

DISSERTATION

THE APPLICATION OF CARBON COMPOSITE ELECTRODES FOR THE ANALYSIS OF
ENVIRONMENTAL AND BIOLOGICAL PATHOGENS

Submitted by:

Catherine J. McMahon

Department of Chemistry

In partial fulfillment of the requirements

For the Degree of Doctor of Philosophy

Colorado State University

Fort Collins, Colorado

Spring 2023

Doctoral Committee:

Advisor: Charles S. Henry

Amy L. Prieto
Delphine Farmer
Brian Geiss

Copyright by Catherine J. McMahon 2023

All Rights Reserved

ABSTRACT

THE APPLICATION OF CARBON COMPOSITE ELECTRODES FOR THE ANALYSIS OF ENVIRONMENTAL AND BIOLOGICAL PATHOGENS

Fast, reliable, and accurate detection of heavy metals is crucial in preventing adverse health effects. Heavy metal contamination comes from various human anthropological endeavors, and can leach into water, food, and consumer products such as cosmetics. Electrochemical detection of heavy metals has become a popular alternative to traditional analysis, using highly sensitive spectroscopic techniques. Carbon composite electrodes have been used for electrochemical sensors due to their chemical inertness, large potential window, and resistance to fouling. However, they can often suffer from poor electrocatalytic behavior, resulting in the need for extensive surface modifications. Moreover, traditional carbon composite electrodes have been limited in their pattern-ability and difficulty in fabrication. Thermoplastic electrodes were developed in 2017 to address these needs and are further discussed and characterized in this dissertation for applications towards heavy metal analysis. Overall, this dissertation seeks to use carbon composite electrodes to improve detection efforts for both environmental pollutants (i.e heavy metals) and biological analytes.

Chapter 2 introduces the use of stencil-printed carbon electrodes (SPCEs) for the analysis of heavy metals in cosmetic samples from Nepal, Ghana, and Uganda. The approach utilizes a previously developed method and adapts it, expanding its utility. The goal of the work is to develop a method that is capable of screening for heavy metal pollutants outside of traditional laboratory settings. An alternative sample extraction approach is detailed as well as the development of a

laboratory standard for heavy metal analysis in cosmetics. In addition to the electrochemical analysis, extensive analysis using inductively coupled plasma optical emission spectroscopy is conducted on the cosmetics samples, to better understand the Pb contamination and matrix complexity of the samples.

Chapter 3 focuses on the use of TPEs for the detection of heavy metals. Six formulations of TPEs, with different graphites and polymer binders, are characterized to better understand how the unique surface properties impact the analysis of heavy metals. The detection of Pb is used as a proof-of-concept model. The results illustrate that both the polymer and graphite can have intensive impact on the application of TPEs. Of the various formulations tested, polystyrene and polymethyl methacrylate show promise in detecting heavy metals within relevant ranges.

Chapter 4 pivots from heavy metal analysis and investigates the use of SPCEs for the detection of SARS-CoV-2 nucleocapsid protein. With the onset of the COVID-19 pandemic in 2020, my research focus pivoted to address the need to develop reliable, accurate, and fast point-of-care diagnostics for SARS-CoV-2 to help manage the spread of the virus. SPCEs are modified based on an ELISA (enzyme-linked immunosorbent assay) for the electrochemical detection of the N-protein. The assay developed sets the framework for a potential POC diagnostic, while meeting the industry need for fewer false negatives and lower limits of detection.

In summary, this dissertation seeks to implement and expand the utility of different kinds of carbon composite electrodes for the detection of heavy metals and biological analytes. The work described in this dissertation sets the framework for improving upon carbon-based electrochemical sensors for environmental and biological sensors. This work provides materials, methods, and fundamental characterization of carbon composite electrodes, and how different surface treatments and modifications can expand their utility in electrochemically sensing applications.

ACKNOWLEDGEMENTS

First, I would like to thank my advisor, Dr. Chuck Henry. Through his mentorship and guidance, I have grown exponentially as a scientist and as a person. His knowledge, the long conversations about research ideas, support, and unwavering patience has helped shaped me into the professional that I am today. He has been an excellent example, showing me that you don't have to be defined to one area of work, and if you work hard, show kindness, and embrace ideas, you can truly make a difference. I would not have made it through the program without his support.

Second, I would like to thank my fellow Henry group members. The community that we have formed within the group is something I will always cherish, and the friendships I will leave with hold so much value to me. The memories that we made, both inside the lab and out are what truly made my PhD memorable. I would especially like to thank Brandaise Martinez, my emotional support research buddy, because without her support, I would not be where I am. While the project that jump-started our friendship is not included in this dissertation, I am grateful for the experience, because it brought me one of my biggest allies and supporters. RIP Mountain Boomer. Her continued optimism, comic relief, and friendship are inspiring.

Third, I would like to thank my thesis committee, for helping guide me throughout my PhD journey. Your advice and ideas have helped shape my graduate school career. Dr. Amy Prieto and Dr. Delphine Farmer have inspired me as fellow women in science. Dr. Brian Geiss, who helped guide and mentor on the work discussed in Chapter 4 and for stepping in at the last minute to fill a vacancy on my committee.

Most importantly, I would like to thank my friends and family for their unwavering support throughout this journey. My friends, both near and far, have made the twist and turns of graduate

school more bearable, and often even beautiful. To my mom, who has been my biggest supporter and ally since day one. I am forever grateful to you, and this success is yours, too. To my brothers, who keep me grounded and remind me to not take life too seriously. I may be the oldest, but all three of you have been my teachers. To Liam, who deserves a special shoutout. His unwavering support in these last stages of my PhD have helped get me over the finish line. And to Toni, whose personal and professional presence in my life throughout my PhD has been unforgettable. Her collaboration on research projects, late night conversations, and endless laughs have been a beacon of light. To all my friends, mentors, and family who have believed in me, even when I didn't believe in myself, I am grateful to you. The community you surround yourself helps define you, and I would not be the person I am today without all of your continued help along the way.

TABLE OF CONTENTS

ABSTRACT.....	i
ACKNOWLEDGEMENTS.....	iv
CHAPTER 1. INTRODUCTION.....	1
1.1 Electrochemical Detection of Heavy Metals.....	1
1.2 Electrochemical Biosensors.....	3
1.3 Carbon Electrodes.....	5
1.4 Thermoplastic Electrodes.....	7
1.5 My Contributions.....	8
REFERENCES.....	11
CHAPTER 2: ANALYSIS OF EYELINER COSMETIC SAMPLES AND THE DEVELOPMENT OF AN ALTERNATIVE ANALYSIS METHOD USING CITRIC ACID AND ANODIC STRIPPING VOLTAMMETRY.....	18
2.2 Introduction.....	18
2.3 Materials and Methods.....	23
2.4 Results and Discussion.....	28
2.5 Conclusion.....	40
REFERENCES.....	42

CHAPTER 3: THERMOPLASTIC ELECTRODES FOR THE ANALYSIS OF LEAD USING ANODIC STRIPPING VOLTAMMETRY.....	46
3.2 Introduction.....	47
3.3 Materials and Methods.....	48
3.4 Results and Discussion.....	52
3.5 Conclusion.....	67
REFERENCES.....	68
CHAPTER 4: ELECTROCHEMICAL IMMUNOASSAY FOR THE DETECTION OF SARS-CoV-2 NUCLEOCAPSID PROTEIN IN NASOPHARYNGEAL SAMPLES.....	73
4.2 Introduction.....	74
4.3 Materials and Methods.....	76
4.4 Results and Discussion.....	81
4.5 Conclusion.....	91
REFERENCES.....	93
CHAPTER 5. CONCLUSION AND FUTURE DIRECTIONS.....	97
REFERENCES.....	104
APPENDIX 1.....	107
APPENDIX 2.....	109
APPENDIX 3.....	112

Chapter 1: INTRODUCTION

1.1 Electrochemical Detection of Heavy Metals

Heavy metals (HM) are naturally occurring elements found in the Earth's crust and are defined as elements with density greater than 5 g/cm^3 .¹ They can be categorized into two primary categories, essential and non-essential. Metals classified as non-essential include lead (Pb), cadmium (Cd), mercury (Hg), and chromium (Cr).² Through various anthropogenic activities, heavy metals can leach into mediums such as food, water, soil, and consumer products, threatening human health.^{3,4} Through exposure to contaminated sources via either dermal adsorption, ingestion or inhalation, HM can bioaccumulate in the human body, leading to a cascade of health effects.⁵ According to the Environmental Protection Agency (EPA), Pb can be permitted in drinking water up to 15 ppb, with the ultimate goal of zero Pb contamination.⁶ To prevent adverse exposure to heavy metals, monitoring of heavy metal concentrations is crucial.

Analysis of heavy metals usually utilizes highly sensitive spectroscopic techniques such as atomic adsorption spectroscopy, inductively coupled plasma-optical emission (ICP-OES) and mass spectrometry (ICP-MS).⁷ Samples often undergo rigorous preparation and digestion protocols, using concentrated acids and high temperatures in order to fully dissociate the metal ions from their sample matrix.⁸ While these methods are effective, they are time consuming, costly, and require experienced personnel. Electrochemical analysis of heavy metals has become a popular alternative as they are user-friendly, low cost, enable fast analyses, and can be miniaturized for utilization outside of typical laboratory environments.⁹ Typically, a three-electrode system is utilized for heavy metal detection that consists of a modified working electrode (WE), and reference electrode (RE), and counter electrode (CE). The electrolyte is the aqueous solution containing the heavy metal ion and the conductor is the electrode itself. By applying different

techniques, various half reactions can take place which allow for quantitative measurement of the heavy metal ions.¹⁰

Heavy metal ions can be electro-analytically measured with a variety of techniques, including potentiometry,^{11,12} chronoamperometry,¹³ cyclic voltammetry,¹⁴ and stripping voltammetry.^{15,16} Despite potentiometric and chronoamperometric techniques being viable techniques, they suffer from lower sensitivity/high LOD or require complex surface modification in comparison to voltammetry. For voltametric techniques, the potential is controlled, and the current response is used to measure the heavy metal ions in solution. In doing so, the technique is able to suppress the background current and increase sensitivity/LOD.¹⁰ Of the many electrochemical techniques that can be used, square-wave anodic stripping voltammetry (ASV) is the most common, lending to its high sensitivity and minimal background current. ASV can measure labile metal concentrations at the sub-ppb level using electrodeposition, which pre-concentrates the metal of interest on the electrode surface. The sub-sequent oxidative stripping peaks, specific to individual metal ions, can then be used to quantify the metal ion of interest.^{17,18}

Several different electrode materials have been developed for the electro-analysis of heavy metals. Mercury electrodes were one of the first materials used for heavy metal analysis, because of their high sensitivity, wide potential ranges, and ability to form amalgams with various metal ions.¹⁹ The hanging mercury drop electrodes were among the first to be used for trace metal analysis, but due to the instability of the electrode, research pivoted to thin-film mercury electrodes.²⁰ The conductivity of Hg and the poor hydrogen evolution reaction (HER) kinetics allow Hg thin film electrodes to be utilized over wide potential ranges. Further, the Hg can form stable amalgams with deposited metals, increasing stability and deposition efficiency.^{21,22} Many Hg thin-film electrodes use a carbon base, and due to the toxicity of Hg, several efforts have sought

to replace Hg with a bismuth (Bi) film, which behaves in a similar manner to Hg but is non-toxic.^{23–}
²⁵ Much like Hg, Bi can form a thin layer on the electrode surface, promoting the nucleation of metal ions during deposition, which can then be stripped off (either anodically or cathodically), producing resolved and quantifiable peaks (**Figure 1.1**).²⁶ With the movement away from Hg-based electrodes, carbon-based electrodes have become more popular for heavy metal analysis. Chapters two and three seek to improve upon and develop novel electrochemical sensors for Pb analysis using carbon-based electrode systems.

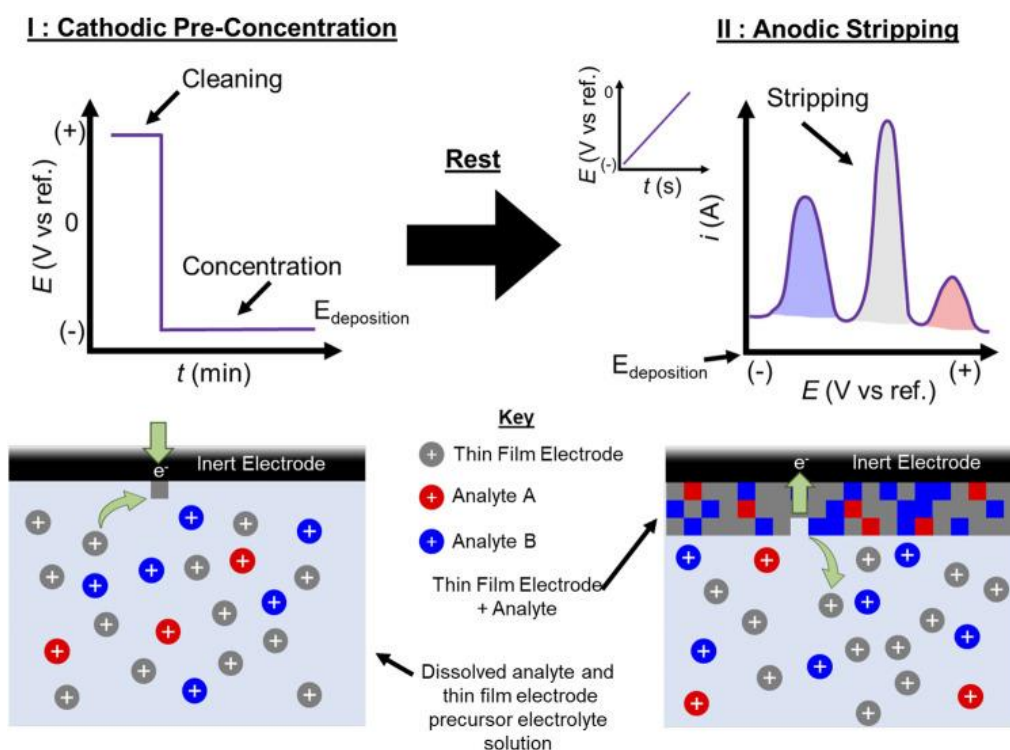


Figure 1.1: Schematic of the ASV process for heavy metal ions, utilizing a thin-film on an in-situ electrode system. Figure from Wygant, *et al.*²¹

1.2 Electrochemical Biosensors

Environmental pollutants have also been detected using various types of biosensors. A biosensor consists of two main elements, the bioreceptor and a transducer.²⁷ The bioreceptor acts as a recognition element for the analyte of interest and the transducer converts the interaction into a measurable signal. Examples of common bioreceptors include nucleic acids, cells, antibodies,

and enzymes.²⁸ Of the several different types of biosensors, electrochemical biosensors have been studied extensively because they are capable of low limits of detection, specificity, and are user-friendly.²⁹ The immobilization of a glucose oxidase enzyme on an oxygen electrode for the detection of glucose was one of the first reported electrochemical biosensors back in 1962.³⁰ Immunosensors, aptasensors, and enzymatic biosensors have all been developed for detecting a handful of environmental pollutants, including heavy metals.³¹ Enzymatic, whole cell, microbial, nucleic acid, and biofilm electrochemical biosensors have all been developed for the trace-level detection of heavy metals in water sources.³² These sensors are capable of detecting heavy metals within EPA and WHO regulations, making them promising candidates for environmental screening and prevention operations.

Beyond applications in environmental sensing, electrochemical biosensors are often utilized in medical, biological, and biotechnological applications.²⁸ Biosensor use is growing exponentially in the medical field for diagnosis and monitoring of diseases, with a recent push in infectious diseases.³³ Nucleic-acid amplification tests like PCR or immunoassays such as an ELISA are the most common methods for detecting infectious disease, but are also labor intensive and time consuming.³⁴⁻³⁷ ELISAs (enzyme link immunosorbent assay) are often used to detect an antigen or antibody of a disease using a conjugated enzyme and substrate.³⁸ Electrochemically, enzymes are chosen that can react with a substrate to create a redox product, which can then be measured and quantified.^{39,40}

In recent years, electrochemical biosensors have been applied to developing point-of-care (POC) diagnostics for a variety of diseases. POC tests are multifaceted, as they need to be fast, sensitive, and selective while also being small and user-friendly. Electrochemical biosensors fulfill several of those requirements, making them promising candidates for POC diagnostic

development.^{41,42} At the onset of the COVID-19 pandemic in 2020, there was a huge need for the development of point-of-care devices for the monitoring and diagnosis of the virus. The WHO listed POC diagnostic development for SARS-CoV-2 a top research priority. Several electrochemical POC diagnostics were developed that utilized microfluidics, screen-printed devices and electrochemical paper-based analytical devices.⁴³ Several variations of carbon-based electrochemical systems were developed for the detection of viruses, with most implementing an ELISA-based surface modification approach using voltametric or impedimetric-mode based sensors.⁴⁴ However, many of the POC sensors failed to meet the WHO minimum criteria for positive and negative sample detection and suffered when analyzing real patient samples. Chapter 4 of this dissertation explores the preliminary development of a POC electrochemical biosensor for the detection of SARS-CoV-2 using a carbon-based ELISA system, seeking to address the drawbacks of other POC diagnostics for COVID-19.

1.3 Carbon Electrodes

Carbon electrodes have come to the forefront in several industries because of the diverse physical and chemical properties they can emulate. Carbon based materials have wide potential windows, chemical stability, and complex surface chemistry while maintaining tunable electron transfer and charge-storage properties.^{45,46} Further, carbon electrodes are recognized for their inert electrochemistry⁴⁷, which is imperative for deployment in sensing applications. Several types of carbon electrodes have been developed, which have utilized the various allotropes of carbon, including graphite, diamond, and fullerene – all of which present different electrochemical features.⁴⁷ Graphitic carbon has become the most carbon allotrope for electrochemical sensors, being the most crystalline form of carbon and as such, exhibits properties similar to precious metal counterparts (electrical and thermal conductivity) and chemical inertness and lubricity.⁴⁸ Graphite

can be broken down into natural and synthetic classifications, which can be further categorized into a handful of varieties.⁴⁸ The type of graphite can then have a cascade effect on the electrochemical performance.

Carbon composite electrodes are one of the most common carbon electrodes used in electrochemical applications, and are defined by a conductive phase (i.e., carbon) being mixed with an insulating matrix.⁴⁹ The type of insulating matrix and carbon source can have intrinsic properties on the electrochemical behavior. There are several types of carbon composite electrodes, including carbon paste, stencil or screen printed carbon electrodes (SPCE), and epoxy-based electrodes.⁵⁰⁻⁵³ Stencil-printed carbon electrodes (SPCE) have been developed extensively, because of their low cost, ease of fabrication, and ability to be incorporated into point-of-need devices/applications.⁵⁴⁻⁵⁷ While SPCE can have limitations in regards to their electrochemical performance in comparison to other carbon composite electrodes, several surface modifications can be implemented to enhance conductivity and their electron transfer kinetics. Further, the reduction in size of the electrodes allows for smaller reagent volumes while the disposability feature negates issues of cleaning and memory effects.⁵³ SPCEs are attractive for heavy metal analysis as they eliminate carryover contamination and/or biofouling from multiple uses, which is a critical component when looking at trace-level analysis. Further, SPCEs can be versatile in both design and modification with the incorporation of different insulating inks (carbon or precious metal) and surface additives such as carbon nanomaterials or other covalent conjugations.⁵⁸

Carbon composite electrodes can be greatly influenced by the type of insulator and graphite used for fabrication. Different graphites (sources and sizes) can lead to significant differences in surface functional groups, therefore effecting the surface chemistry of the electrode.⁵⁹ Surface oxides are some of the most prominent surface functional groups, which can be separated into acidic

(carboxylic, phenolic), neutral (benzoquinonyl) and alkaline groups (carbonyls).⁶⁰ Surface oxides can be influenced by the morphology and surface preparation (sanding/polishing) of the electrode surface, which can then effect electron transfer, adsorption and electrocatalysis.^{47,61} Different techniques can be applied to activate the carbon surface, which can tune the surface chemistry towards detection of different analytes. Examples include plasma treatment to create more hydrophilic surfaces which attract aqueous analytes or electrochemical activation to create a net charge on the surface, promoting interaction with analytes of opposite charge.⁶² Further, the physical structure of the carbon electrode can impact the applicability. In relation to metal deposition, surfaces that contain mesopores or macropores that are more acidic are the most effective in depositing Pb.^{60,63} The binder, or insulator, can limit carbon composite electrode utility in respect to the electrocatalytic activity or the moldability. Some binders can interfere with the electrochemical performance by hindering electron transfer with the graphite and/or fabrication is limited, due to poor pattern-ability. Both aspects are important consideration when designing electrodes for sensing applications.

1.4 Thermoplastic Electrodes

Thermoplastic electrodes (TPEs) were introduced in 2017 by the Henry group, and described as easily fabricated carbon composite electrodes that maintain excellent electrochemical properties.⁶⁴ Broadly, TPEs are fabricated by combining a thermoplastic polymer, acting as the insulator, with a graphitic carbon source. Thermoplastic polymers are attractive insulators because they can be heated and molded into various patterns without losing their structural integrity.⁶⁵ With the mechanistic properties of the thermoplastic unaffected, TPEs are only limited by the carbon particle size and respective mass loading of the carbon source.^{64,66} Previous characterization has shown TPEs can have 10:1 or higher carbon:polymer ratios, lending them to be highly conductive.

TPEs have reported conductivities up to ~1000 S/m, which is significantly higher than other previously reported SPCEs and in good agreement with other carbon composite electrodes.^{66–68}

Several different types of thermoplastics have been implemented in TPEs, including polymethyl methacrylate (PMMA)^{64,69}, polystyrene (PS)^{67,70}, and polycaprolactone (PCL).^{66,71} Previous characterization of TPEs with all three polymers have demonstrated that their electrochemical performance is comparable to other carbon composite electrodes, as well as glassy carbon and precious metal electrodes. The electrode characteristics can be tuned by adjusting the carbon source, thermoplastic, or the ratio of the two. Such adjustments can alter the electrochemical and physical characteristics, broadening their overall application. TPEs have been used to create biological sensors^{70–73}, but little has been done to apply them to environmental pathogens such as heavy metals. The application of all three binder types with different carbon sources for application in heavy metal analysis will be further discussed in this dissertation.

1.5 My Contributions

This dissertation aims to apply carbon composite electrodes toward the sensing of both environmental and biological pathogens. In Chapter 2, SPCEs are used to characterize and analyze Pb contamination in cosmetic samples from resource-limited areas. The electrochemical method is adapted to be suitable analysis of samples with high metal contamination, rather than trace-level analysis, which is rarely done. The new method sets the framework for alternative analysis of heavy metals in cosmetics without the use of sophisticated instrumentation and hazardous chemicals.

Chapter 3 explores the utility of TPEs for environmental monitoring. The analysis of Pb is explored as a proof-of-concept model, to understand if TPEs can be applied to trace-metal analysis.

Unlike Chapter 2, where the focus is on high levels of contamination, Chapter 3 focuses on trace-level analysis, with the goal of developing reusable sensors, unlike the SPCE counterparts which have been previously developed. Due to the surprising results, further physical and chemical characterization was conducted on several formulations of TPEs, to gain insight on which properties impact TPE performance.

Chapter 4 completely switches focus, with the development of an electrochemical sensor for the detection of COVID-19 nucleocapsid protein. Due to the on-set of the COVID-19 pandemic, my research focus pivoted to address the need for low-cost, point-of-care sensors to combat the continued spread of the virus. The work with SPCEs from Chapter 2 was broadened to be applicable to biosensors. The work focuses on the adapting a sandwich ELISA approach to an electrochemical sensor, to create a highly sensitive and accurate diagnostic. The SPCEs are modified with antibodies for the SARS-CoV-2, using covalent conjugation to the electrode surface. Inactivated virus samples are then tested and quantified using electrochemically active enzyme substrates, bound specifically to the antigen target. A proof-of-concept clinical study is conducted, showing preliminary data that the sensor could be used to assess infectivity rates of individuals. While the sensor does not meet the requirements of a point-of-care diagnostic, it sets the framework for future POC devices.

Overall, this dissertation seeks to employ low-cost and tunable electrochemical sensors for the analysis of environmental and biological analytes. The majority of the work is focused on utilizing carbon composite electrodes as electrochemical sensors for heavy metals, with a specific focus on Pb contamination. The focus is then slightly shifted toward developing a carbon-based electrochemical system for the detection of COVID-19. More broadly, all three elements of the

dissertation provide preliminary groundwork for making electrochemical sensors more deployable outside of traditional laboratory settings, without sacrificing performance or accuracy.

References

- (1) Järup, L. Hazards of Heavy Metal Contamination. *Br. Med. Bull.* **2003**, *68* (1), 167–182. <https://doi.org/10.1093/bmb/ldg032>.
- (2) Raychaudhuri, S. S.; Pramanick, P.; Talukder, P.; Basak, A. Chapter 6 - Polyamines, Metallothioneins, and Phytochelatins—Natural Defense of Plants to Mitigate Heavy Metals. In *Studies in Natural Products Chemistry*; Atta-ur-Rahman, Ed.; Bioactive Natural Products; Elsevier, 2021; Vol. 69, pp 227–261. <https://doi.org/10.1016/B978-0-12-819487-4.00006-9>.
- (3) Tchounwou, P. B.; Yedjou, C. G.; Patlolla, A. K.; Sutton, D. J. Heavy Metals Toxicity and the Environment. *EXS* **2012**, *101*, 133–164. https://doi.org/10.1007/978-3-7643-8340-4_6.
- (4) Yadav, M.; Gupta, R.; Sharma, R. K. Chapter 14 - Green and Sustainable Pathways for Wastewater Purification. In *Advances in Water Purification Techniques*; Ahuja, S., Ed.; Elsevier, 2019; pp 355–383. <https://doi.org/10.1016/B978-0-12-814790-0.00014-4>.
- (5) Ahmad, W.; Alharthy, R. D.; Zubair, M.; Ahmed, M.; Hameed, A.; Rafique, S. Toxic and Heavy Metals Contamination Assessment in Soil and Water to Evaluate Human Health Risk. *Sci. Rep.* **2021**, *11* (1), 17006. <https://doi.org/10.1038/s41598-021-94616-4>.
- (6) US EPA, O. *Basic Information about Lead in Drinking Water*. <https://www.epa.gov/ground-water-and-drinking-water/basic-information-about-lead-drinking-water> (accessed 2023-01-09).
- (7) Sastre, J.; Sahuquillo, A.; Vidal, M.; Rauret, G. Determination of Cd, Cu, Pb and Zn in Environmental Samples: Microwave-Assisted Total Digestion versus Aqua Regia and Nitric Acid Extraction. *Anal. Chim. Acta* **2002**, *462* (1), 59–72. [https://doi.org/10.1016/S0003-2670\(02\)00307-0](https://doi.org/10.1016/S0003-2670(02)00307-0).
- (8) Shahbazi, K.; Beheshti, M. Comparison of Three Methods for Measuring Heavy Metals in Calcareous Soils of Iran. *SN Appl. Sci.* **2019**, *1* (12), 1541. <https://doi.org/10.1007/s42452-019-1578-x>.
- (9) Pujol, L.; Evrard, D.; Groenen-Serrano, K.; Freyssinier, M.; Ruffien-Cizsak, A.; Gros, P. Electrochemical Sensors and Devices for Heavy Metals Assay in Water: The French Groups' Contribution. *Front. Chem.* **2014**, *2*.
- (10) Bansod, B.; Kumar, T.; Thakur, R.; Rana, S.; Singh, I. A Review on Various Electrochemical Techniques for Heavy Metal Ions Detection with Different Sensing Platforms. *Biosens. Bioelectron.* **2017**, *94*, 443–455. <https://doi.org/10.1016/j.bios.2017.03.031>.
- (11) Zanganeh, A. R.; Amini, M. K. Polypyrrole-Modified Electrodes with Induced Recognition Sites for Potentiometric and Voltammetric Detection of Copper(II) Ion. *Sens. Actuators B Chem.* **2008**, *135* (1), 358–365. <https://doi.org/10.1016/j.snb.2008.09.005>.
- (12) Prakash, R.; Srivastava, R.; Pandey, P. Copper(II) Ion Sensor Based on Electropolymerized Undoped Conducting Polymers. *J. Solid State Electrochem.* **2002**, *6* (3), 203–208. <https://doi.org/10.1007/s100080100213>.

- (13) Yasri, N. G.; Halabi, Ahmad. J.; Istamboulie, G.; Noguier, T. Chronoamperometric Determination of Lead Ions Using PEDOT:PSS Modified Carbon Electrodes. *Talanta* **2011**, *85* (5), 2528–2533. <https://doi.org/10.1016/j.talanta.2011.08.013>.
- (14) Quintana, H.; Ramírez, J. L.; Rubio, E. F.; Marquez, E.; González, G.; González, G.; Uruchurtu, J. Electrochemical Sensor Based on Polypyrrole for the Detection of Heavy Metals in Aqueous Solutions. *ECS Trans.* **2013**, *47* (1), 265. <https://doi.org/10.1149/04701.0265ecst>.
- (15) Manisankar, P.; Vedhi, C.; Selvanathan, G.; Arumugam, P. Differential Pulse Stripping Voltammetric Determination of Heavy Metals Simultaneously Using New Polymer Modified Glassy Carbon Electrodes. *Microchim. Acta* **2008**, *163* (3), 289–295. <https://doi.org/10.1007/s00604-008-0013-6>.
- (16) Yoo, K.-S.; Woo, S.-B.; Jyoung, J.-Y. Trace Mercury Determination by Differential Pulse Anodic Stripping Voltammetry Using Polythiophene-Quinoline/Glassy Carbon Modified Electrode. *Bull. Korean Chem. Soc.* **2003**, *24* (1), 27–31. <https://doi.org/10.5012/bkcs.2003.24.1.027>.
- (17) Borrill, A. J.; Reily, N. E.; Macpherson, J. V. Addressing the Practicalities of Anodic Stripping Voltammetry for Heavy Metal Detection: A Tutorial Review. *Analyst* **2019**, *144* (23), 6834–6849. <https://doi.org/10.1039/C9AN01437C>.
- (18) Barón-Jaimez, J.; Joya, M. R.; Barba-Ortega, J. Anodic Stripping Voltammetry – ASV for Determination of Heavy Metals. *J. Phys. Conf. Ser.* **2013**, *466* (1), 012023. <https://doi.org/10.1088/1742-6596/466/1/012023>.
- (19) Ariño, C.; Serrano, N.; Díaz-Cruz, J. M.; Esteban, M. Voltammetric Determination of Metal Ions beyond Mercury Electrodes. A Review. *Anal. Chim. Acta* **2017**, *990*, 11–53. <https://doi.org/10.1016/j.aca.2017.07.069>.
- (20) Kudr, J.; Nguyen, H. V.; Gumulec, J.; Nejdil, L.; Blazkova, I.; Ruttkay-Nedecky, B.; Hynek, D.; Kynicky, J.; Adam, V.; Kizek, R. Simultaneous Automatic Electrochemical Detection of Zinc, Cadmium, Copper and Lead Ions in Environmental Samples Using a Thin-Film Mercury Electrode and an Artificial Neural Network. *Sensors* **2015**, *15* (1), 592–610. <https://doi.org/10.3390/s150100592>.
- (21) Wygant, B. R.; Lambert, T. N. Thin Film Electrodes for Anodic Stripping Voltammetry: A Mini-Review. *Front. Chem.* **2022**, *9*, 809535. <https://doi.org/10.3389/fchem.2021.809535>.
- (22) Wu, H. Ping. Nature and Stability of Mercury Thin Films on Glassy Carbon Electrodes under Fast-Scan Anodic Stripping Voltammetry. *Anal. Chem.* **1994**, *66* (19), 3151–3157. <https://doi.org/10.1021/ac00091a025>.
- (23) Baldo, M. A.; Daniele, S.; Bragato, C. Bismuth Film Microelectrodes for Heavy Metals Monitoring by Anodic Stripping Voltammetry. *J. Phys. IV Proc.* **2003**, *107*, 103–106. <https://doi.org/10.1051/jp4:20030254>.
- (24) Economou, A. Bismuth-Film Electrodes: Recent Developments and Potentialities for Electroanalysis. *TrAC Trends Anal. Chem.* **2005**, *24* (4), 334–340. <https://doi.org/10.1016/j.trac.2004.11.006>.

- (25) Wang, J.; Lu, J.; Hocevar, S. B.; Farias, P. A. M.; Ogorevc, B. Bismuth-Coated Carbon Electrodes for Anodic Stripping Voltammetry. *Anal. Chem.* **2000**, *72* (14), 3218–3222. <https://doi.org/10.1021/ac000108x>.
- (26) Lee, S.; Bong, S.; Ha, J.; Kwak, M.; Park, S.-K.; Piao, Y. Electrochemical Deposition of Bismuth on Activated Graphene-Nafion Composite for Anodic Stripping Voltammetric Determination of Trace Heavy Metals. *Sens. Actuators B Chem.* **2015**, *215*, 62–69. <https://doi.org/10.1016/j.snb.2015.03.032>.
- (27) Lee, Y. H.; Mutharasan, R. CHAPTER 6 - Biosensors. In *Sensor Technology Handbook*; Wilson, J. S., Ed.; Newnes: Burlington, 2005; pp 161–180. <https://doi.org/10.1016/B978-075067729-5/50046-X>.
- (28) Grieshaber, D.; MacKenzie, R.; Vörös, J.; Reimhult, E. Electrochemical Biosensors - Sensor Principles and Architectures. *Sensors* **2008**, *8* (3), 1400–1458.
- (29) Sawant, S. N. 13 - Development of Biosensors From Biopolymer Composites. In *Biopolymer Composites in Electronics*; Sadasivuni, K. K., Ponnamma, D., Kim, J., Cabibihan, J.-J., AlMaadeed, M. A., Eds.; Elsevier, 2017; pp 353–383. <https://doi.org/10.1016/B978-0-12-809261-3.00013-9>.
- (30) *ELECTRODE SYSTEMS FOR CONTINUOUS MONITORING IN CARDIOVASCULAR SURGERY - Clark - 1962 - Annals of the New York Academy of Sciences - Wiley Online Library.* <https://nyaspubs.onlinelibrary.wiley.com/doi/abs/10.1111/j.1749-6632.1962.tb13623.x> (accessed 2023-01-10).
- (31) Justino, C. I. L.; Duarte, A. C.; Rocha-Santos, T. A. P. Recent Progress in Biosensors for Environmental Monitoring: A Review. *Sensors* **2017**, *17* (12), 2918. <https://doi.org/10.3390/s17122918>.
- (32) Hara, T. O.; Singh, B. Electrochemical Biosensors for Detection of Pesticides and Heavy Metal Toxicants in Water: Recent Trends and Progress. *ACS EST Water* **2021**, *1* (3), 462–478. <https://doi.org/10.1021/acsestwater.0c00125>.
- (33) Mehrotra, P. Biosensors and Their Applications – A Review. *J. Oral Biol. Craniofacial Res.* **2016**, *6* (2), 153–159. <https://doi.org/10.1016/j.jobcr.2015.12.002>.
- (34) Kwok, S.; Sninsky, J. J. Application of PCR to the Detection of Human Infectious Diseases. In *PCR Technology: Principles and Applications for DNA Amplification*; Erlich, H. A., Ed.; Palgrave Macmillan UK: London, 1989; pp 235–244. https://doi.org/10.1007/978-1-349-20235-5_19.
- (35) Yang, S.; Rothman, R. E. PCR-Based Diagnostics for Infectious Diseases: Uses, Limitations, and Future Applications in Acute-Care Settings. *Lancet Infect. Dis.* **2004**, *4* (6), 337–348. [https://doi.org/10.1016/S1473-3099\(04\)01044-8](https://doi.org/10.1016/S1473-3099(04)01044-8).
- (36) Fredricks, D. N.; Relman, D. A. Application of Polymerase Chain Reaction to the Diagnosis of Infectious Diseases. *Clin. Infect. Dis.* **1999**, *29* (3), 475–486.
- (37) Yolken, R. H. Enzyme Immunoassays for the Detection of Microbial Antigens and Prospects for Improved Assays. *Yale J. Biol. Med.* **1986**, *59* (1), 25–31.

- (38) Sykes, J. E.; Rankin, S. C. Chapter 2 - Immunoassays. In *Canine and Feline Infectious Diseases*; Sykes, J. E., Ed.; W.B. Saunders: Saint Louis, 2014; pp 10–16. <https://doi.org/10.1016/B978-1-4377-0795-3.00002-8>.
- (39) Bhimji, A.; Zaragoza, A. A.; Live, L. S.; Kelley, S. O. Electrochemical Enzyme-Linked Immunosorbent Assay Featuring Proximal Reagent Generation: Detection of Human Immunodeficiency Virus Antibodies in Clinical Samples. *Anal. Chem.* **2013**, *85* (14), 6813–6819. <https://doi.org/10.1021/ac4009429>.
- (40) Liu, Q.-L.; Yan, X.-H.; Yin, X.-M.; Situ, B.; Zhou, H.-K.; Lin, L.; Li, B.; Gan, N.; Zheng, L. Electrochemical Enzyme-Linked Immunosorbent Assay (ELISA) for α -Fetoprotein Based on Glucose Detection with Multienzyme-Nanoparticle Amplification. *Molecules* **2013**, *18* (10), 12675–12686. <https://doi.org/10.3390/molecules181012675>.
- (41) Ning, Q.; Feng, S.; Cheng, Y.; Li, T.; Cui, D.; Wang, K. Point-of-Care Biochemical Assays Using Electrochemical Technologies: Approaches, Applications, and Opportunities. *Mikrochim. Acta* **2022**, *189* (8), 310. <https://doi.org/10.1007/s00604-022-05425-z>.
- (42) Wan, Y.; Su, Y.; Zhu, X.; Liu, G.; Fan, C. Development of Electrochemical Immunosensors towards Point of Care Diagnostics. *Biosens. Bioelectron.* **2013**, *47*, 1–11. <https://doi.org/10.1016/j.bios.2013.02.045>.
- (43) Biswas, G. C.; Choudhury, S.; Rabbani, M. M.; Das, J. A Review on Potential Electrochemical Point-of-Care Tests Targeting Pandemic Infectious Disease Detection: COVID-19 as a Reference. *Chemosensors* **2022**, *10* (7), 269. <https://doi.org/10.3390/chemosensors10070269>.
- (44) Antiochia, R. Electrochemical Biosensors for SARS-CoV-2 Detection: Voltametric or Impedimetric Transduction? *Bioelectrochemistry Amst. Neth.* **2022**, *147*, 108190. <https://doi.org/10.1016/j.bioelechem.2022.108190>.
- (45) Baptista, F. R.; Belhout, S. A.; Giordani, S.; Quinn, S. J. Recent Developments in Carbon Nanomaterial Sensors. *Chem. Soc. Rev.* **2015**, *44* (13), 4433–4453. <https://doi.org/10.1039/C4CS00379A>.
- (46) Zhang, W.; Zhu, S.; Luque, R.; Han, S.; Hu, L.; Xu, G. Recent Development of Carbon Electrode Materials and Their Bioanalytical and Environmental Applications. *Chem. Soc. Rev.* **2016**, *45* (3), 715–752. <https://doi.org/10.1039/C5CS00297D>.
- (47) McCreery, R. L. Advanced Carbon Electrode Materials for Molecular Electrochemistry. *Chem. Rev.* **2008**, *108* (7), 2646–2687. <https://doi.org/10.1021/cr068076m>.
- (48) Wissler, M. Graphite and Carbon Powders for Electrochemical Applications. *J. Power Sources* **2006**, *156* (2), 142–150. <https://doi.org/10.1016/j.jpowsour.2006.02.064>.
- (49) Corb, I.; Manea, F.; Radovan, C.; Pop, A.; Burtica, G.; Malchev, P.; Picken, S.; Schoonman, J. Carbon-Based Composite Electrodes: Preparation, Characterization and Application in Electroanalysis. *Sensors* **2007**, *7* (11), 2626–2635.
- (50) Ferreira da Silva, P.; Ferreira Gomes, B.; Silva Lobo, C. M.; Carmo, M.; Roth, C.; Colnago, L. A. Composite Graphite–Epoxy Electrodes for In Situ Electrochemistry Coupling

with High Resolution NMR. *ACS Omega* **2022**, 7 (6), 4991–5000.
<https://doi.org/10.1021/acsomega.1c05823>.

(51) Manea, F.; Radovan, C.; Pop, A.; Corb, I.; Burtica, G.; Malchev, P.; Picken, S.; Schoonman, J. Carbon Composite Electrodes Applied for Electrochemical Sensors. In *Sensors for Environment, Health and Security*; Baraton, M.-I., Ed.; NATO Science for Peace and Security Series C: Environmental Security; Springer Netherlands: Dordrecht, 2009; pp 179–189.
https://doi.org/10.1007/978-1-4020-9009-7_11.

(52) A. Wring, S.; P. Hart, J. Chemically Modified, Screen-Printed Carbon Electrodes. *Analyst* **1992**, 117 (8), 1281–1286. <https://doi.org/10.1039/AN9921701281>.

(53) Taleat, Z.; Khoshroo, A.; Mazloun-Ardakani, M. Screen-Printed Electrodes for Biosensing: A Review (2008–2013). *Microchim. Acta* **2014**, 181 (9), 865–891.
<https://doi.org/10.1007/s00604-014-1181-1>.

(54) Martín-Yerga, D.; Álvarez-Martos, I.; Blanco-López, M. C.; Henry, C. S.; Fernández-Abedul, M. T. Point-of-Need Simultaneous Electrochemical Detection of Lead and Cadmium Using Low-Cost Stencil-Printed Transparency Electrodes. *Anal. Chim. Acta* **2017**, 981, 24–33.
<https://doi.org/10.1016/j.aca.2017.05.027>.

(55) Álvarez-Martos, I.; Henry, C. S.; Fernández Abedul, M. T. Chapter 4 - Anodic Stripping Voltammetric Determination of Lead and Cadmium with Stencil-Printed Transparency Electrodes. In *Laboratory Methods in Dynamic Electroanalysis*; Fernandez Abedul, M. T., Ed.; Elsevier, 2020; pp 35–45. <https://doi.org/10.1016/B978-0-12-815932-3.00004-8>.

(56) Berg, K. E.; Adkins, J. A.; Boyle, S. E.; Henry, C. S. Manganese Detection Using Stencil-Printed Carbon Ink Electrodes on Transparency Film. *Electroanalysis* **2016**, 28 (4), 679–684. <https://doi.org/10.1002/elan.201500474>.

(57) Ruecha, N.; Rodthongkum, N.; Cate, D. M.; Volckens, J.; Chailapakul, O.; Henry, C. S. Sensitive Electrochemical Sensor Using a Graphene–Polyaniline Nanocomposite for Simultaneous Detection of Zn(II), Cd(II), and Pb(II). *Anal. Chim. Acta* **2015**, 874, 40–48.
<https://doi.org/10.1016/j.aca.2015.02.064>.

(58) Barton, J.; García, M. B. G.; Santos, D. H.; Fanjul-Bolado, P.; Ribotti, A.; McCaul, M.; Diamond, D.; Magni, P. Screen-Printed Electrodes for Environmental Monitoring of Heavy Metal Ions: A Review. *Microchim. Acta* **2016**, 183 (2), 503–517. <https://doi.org/10.1007/s00604-015-1651-0>.

(59) Oliveira, L. S.; Alba, J. F. G.; Silva, V. L.; Ribeiro, R. T.; Falcão, E. H. L.; Navarro, M. The Effect of Surface Functional Groups on the Performance of Graphite Powders Used as Electrodes. *J. Electroanal. Chem.* **2018**, 818, 106–113.
<https://doi.org/10.1016/j.jelechem.2018.04.022>.

(60) Wang, L.; Zhang, H.; Cao, G.; Zhang, W.; Zhao, H.; Yang, Y. Effect of Activated Carbon Surface Functional Groups on Nano-Lead Electrodeposition and Hydrogen Evolution and Its Applications in Lead-Carbon Batteries. *Electrochimica Acta* **2015**, 186, 654–663.
<https://doi.org/10.1016/j.electacta.2015.11.007>.

- (61) Pacchioni, G.; Freund, H. Electron Transfer at Oxide Surfaces. The MgO Paradigm: From Defects to Ultrathin Films. *Chem. Rev.* **2013**, *113* (6), 4035–4072. <https://doi.org/10.1021/cr3002017>.
- (62) Bowling, R.; Packard, R. T.; McCreery, R. L. Mechanism of Electrochemical Activation of Carbon Electrodes: Role of Graphite Lattice Defects. *Langmuir* **1989**, *5* (3), 683–688. <https://doi.org/10.1021/la00087a022>.
- (63) Yin, J.; Lin, H.; Shi, J.; Lin, Z.; Bao, J.; Wang, Y.; Lin, X.; Qin, Y.; Qiu, X.; Zhang, W. Lead-Carbon Batteries toward Future Energy Storage: From Mechanism and Materials to Applications. *Electrochem. Energy Rev.* **2022**, *5* (3), 2. <https://doi.org/10.1007/s41918-022-00134-w>.
- (64) Klunder, K. J.; Nilsson, Z.; Sambur, J. B.; Henry, C. S. *Patternable Solvent-Processed Thermoplastic Graphite Electrodes*. ACS Publications. <https://doi.org/10.1021/jacs.7b06173>.
- (65) Bîrcă, A.; Gherasim, O.; Grumezescu, V.; Grumezescu, A. M. Chapter 1 - Introduction in Thermoplastic and Thermosetting Polymers. In *Materials for Biomedical Engineering*; Grumezescu, V., Grumezescu, A. M., Eds.; Elsevier, 2019; pp 1–28. <https://doi.org/10.1016/B978-0-12-816874-5.00001-3>.
- (66) Klunder, K. J.; Clark, K. M.; McCord, C.; Berg, K. E.; Minter, S. D.; Henry, C. S. Polycaprolactone-Enabled Sealing and Carbon Composite Electrode Integration into Electrochemical Microfluidics. *Lab. Chip* **2019**, *19* (15), 2589–2597. <https://doi.org/10.1039/C9LC00417C>.
- (67) McCord, C. P.; Summers, B.; Henry, C. S. Redox Behavior and Surface Morphology of Polystyrene Thermoplastic Electrodes. *Electrochimica Acta* **2021**, *393*, 139069. <https://doi.org/10.1016/j.electacta.2021.139069>.
- (68) Randviir, E. P.; Brownson, D. A. C.; Metters, J. P.; Kadara, R. O.; Banks, C. E. The Fabrication, Characterisation and Electrochemical Investigation of Screen-Printed Graphene Electrodes. *Phys. Chem. Chem. Phys. PCCP* **2014**, *16* (10), 4598–4611. <https://doi.org/10.1039/c3cp55435j>.
- (69) Noviana, E.; Klunder, K. J.; Channon, R. B.; Henry, C. S. Thermoplastic Electrode Arrays in Electrochemical Paper-Based Analytical Devices. *Anal. Chem.* **2019**, *91* (3), 2431–2438. <https://doi.org/10.1021/acs.analchem.8b05218>.
- (70) Ozer, T.; McCord, C.; Geiss, B. J.; Dandy, D.; Henry, C. S. Thermoplastic Electrodes for Detection of Escherichia Coli. *J. Electrochem. Soc.* **2021**, *168* (4), 047509. <https://doi.org/10.1149/1945-7111/abf77e>.
- (71) Clark, K. M.; Henry, C. S. Thermoplastic Electrode (TPE)-Based Enzymatic Glucose Sensor Using Polycaprolactone-Graphite Composites. *Electroanalysis* **2022**, *34* (12), 1869–1876. <https://doi.org/10.1002/elan.202100446>.
- (72) Ozer, T.; Henry, C. S. All-Solid-State Potassium-Selective Sensor Based on Carbon Black Modified Thermoplastic Electrode. *Electrochimica Acta* **2022**, *404*, 139762. <https://doi.org/10.1016/j.electacta.2021.139762>.

(73) Ozer, T.; Henry, C. S. Microfluidic-Based Ion-Selective Thermoplastic Electrode Array for Point-of-Care Detection of Potassium and Sodium Ions. *Microchim. Acta* **2022**, *189* (4), 152. <https://doi.org/10.1007/s00604-022-05264-y>.

CHAPTER 2: Analysis of eyeliner cosmetic samples and the development of an alternative analysis method using citric acid and anodic stripping voltammetry.

2.1 Chapter Overview: Heavy metal contamination in consumer products is not a new problem, but little attention has been given to potential contamination in cosmetic products, especially from resource limited settings such as Nepal, Ghana, and Uganda. This work presents the analysis of several eyeliners from each country, using both traditional digestion and analysis methods as well as the preliminary development of an alternative, safer method using citric acid and anodic stripping voltammetry. Preliminary results indicate that the alternative method is suitable for simple matrixes, but further development is needed before use in real cosmetic samples. ICP-OES results shows that 80% of the samples collected samples tested have dangerous levels of lead contamination. Moreover, as heavy metal analysis is not commonly done on cosmetics, the development of the spiked cosmetic standard was developed, for use in testing and optimizing the alternative analysis method. The work in this chapter is under preparation to be submitted to *Analytical Chemistry*. This work was done in collaboration with Dr. Toni Barstis from Saint Mary's College and the University of Notre Dame. Dr. Barstis performed all the inductively coupled plasma experiments, including validation experiments of protocols developed and initially tested at CSU. Without her contribution, this work would not have been possible. All remaining experiments were performed by K. McMahon.

2.2 INTRODUCTION

Exposure to heavy metals can lead to a cascade of potential health concerns including, but not limited to cancer, respiratory diseases, kidney disease, and nervous system and skeletal damage.^{1,2} Human and animal exposure to heavy metals can occur from a variety of sources, including water, food, soil and consumer products such as cosmetics.^{3,4,5} Heavy metals are

naturally occurring elements in the Earth's crust with high densities in comparison to water. Key elements include lead (Pb), cadmium (Cd), mercury (Hg), and chromium (Cr) as well as essential nutrients iron (Fe), copper (Cu), zinc (Zn), and nickel (Ni).⁶ For the purposes of this research, heavy metals include transition metals, post-transition metals, and the metalloid arsenic (As), due to its toxicity. Metals like Pb, Cd, and Hg are considered highly toxic and have no biological role while heavy metals like Fe, Ni, and Cu are necessary nutrients but in excess can cause several adverse health effects.⁷

Despite regulations meant to minimize exposure, heavy metals continue to leach into sources that humans interact with regularly.⁸ Heavy metals are introduced into the environment through industrial, domestic, technological, and agricultural practices and through natural sources like weathering and volcanic eruptions.⁹ For example, activities like mining can produce waste with high levels of heavy metals that contaminate water sources.¹⁰ Heavy metals from contaminated water sources can be then transferred to other mediums like soil, plants, and food, which then leads to human and animal exposure.^{11,12} Depending on the metal and the type of exposure, permitted heavy metal concentrations by the World Health Organization (WHO), Environmental Protection Agency (EPA), and the Food and Drug Administration (FDA) can range from 0.5 ppb – 50 ppm.¹³ Heavy metal exposure from cosmetics has been largely overlooked, however, many cosmetics can contain dangerous levels, especially in developing countries.

Heavy metals are often present in cosmetic products, stemming from either matrix impurities or ingredients used in color pigmentations.¹⁴ For example, silicate mineral additives often found in eye shadows, lipsticks, care creams, and makeup powders can introduce trace levels of metal impurities into the product.¹⁵ Cosmetics most often contain Pb, Cd, Fe, Cu, Ni, Ti, Zn, and in rare circumstances, As and Hg.⁴ The FDA permits a range of heavy metal concentrations in

cosmetic products, depending on the metal toxicity. The United States regulations permit Pb concentrations up to 10 ppm and As concentrations in color additives up to 3 ppm.¹⁶ The European Union and Canada also have policies for metals in cosmetics, but in most other parts of the world, there is little regulation. Due to this lack of regulation, several studies have found regions in Asia, the Middle East, and Africa where heavy metal concentrations in cosmetics are dangerously high.^{17-20,12} For example, Surma eyeliners are often applied to children for cultural and medicinal traditions in addition to standard beauty routines.^{21,22} One study showed that Pb and Cd levels in Surma related cosmetic products ranged between 51.1 – 4839.5 ppm and 1-158.6 ppm respectively, which is substantially higher than FDA regulated levels (10 ppm).²³

Dermal exposure to heavy metals is generally considered less dangerous than ingestion; however, it can still have a significant impact on human health, as the metals can bioaccumulate over time.²⁴ The use of contaminated cosmetics can lead to metal accumulation in the skin layers causing dermatitis or the metals can be transported through skin layers, entering the blood stream, leading to a cascade of moderate to severe health effects.^{25,26} One study showed that Pb can be rapidly absorbed through the skin via sweat glands and hair follicles, and was later detected in blood, urine, or sweat.²⁷ Therefore, the development of an easy to use, cost effective platform capable of analyzing trace metal concentrations in cosmetics is critical.

Several analytical methods are currently available for heavy metal quantification in cosmetics. These include inductively coupled plasma optical emission spectroscopy, atomic absorption spectroscopy, and atomic fluorescence spectroscopy.²⁸ The current gold standard garnered by the U.S. Environmental Protection Agency (EPA), and used by the FDA is inductively coupled plasma mass spectrometry.^{29,30} While all these methods are sensitive, accurate, and suitable for trace metal analysis, they are cost-prohibitive, time-consuming, and require extensive

training. Further, samples must be collected in the field and transported back to laboratory settings for analysis. This makes it particularly difficult for resource limited areas to perform any kind of heavy metal testing. Additionally, sample preparation for analysis poses another significant obstacle.

Cosmetic matrices are complex and generally consist of lipids, organic absorbers, and other organic additives, rendering extraction of heavy metals from cosmetic samples complicated. Therefore, coextraction of matrix components along with the metal ions becomes the primary hinderance.¹⁵ Secondly, a preparation technique that can be applied to a variety of cosmetic products is challenging, due to the diversity of the cosmetic matrices. Organic additives in the cosmetics can bind to the metal ion impurities, hindering metal lability, which is crucial for detection. Therefore, aggressive sample preparations are required to free any complexed metal.³¹ Standard methods for sample preparation use strong acids and bases at high temperatures in a controlled environment to destroy the matrix while simultaneously capturing the metals.³² Examples include microwave-assisted or close vessel acid digestions with combinations of nitric acid, hydrochloric acid, perchloric acid, and hydrofluoric acid.^{30,32} These acids are considered hazardous, requiring controlled operating conditions, further increasing the cost and time of analysis. Alternative, safe methods of sample preparation are of significant interest to not only decrease the cost of analysis but to enable analysis to be done by individuals with less training and expertise safely.

To analyze the cosmetic samples in the field or in low resource settings, an alternative sample preparation protocol that avoids using any hazardous reagents is necessary. Soil samples are the closest related matrix to cosmetic products. Several studies have demonstrated successful implementation of less hazardous extraction protocols for analysis of heavy metals in soil samples.

Examples include the use of extraction solutions containing weak or diluted acid/bases, chelating agents, and redox manipulators.³³ While soil samples have a similar matrix to cosmetics, they are still less complex and can be “cleaned” with more ease. Therefore, the successful extraction of metals from cosmetic samples remains elusive.

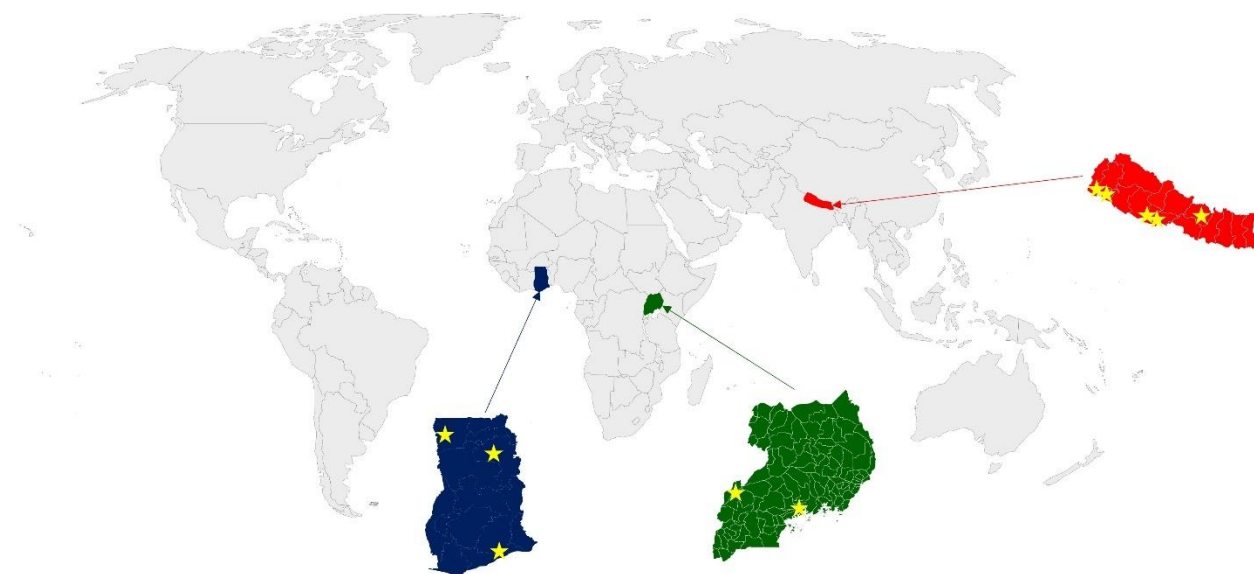
Electrochemical approaches, in particular, anodic/cathodic stripping voltammetry, have been demonstrated as a suitable method for analysis of heavy metals, with sub part per billion (ppb) detection limits.³⁴ Stripping voltammetry techniques have been used in trace metal ion detection for two primary reasons; the accumulation of the metal ions on the working electrode allows for preconcentration and the voltage pulses during the stripping step produces a high signal to background ratio, yielding high sensitivity of the assay.³⁵ However, portable and nontoxic electrode materials have been a major hinderance. Recent work has looked at stencil-printed carbon electrodes (SPCEs) for trace metal ion detection, which can be fabricated from non-toxic materials.³⁶⁻⁴¹ The electrodes are fabricated from glassy carbon, a form of graphitic carbon, and when used in combination with a bismuth film, generate well resolved voltammograms for trace metal ions.³⁶ The bismuth is electrodeposited onto the working electrode to form a stable alloy with the metal ions, and shows similar electrochemical performance to traditional mercury-film electrodes, but without any added toxicity.^{34,37}

The work described herein outlines an alternative method for the analysis of cosmetic samples from resource-limited settings. Analysis of varying levels of heavy metal contamination in eyeliner samples are first shown, examined with traditional digestion and analysis methods to demonstrate the need for routine analysis of cosmetics. An alternative extraction method coupled with an electrochemical technique is then described. To test the new method, a cosmetic standard was developed, to mimic a true cosmetic matrix with heavy metal contamination.

2.3 Materials and Methods

Cosmetic Sample Collection

Cosmetic samples were collected in Nepal in June of 2019, in Ghana in December of 2019, and Uganda in January of 2020. A variety of sample types were chosen. Samples of particular interest included any product labeled with “surma” or “kohl”, as those ingredients are banned in the US and have been shown to contain high levels of Pb, among other toxic metals. 17 samples were collected and stored at ambient temperatures prior to analysis.



Schematic 2.1: Map of the three countries where eyeliner cosmetic samples were collected. Stars represent the regions in each country where the sample was obtained.

Table 2.1: List of collected in Nepal, Ghana, and Uganda. Brands are reported as seen on the label of the cosmetic, and the matrix was determined from the label and physical examination.

Country	Brand	Matrix
Nepal	S.O.N.A.T.A Eye Liner Selfish	Liquid
	S.O.N.A.T.A Premium Eye Liner	Liquid
	Surma Mamira	Solid/powder
	Perfect Eyeliner	Waxy paste
	Sheetal	Waxy paste
	Homemade child eyeliner	Dried solid
	Ashok	Solid/powder
	Eye Improvement Powder	Solid/powder
	Surma Mamira	Solid/powder
Ghana	Al-Asmad	Solid/powder
	Kohl Al-Sherifain	Solid/powder
	Lateef Surma	Solid/powder
	Mumtaz Delux Kajal Cold	Waxy paste
	Mumtax Delux Kajal	Waxy paste
	Khojati Surma No. 13 Black	Solid/powder
	Hind Noor Eye Liner	Solid/powder
	Mumtaz Delux Kajal Cold	Waxy paste
Uganda	Starlet Kojal	Waxy paste
	Starlet Kojal	Waxy paste

X-Ray Fluorescence Spectroscopy

An Orbis Micro-XRF Analyzer was used with a 30mm² Silicon Drift Detector, rhodium x-ray source, and 30um PolyCap sensor. Samples did not undergo any preparation steps other than creating uniform physical surface for detection of the stage platform.

Cosmetic Sample Digestion for ICP-MS

Approximately 50 mg of each sample powder/liquid was weighed into pre-cleaned 15 mL Savillex® Teflon beakers. 4.0 mL of double-distilled (DD) concentrated (16N) HNO₃ (Sigma Aldrich) was added to each sample and placed on a hotplate to reflux at 200°C for 48h. Samples were subsequently removed from the hotplate and cooled for 1h. Any sample residue adhered to the sides of the beakers was rinsed with 18 MΩ cm⁻² water. The samples were then placed on the

hotplate at 110 °C to dryness. 2.0 ml of DD 16N HNO₃ was added to the dried samples, and beakers were recapped and placed on the hotplate at 200 °C for 48h. Samples were again removed from the hotplate and cooled. Two or three drops of 30% hydrogen peroxide were added to each sample. Once the reaction subsided, the samples were placed on the hotplate again for 60 min. This process of removing the sample to cool and adding H₂O₂ and DD concentrated HNO₃ was repeated until there was no further reaction. Samples were placed on the hotplate at 110 °C to evaporate to dryness. Subsequent to this last evaporation cycle, 3 mL of concentrated DD HNO₃ was added and then diluted to a final volume of ~100 mL with 18 MΩ cm⁻² water. Aliquots from the digested solutions were used for both trace elements and isotopic measurements.

Inductively Coupled Plasma Mass Spectrometry

Trace element concentrations of all solution aliquots were collected on a Nu Instruments AttoM High Resolution (HR) inductively coupled plasma mass spectrometer (ICP-MS). All trace element analyses were conducted in wet plasma mode in medium mass resolution ($M/\Delta M \approx 2500$), and at the start of each analytical session the instrument was tuned and calibrated using a multi element solution (Li, B, Na, Si, Sc, Co, Ga, Y, Rh, In, Ba, Lu, Tl, and U; 1 ng/g). Indium and Rhenium were used as an internal standard to monitor and correct for instrument drift and matrix effects. Trace element abundances were calculated based on an external calibration technique.

Spiking Procedure (creation of lead-spiked cosmetic standard)

A lead-spiked cosmetic standard was not commercially available, so one was made using the cosmetic Coty Airspun Loose Face powder. 2.0 grams of the Airspun cosmetic was mixed with 5 mL of 50 ppm Pb²⁺ standard (Atomic Absorption Lead Standard (Sigma-Aldrich) for 48h while rotating at ~40 rpm. The samples were gravity filtered with W40 filter paper; both the filtrate and filtride conserved. The filtride was allowed to dry completely (~12h).

Extraction Solution

An extraction solution was adapted from previous literature with modifications.³³ Briefly, 250 mL of 0.5 M citric acid, at pH 2 was prepared by adding solid citric acid (Sigma-Aldrich) to deionized water. Solution was pH adjusted using either HCl or NaOH until desired pH was reached and solution was brought to volume.

Extraction procedure

0.2 g of cosmetic sample was added to 5 mL of 0.5 M citric acid, pH 2, and incubated for 2h at ~40 rpm. Samples were suction filtered with W40 filter paper; both the filtrate and filtride conserved. The filtride was allowed to dry completely (~12h).

Cosmetic Sample Digestion for ICP-OES

For each sample, 50 mg of sample was weighed and placed into a CEM MARS6 Microwave Digester tube. 5 mL of trace-metal grade, concentrated (16N) HNO₃ was then added to each sample, and all tubes were loaded into the CEM carousel. The pre-programmed CEM “USP RM Organic” digestion method (1030-1800 Watt power, 20-25 min ramp time, 15 min hold time at 210°C) was used to microwave digest the samples. Following digestion, the samples were allowed to cool for at least 20 min. Each tube was carefully opened, and the contents were transferred to a Falcon tube and diluted with 20-25 mL of deionized water.

Inductively Coupled Plasma Optical Emitting Spectra (ICP-OES)

ICP-OES analyses of the cosmetic samples were conducted at the Center for Environmental Science and Technology (CEST) at University of Notre Dame using the Perkin Elmer Optima 8000 ICP-OES with Prep3 instrument. At the start of each analytical session, the instrument was calibrated using standard Pb²⁺ (Atomic Absorption Lead Standard (Sigma-Aldrich) solutions, 0-

10 ppm. Yttrium was used as an internal standard to monitor and correct for instrument drift and matrix effects. Lead concentrations were calculated based on the standard calibration curve.

Stencil Printed Carbon Electrode Fabrication

SPCEs were fabricated according to previous literature with no modifications.³⁶ Briefly, 2 g of glassy carbon (Sigma-Aldrich) was combined with 1.8 g of commercial carbon ink (Ercon). Using a precut transparency stencil cut with a CO₂ Epilog laser, the electrodes were printed onto a separate transparency sheet and dried at 65 °C for 30 min. Ag/AgCl ink (Sigma Aldrich) was painted onto the right electrode to serve as the reference electrode and dried at 65 °C for 30 min.

Electrochemical Measurements

Deposition and stripping parameters were adapted from previous work.³⁶ All buffer, pH and bismuth concentrations were replicated with minor modifications to the electrochemical parameters. 0.1M, pH 4 acetate buffer was made using sodium acetate (Sigma Aldrich) and trace-metal grade acetic acid (Fischer Scientific). Atomic Absorption Lead and Bismuth Standards (1000 mg/mL) (Sigma-Aldrich) were used to create various concentrations for the calibration curves. Before deposition, electrodes were cleaned using chronoamperometry at 0.4V for 120 s, using 50 μL of 0.1M acetate buffer, pH 4. 50 μL of Pb²⁺ standards and cosmetic samples were used for all measurements.

Standard Addition Curves

A 10 ppm Pb²⁺ standard, made from an Atomic Absorption Lead Standard (1000 mg/mL) (Sigma-Aldrich) were added to the unknown sample, in 10 or 20 μL aliquots up to a total of 40 μL. All generated curves were fit to a linear regression model, and the lines of best fit were used to calculate the x-intercept. The unknown concentration was calculated using Equation 2.1. V_s is the x-intercept, C_s is the concentration of the standard, and V_x is the volume of the standard.

$$C_x = - \frac{-(V_S)_0(C_S)}{V_x} \quad \text{Equation 2.1}$$

2.4 Results and Discussion:

Cosmetic Sample Preliminary Analysis

A handful of samples collected from Nepal were analyzed using X-Ray Fluorescence (XRF). Liquid or gel samples were not analyzed due to the incompatibility with the matrix and sample set-up in the instrument. Preliminary analysis was done using XRF because it is non-destructive and often used to understand the composition of trace metals in environmental samples.^{42,43} As seen in **Figure 2.1**, the cosmetic samples contain a variety of heavy metals and other inorganic matter, including toxic metals of interest Pb, As, and Cr. Micronutrients such as Fe, Ca, Zn, and Cu were detected in high abundances, which is not unexpected as they are often used as additives. As the instrument and samples were not calibrated for quantitative analysis, only qualitative information was gathered.

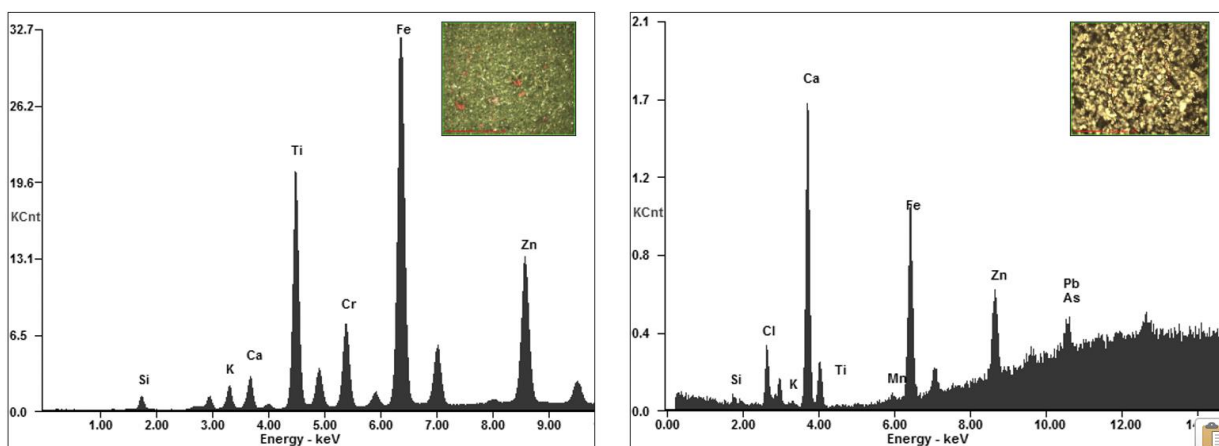


Figure 2.1: Representative X-ray fluorescence spectra of Nepali eyeliners from the Southwest region. Spectra represents relative abundances of inorganic species at the location of the x-ray source.

Using the data collected from the X-ray fluorescence experiments, Cr, As, and Pb were chosen to be analyzed with inductively coupled plasma mass spectrometry (ICP-MS). Four black eyeliner samples were tested, all of various matrixes. Black eyeliners were chosen, due to their

higher probability of containing Pb contamination, due to the dark pigmentation.⁴⁴ As seen in **Table 2.2**, all three metals of interest were found in the samples. In two of the samples, S6 S-3 and S1 SW-6, the Pb concentrations were 503 and 1543 ppm, respectively. This is 50x and 150x the amount of Pb permitted in cosmetic products by US regulations. The Cr and As concentrations were below the permitted levels for all samples. As Pb was seen in all samples with varying concentrations, further analysis was focused solely on Pb contamination.

Table 2.2: Results of ICP-MS analysis, in mg/kg, of four eyeliner samples collected from Nepal. Samples were only run (n=1), due to limited sample inventory.

	Chromium, (mg/kg)	Arsenic, (mg/kg)	Lead, (mg/kg)
Sample 1	1.4	0.75	1543
Sample 2	0.6	0.04	28
Sample 3	0.6	0.04	3
Sample 4	1.3	0.34	503

Development of a cosmetic standard for heavy metal analysis

To develop a method that can analyze cosmetics without the need for strong acids or traditional lab equipment, a cosmetic standard containing Pb first needed to be developed, as there are no commercially available cosmetic standards for heavy metal analysis. As Pb is often an impurity in darkly pigmented cosmetics⁴⁴, a light powder, Airpsun, was used as the standard matrix to ensure Pb was not present prior to being added. The powder was mixed with a 50-ppm aqueous Pb solution and incubated for 48 hours, while rotating. The rotation ensures that the powder interacts with the Pb solution evenly. An aqueous solution of Pb was chosen to ensure the Pb was fully solubilized, increasing the likelihood of it chelating with the ingredients in the powder. The

“spiked” powder was then filtered, to remove any excess liquid and allowed to dry. The spike efficiency was determined by digesting the “spiked” sample and measuring the total Pb content using ICP-OES. Both the filtrate and filtrides were analyzed, to be able to determine the percent loss of Pb (**Table 2.3**). The majority of the Pb should remain in the filtride if the spiking protocol was successful.

Table 2.3: Average Pb²⁺ concentrations from the ICP-OES results of the Airspun sample digestion. The filtride was digested for analysis of total [Pb²⁺] conjugated to the Airspun matrix. Filtrate was digested for analysis of total [Pb²⁺] not conjugated to the sample. Percent loss was calculated using the difference. Mg/L was converted to mg/kg, to account for mass of the cosmetic powder. Mass and volume of the sample were taken into account when calculating concentrations.

	Theoretical [Pb²⁺], (mg/kg)	Measured [Pb²⁺], in filtride (mg/kg)	Measured [Pb²⁺], in filtrate (mg/kg)	[Pb²⁺] loss, (mg/kg)	Percent Loss (%)
“Spiked” Airspun	1249 ± 0.6	971 ± 40	0.6 ± 0.01	278	22

On average, there is a percent loss of ~22% of the total Pb spiked into the cosmetic, equating the standard to have a concentration of ~40 ppm Pb²⁺. The loss is likely a result of the manual filtration process. During filtration, a small portion of the cosmetic powder would get trapped in the filter paper and is unrecoverable. This is further verified by comparing the dry weights of the spiked cosmetic before and after filtration. Prior to filtration, the total mass weight was 6.00 grams. After spiking, the sample weighed 5.04 grams, resulting in approximately one sixth of total mass loss. The spiking method proved reproducible (n=5) and was used for the development of a preliminary extraction solution, with a concentration of 40 ppm. The sample discussed above is representative and presents the average result of all Airspun standards made. For each batch of standard made, it was quantified on ICP-OES prior to use.

Development of Heavy Metal Extraction Solution

To make metal analysis more available in resource limited settings, the elimination of toxic reagents is necessary. Traditional sample preparation involves destroying the sample matrix and extracting out the metals of interest with concentrated strong acids and high temperatures. This ensures there are no matrix interferences during measurement, allowing complete dissociation of the metal ions from chelators. To address this, alternative extraction approaches can be developed. Elements to consider are reagents that can break down matrix components, releasing the metal ion into solution or the promotion of ion-exchange, both of which can increase lability and decrease chelation. Therefore, rather than seeking to destroy the cosmetic matrix, it is only necessary to manipulate the sample enough to release the heavy metals into free solution.

Citric acid (CA) is regarded as biodegradable metal chelator, as it is a naturally available organic acid. CA contains three carboxyl groups, which all act as potential coordination centers for heavy metals and can form stable metal complexes with Pb ions.⁴⁵ Other organic acids such as ascorbic acid or oxalic acid have also been applied to metal removal in soil samples.⁴⁶ Stability constants for the biligand complexes for each of the organics acids have been previously reported in the literature⁴⁷ and are shown in **Table 2.4**, where the higher the stability constant, the stronger the ligand-metal interaction is.

Table 2.4: Reported stability constants for Pb²⁺ metal ions with ascorbic, oxalic, and citric acid.⁴⁷

Organic Acid	Log K
Ascorbic Acid	3.5, 2.98, 4.08
Oxalic Acid	5.82, 5.50, 6.33, 6.76
Citric Acid	5.92, 6.08, 6.1

For the proposed system, it is necessary to balance the ability of the metal to both associate with the ligand and consequently dissociate for analysis. CA was chosen as a starting candidate for the

extraction solution, as it capable of binding Pb with high affinity in relation to both ascorbic acid and oxalic acid, but an adjustment in solution conditions, such as pH, could release the metal ion back into free solution.

A preliminary solution composition for extraction consisted of a 0.5M CA solution at pH 2. A low pH was chosen to resemble typical digestion pH's, to maximize the amount of matrix destruction. A 0.5M solution was tested, as anything higher than 0.5M could be potentially hazardous to bring into field settings but concentrated enough to release metal ions into solution. The Airspun standard was extracted using the solution and analyzed on ICP-OES, to understand the total Pb concentration that could be extracted, regardless of lability. Both the filtrates and filtrides were analyzed, to assess the efficiency of the extraction method. After extraction, the filtrides were subjected to traditional digestion to extract any remaining Pb in the cosmetic.

Table 2.5: ICP-OES analysis of extracted Airspun (n=5). Filtride was microwave digested following extraction, to determine total [Pb²⁺] remaining in the sample, after extraction. Extraction yield was calculated using the difference between theoretical and measured concentrations.

	Theoretical [Pb²⁺], (mg/kg)	Measured [Pb²⁺], in filtride (mg/kg)	Measured [Pb²⁺], in filtrate (mg/kg)	[Pb²⁺] loss, (mg/kg)	CA Extraction Yield (%)
Airspun Extract	971 ± 40	47 ± 2	914 ± 15	57	94

Seen in **Table 2.5**, the total amount of Pb that was extracted on average was 914 mg/kg, with 47 mg/kg left in the cosmetic. Considering the mass of the extracted sample and the volume of the extraction, this yields an extraction efficiency of 94%. This value is comparable to other CA techniques applied to lead remediation in soil and other environmental sources, while also taking less time and fewer resources.^{48,49} However, this does not account for the lability of the Pb. Small coordination complexes could be extracted using the solution, decreasing lability but having no

effect on the total Pb concentration. The filter paper was selected to be as selective for the atomic size of Pb as possible, but several small molecules could easily pass through the membrane. Since ICP-OES completely destroys any residual matrix components, the extraction efficiency is maximized, and other techniques that rely on metal lability could result in smaller extraction efficiencies.

Applying Anodic Stripping Voltammetry toward the Analysis of Heavy Metals in Cosmetics

As inductively coupled plasma optical emission spectroscopy cannot be taken out of a lab-based setting, there is an opportunity to apply electrochemical techniques toward the analysis of heavy metals in cosmetics. Electrochemical techniques for metal analysis have been widely seen in the literature, in particular, square wave anodic stripping voltammetry (ASV).⁵⁰⁻⁵² The electrode fabrication, solutions, and ASV conditions were adapted from previously published work.³⁶ The adopted protocol was designed for sub-ppb Pb analysis, and adjustments were made to produce a wider working linear range, making it more suitable for cosmetic analysis, rather than water analysis. Kava et al demonstrated that a pH of 3.6 was optimal for Pb detection, due to the uniformity and thickness of the Bi film that is formed on the surface in a slightly more acidic environment. Bi is critical to the Pb deposition on carbon electrodes, as it forms an amalgam with the Pb during deposition, increasing stability and deposition efficiency.⁵³ Despite this, when using higher concentrations of Pb, a pH of 4 showed the best result (**Figure 2.2A**). It is hypothesized that at pH 4, the Bi film is thinner. When using higher concentrations of Pb, there is more Pb present undergoing diffusion and a thicker Bi layer could hinder the electron transfer of the Pb during the stripping step.³⁹ It was also determined that lowering the frequency to 10, versus 14, improved the linear correlation at higher concentrations (**Figure 2.2B**). Frequency can impact peak sharpness and background characteristics.⁵⁴ As frequency increases, the oxidative peak current is

increased, but the peaks suffer from widening, making them less reproducible. By lowering the frequency, we improve the peak definition, allowing the higher concentration peak currents to be captured more accurately. For lower concentration levels, increasing peak current is imperative to maximize sensitivity and achieve a low limit of detection. Using the optimized conditions described above, a calibration curve was constructed in 0.1 M acetate buffer, at pH 4, and was used to quantify the labile Pb extracted from the Airspun samples throughout the remainder of the study (**Figure 2.3**). By fitting the peak currents of the extracted samples to the calibration curve (represented in red on **Figure 2.3**), and accounting for dilution factors, the labile Pb^{2+} concentration was determined in ppm.

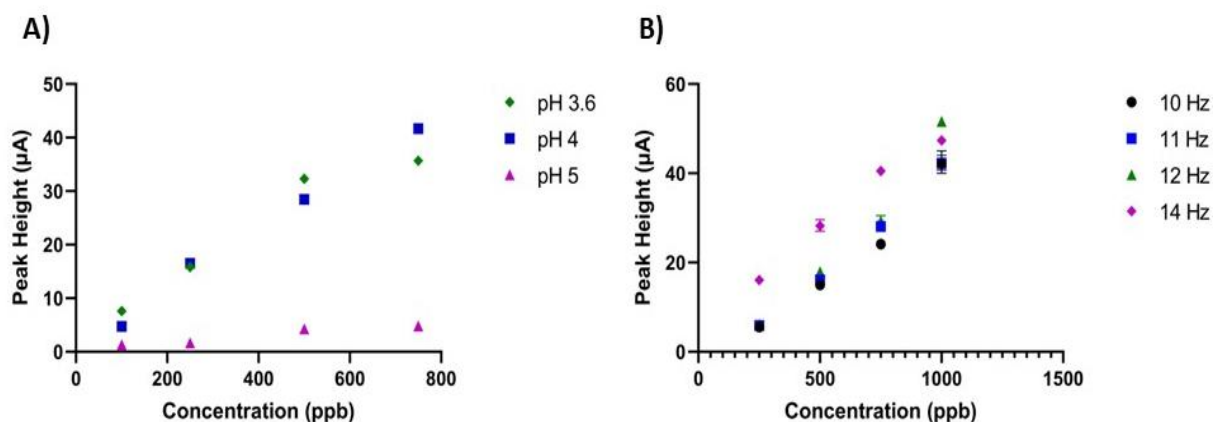


Figure 2.2: Calibration curves of Pb^{2+} to assess the optimal working linear range for A) pH and B) frequency. Optimal pH was determined using Pb concentrations from 100 – 750 ppb and frequency was determined using Pb concentrations from 250 – 1000 ppb.

To further optimize the method, a pH study and acid study was conducted, to maximize the amount of labile Pb^{2+} extracted from the Airspun samples. As such, Airspun standards were extracted using four different acids, nitric acid (HNO_3), hydrochloric acid (HCl), acetic acid, and citric acid and then run on the optimized ASV system (**Figure 2.4A**). Of the strong acids, HCl extracted the most labile Pb, which is expected due to its ability of breaking any covalent

interactions. Of the two organic acids, CA outperforms acetic acid, providing further evidence that CA is the best organic acid for the extraction of Pb from cosmetic samples. Additionally, the same Airspun standards were extracted using 0.5M citric acid solutions, ranging from a pH of 2-6 (**Figure 2.4B**). A range of pHs were tested as relevant literature has shown that pH can impact Pb extraction efficiency.^{46,49,55,56} pH 2 showed the best extraction efficiency with 83% labile Pb²⁺ extracted, whereas pH 6 showed the worst with an extraction efficiency of 62.5%. All results were validated using ICP-OES, shown in **Figure 2.4C and 2.4D** and follow the same trends as the anodic stripping voltammetry data.

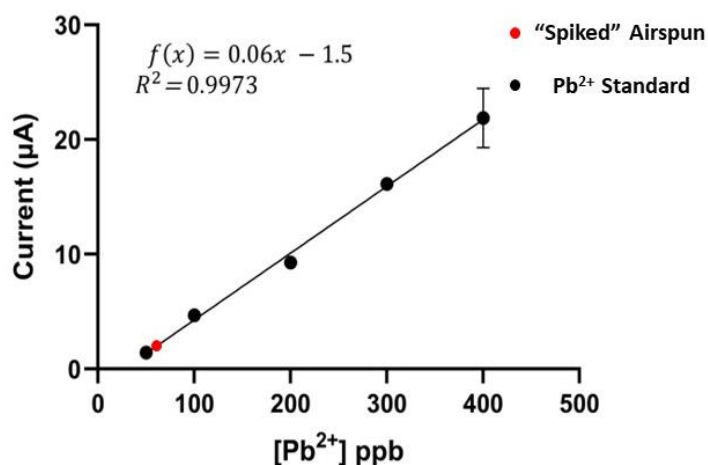


Figure 2.3: Peak heights of Pb²⁺ standards normalized to the background buffer solution, ranging from 50 – 400 ppm are plotted. All standards contained 2 ppm bismuth. The red dot represents the average peak height of the extracted Airspun samples. The final concentration of extracted lead was calculated using the line of best fit. All dilutions factors were considered.

As the ASV method can only measure labile Pb, rather than total Pb, it is likely that the Airspun matrix contains small organic ingredients that can act as chelators that are not affected by the CA and are permeable through the filtration step. It is also possible that a pH adjustment from 2 to 4 (dilution of the standard into the acetate buffer) is not enough to fully release the metal ions from the CA coordination centers. Despite this extraction efficiency being less than what is observed with ICP-OES, the data is reproducible with small error margins. Further, the method

was able to quantify Pb concentrations above what is permitted by the FDA. Therefore, the ASV analysis method and CA extraction solution is capable of Pb analysis in cosmetics with simple matrixes.

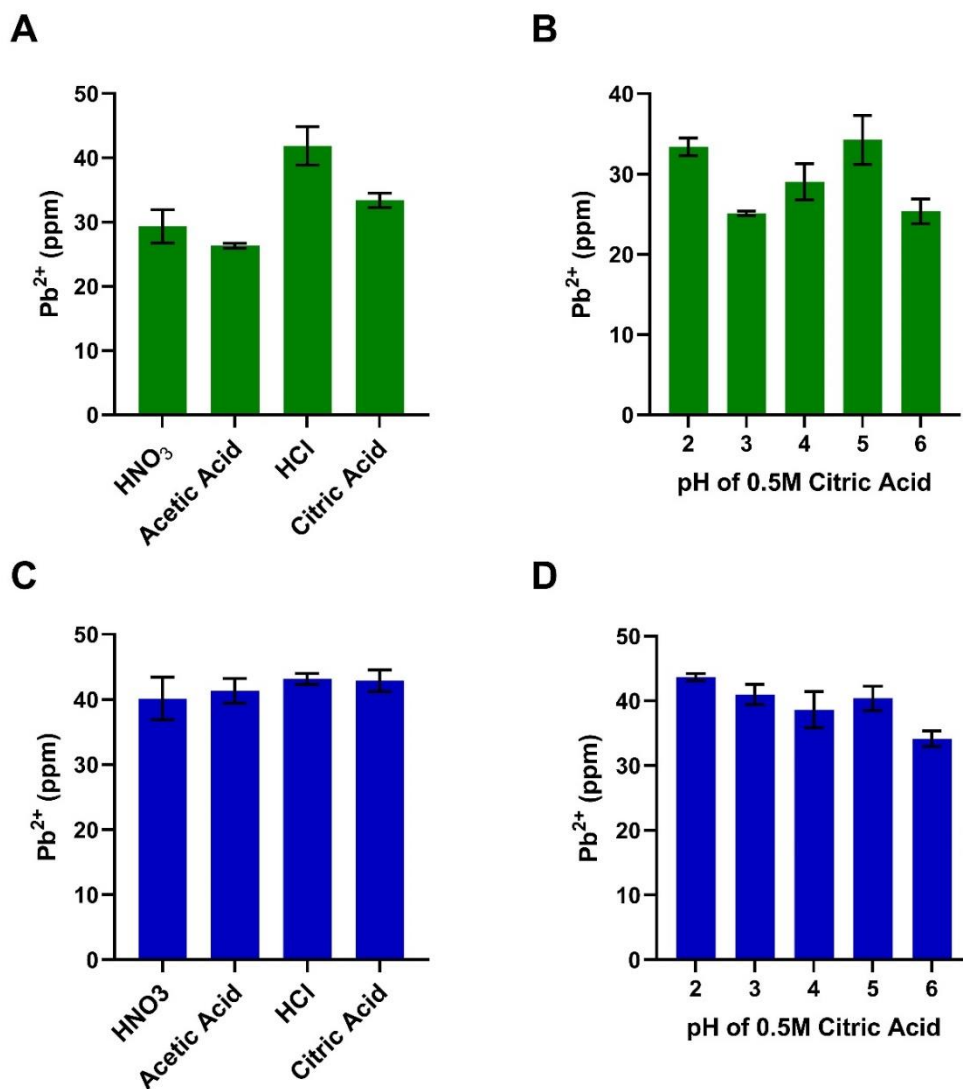


Figure 2.4: Final Pb²⁺ concentrations of the Airspun standards after extractions using different acids and different pHs. Labile [Pb²⁺] measured from Airspun standards using anodic stripping voltammetry after extraction from A) 0.5 M acids and B) 0.5M citric acid, ranging from pH 2-6. Total [Pb²⁺] measured using ICP-OES for C) 0.5M acids and D) 0.5 M citric acid, ranging from pH 2-6. The standard used for this study had an average concentration of 45 ± 3 ppm.

Testing of Real Samples using ICP-OES and ASV

ICP-OES Analysis

Since Pb concentrations were well above the ppb levels in the four samples analyzed on ICP-MS, ICP-OES was used to analyze the remaining samples. ICP-OES can be used for heavy metal analysis, much like ICP-MS, but it is a less sensitive technique. In total, 17 eyeliner samples from various regions of Nepal, Ghana, and Uganda were collected and analyzed, as shown in **Schematic 2.1**. Results are shown in **Figure 2.4**. Samples were microwave-digested, to determine the total Pb concentration of the cosmetics, shown in the blue bars. For the Nepali samples, Pb concentrations ranged from 2 ppm to ~2000 ppm. Of those samples, 67% of them were above the FDA permitted concentration of 10 ppm. Out of the Ghanaian samples, 85% were above permitted levels. Only two Ugandan samples were tested, due to limited availability of samples during collection and both samples were above permitted levels. In total, out of the 24 samples that were analyzed, 79% of them had levels of Pb contamination that exceed the FDA permitted concentration of 10 ppm.

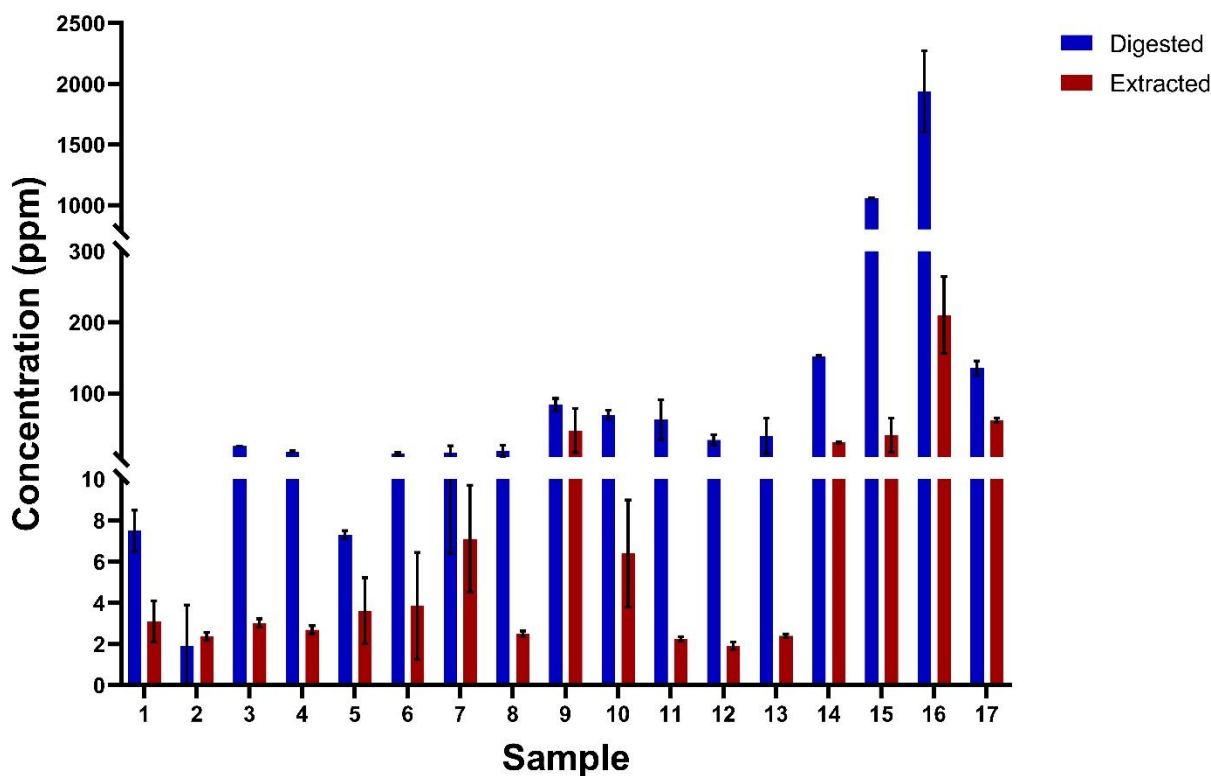


Figure 2.4: Comparison of the digested (blue) vs the extracted (red) Pb^{2+} concentration measured using ICP-OES of the 17 real samples analyzed.

ASV Analysis

As mentioned previously, the Airspun standard represents a simple cosmetic matrix. Since the CA extraction solution and ASV method were both successfully used to quantify the Pb concentration the Airspun standard, real samples were also tested, to determine the efficacy of the method on more complex cosmetic matrices. Four powder samples were tested, as their matrix most closely resembles that of the standard. Results are shown in **Table 2.6**. For all samples, Pb was measured and quantified, but the matrix had a large impact on the lability of the metal ion in the sample. Preliminary testing (not shown) of the sample using ASV showed that the labile Pb concentration was below what was quantifiable using the original calibration curve (**Figure 2.3**). To combat this, a 10 ppm Pb standard was added to the unknown sample in increasing volume to

generate a 3- or 4-point standard addition calibration curve for each sample. No more than 40 μL of standard was added, to preserve the integrity of the calibration curve and not mask the matrix effect. The standard addition plots for the four samples tested can be seen in **Figure 2.6**.

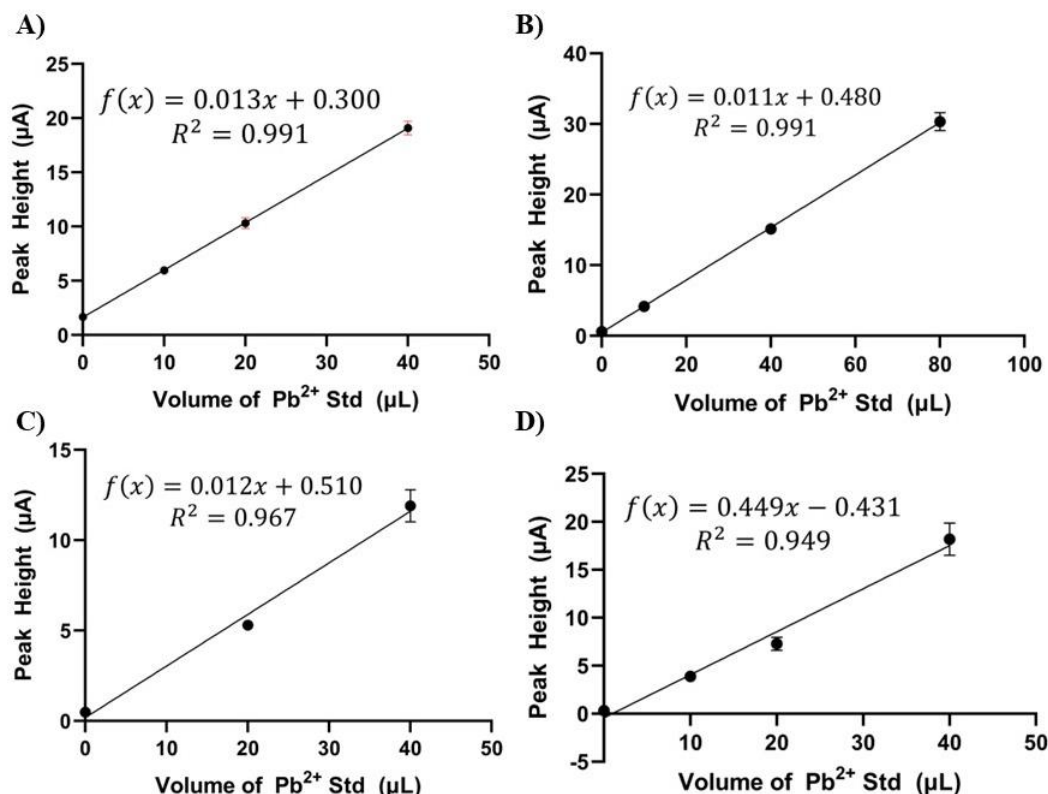


Figure 2.6: Standard addition plots of A) S-3 Surma, B) SW-6, C) N-2 Med 1, and D) N-2 Child 2. Linear regression lines of best fit were used to calculate the x-intercept. The x-intercept was then used to calculate the concentration of the unknown using the concentration and volume of the standard used using **Equation 1**. All data contains error bars, but points with small std dev are hard to see.

The calculated Pb concentrations from the standard addition curves were 8.6 ppm, 330 ppb, 1.32 ppm, 240 ppb for Samples 1-4, respectively. The extracted samples were also measured with ICP-OES, to determine the total Pb concentration extracted using the solution. Comparing the measured Pb concentrations between ICP-OES and ASV, Samples 2 and 4 had the most matrix interference with 0.5% of extracted Pb being labile, whereas Sample 1 had the least amount of matrix interference with 20% of the extracted Pb being labile. Collectively, all ASV measurements

were at least an order of magnitude below what was determined with the ICP-OES. Based on the low concentrations quantified by both the ASV and ICP method using the CA method, the complexity of the cosmetic matrixes has great impact on the utility of the approach. There are likely several potential interferents that have strong binding constants with Pb, decreasing the lability. Therefore, CA alone is not enough to extract Pb from cosmetics, and the extraction solution requires further optimization. However, all samples tested were able to be quantified to some degree using both methods.

Table 2.6: Results of Pb analysis of four cosmetic samples, used ICP-OES and ASV. All samples were extracted with the CA extraction solution. Extraction efficiency was calculated by comparing the total Pb concentration to the Pb concentration measured after extraction. Concentrations were normalized to the mass of the sample and volume of extraction solution.

	Total [Pb²⁺] (mg/kg)	ICP-OES Measurement		ASV Measurement	
		[Pb²⁺] (mg/kg)	Extraction Efficiency (%)	[Pb²⁺] (mg/kg)	Extraction Efficiency (%)
Sample 1	1058.0	41.3	3.9	8.60	0.81
Sample 2	135.6	62.3	46.9	0.33	0.24
Sample 3	1938.6	210.2	10.8	1.32	0.07
Sample 4	152.6	30.9	20.2	0.24	0.16

2.5 Conclusions

The work detailed here illustrates a strong need to analyze and monitor the heavy metal concentrations in cosmetics from low-resource settings. Digestion and ICP-OES analysis of 24 eye-liner samples shows that 80% of the samples contained hazardous levels of Pb contamination. Preliminary development of an alternative extraction and analysis method demonstrates its potential utility in cosmetic analysis, but further optimization is needed before either the CA extraction solution or the ASV method can be successfully implemented in field environments.

Despite this, the CA solution is suitable for basic matrices, such as the Airspun standard. Potential alternations to make the solution more robust include pH adjustment and the addition of calcium or ferric chloride to the solution. An increase in the pH could promote more ion-exchange between the matrix and the CA by reducing the OH groups, opening up more binding sites for the Pb ions - promoting stronger chelation. The addition of additives such as calcium or ferric chloride could enhance metal-exchange reactions through substitution reactions, increasing the extraction of Pb from the matrix. To re-release the Pb ions into solution for the electrochemical analysis, a pretreatment step could be incorporated to increase the lability. Chelation is strongly dependent on pH, therefore an adjustment in either direction could promote dissociation. Broadly, overarching efforts in cosmetic analysis need to continue to develop alternative methods that steer away from using hazardous reagents and expensive instrumentation. This work focuses on presence of Pb, but several other heavy metals could be of concern, such as mercury and cadmium.

REFERENCES

- (1) Jaishankar, M.; Tseten, T.; Anbalagan, N.; Mathew, B. B.; Beeregowda, K. N. Toxicity, Mechanism and Health Effects of Some Heavy Metals. *Interdiscip. Toxicol.* **2014**, *7* (2), 60–72. <https://doi.org/10.2478/intox-2014-0009>.
- (2) Wu, W.; Wu, P.; Yang, F.; Sun, D.; Zhang, D.-X.; Zhou, Y.-K. Assessment of Heavy Metal Pollution and Human Health Risks in Urban Soils around an Electronics Manufacturing Facility. *Sci. Total Environ.* **2018**, *630*, 53–61. <https://doi.org/10.1016/j.scitotenv.2018.02.183>.
- (3) Järup, L. Hazards of Heavy Metal Contamination. *Br. Med. Bull.* **2003**, *68* (1), 167–182. <https://doi.org/10.1093/bmb/ldg032>.
- (4) Borowska, S.; Brzóska, M. M. Metals in Cosmetics: Implications for Human Health. *J. Appl. Toxicol.* **2015**, *35* (6), 551–572. <https://doi.org/10.1002/jat.3129>.
- (5) Kaličanin, B.; Velimirović, D. A Study of the Possible Harmful Effects of Cosmetic Beauty Products on Human Health. *Biol. Trace Elem. Res.* **2016**, *170* (2), 476–484. <https://doi.org/10.1007/s12011-015-0477-2>.
- (6) Quinteros, E.; Ribó, A.; Mejía, R.; López, A.; Belteton, W.; Comandari, A.; Orantes, C. M.; Pleites, E. B.; Hernández, C. E.; López, D. L. Heavy Metals and Pesticide Exposure from Agricultural Activities and Former Agrochemical Factory in a Salvadoran Rural Community. *Environ. Sci. Pollut. Res.* **2017**, *24* (2), 1662–1676. <https://doi.org/10.1007/s11356-016-7899-z>.
- (7) Goyer, R. A. Toxic and Essential Metal Interactions. *Annu. Rev. Nutr.* **1997**, *17* (1), 37–50. <https://doi.org/10.1146/annurev.nutr.17.1.37>.
- (8) US EPA, O. *2004 National Water Quality Inventory Report to Congress*. US EPA. <https://www.epa.gov/waterdata/2004-national-water-quality-inventory-report-congress> (accessed 2019-08-15).
- (9) Tchounwou, P. B.; Yedjou, C. G.; Patlolla, A. K.; Sutton, D. J. Heavy Metals Toxicity and the Environment. *EXS* **2012**, *101*, 133–164. https://doi.org/10.1007/978-3-7643-8340-4_6.
- (10) Fashola, M. O.; Ngole-Jeme, V. M.; Babalola, O. O. Heavy Metal Pollution from Gold Mines: Environmental Effects and Bacterial Strategies for Resistance. *Int. J. Environ. Res. Public Health* **2016**, *13* (11). <https://doi.org/10.3390/ijerph13111047>.
- (11) Ahmed, M.; Matsumoto, M.; Kurosawa, K. Heavy Metal Contamination of Irrigation Water, Soil, and Vegetables in a Multi-Industry District of Bangladesh. *Int. J. Environ. Res.* **2018**, *12* (4), 531–542. <https://doi.org/10.1007/s41742-018-0113-z>.
- (12) Gupta, N.; Khan, D. K.; Santra, S. C. Heavy Metal Accumulation in Vegetables Grown in a Long-Term Wastewater-Irrigated Agricultural Land of Tropical India. *Environ. Monit. Assess.* **2012**, *184* (11), 6673–6682. <https://doi.org/10.1007/s10661-011-2450-7>.
- (13) Agency of Toxic Substances & Disease Registry. *Lead (Pb) Toxicity: What Are the U.S. Standards for Lead Levels? | ATSDR - Environmental Medicine & Environmental Health Education - CSEM*. <https://www.atsdr.cdc.gov/csem/csem.asp?csem=34&po=8> (accessed 2019-08-15).
- (14) Brzóska, M. M.; Galażyn-Sidorczuk, M.; Borowska, S. Metals in Cosmetics. In *Metal Allergy: From Dermatitis to Implant and Device Failure*; Chen, J. K., Thyssen, J. P., Eds.; Springer International Publishing: Cham, 2018; pp 177–196. https://doi.org/10.1007/978-3-319-58503-1_15.
- (15) Zhong, Z.; Li, G. Current Trends in Sample Preparation for Cosmetic Analysis. *J. Sep. Sci.* **2017**, *40* (1), 152–169. <https://doi.org/10.1002/jssc.201600367>.

- (16) Nutrition, C. for F. S. and A. FDA's Testing of Cosmetics for Arsenic, Cadmium, Chromium, Cobalt, Lead, Mercury, and Nickel Content. *FDA* **2019**.
- (17) Alam, M. F.; Akhter, M.; Mazumder, B.; Ferdous, A.; Hossain, M. D.; Dafader, N. C.; Ahmed, F. T.; Kundu, S. K.; Taheri, T.; Atique Ullah, A. K. M. Assessment of Some Heavy Metals in Selected Cosmetics Commonly Used in Bangladesh and Human Health Risk. *J. Anal. Sci. Technol.* **2019**, *10* (1), 2. <https://doi.org/10.1186/s40543-018-0162-0>.
- (18) Mousavi, Z.; Ziarati, P.; Shariatdoost, A. Determination and Safety Assessment of Lead and Cadmium in Eye Shadows Purchased in Local Market in Tehran. *J. Environ. Anal. Toxicol.* **2013**, *3* (7), 1–4. <https://doi.org/10.4172/2161-0525.1000193>.
- (19) Orisakwe, O. E.; Otaraku, J. O. Metal Concentrations in Cosmetics Commonly Used in Nigeria. *Sci. World J.* **2013**, *2013*. <https://doi.org/10.1155/2013/959637>.
- (20) Agorku, E. S.; Kwaansa-Ansah, E. E.; Voegborlo, R. B.; Amegbletor, P.; Opoku, F. Mercury and Hydroquinone Content of Skin Toning Creams and Cosmetic Soaps, and the Potential Risks to the Health of Ghanaian Women. *SpringerPlus* **2016**, *5*. <https://doi.org/10.1186/s40064-016-1967-1>.
- (21) McMichael, J. R.; Stoff, B. K. Surma Eye Cosmetic in Afghanistan: A Potential Source of Lead Toxicity in Children. *Eur. J. Pediatr.* **2018**, *177* (2), 265–268. <https://doi.org/10.1007/s00431-017-3056-z>.
- (22) Goswami, K. Eye Cosmetic 'Surma': Hidden Threats of Lead Poisoning. *Indian J. Clin. Biochem.* **2013**, *28* (1), 71–73. <https://doi.org/10.1007/s12291-012-0235-6>.
- (23) Nouioui, M. A.; Mahjoubi, S.; Ghorbel, A.; Ben Haj Yahia, M.; Amira, D.; Ghorbel, H.; Hedhili, A. Health Risk Assessment of Heavy Metals in Traditional Cosmetics Sold in Tunisian Local Markets. *Int. Sch. Res. Not.* **2016**, *2016*. <https://doi.org/10.1155/2016/6296458>.
- (24) Qu, C.-S.; Ma, Z.-W.; Yang, J.; Liu, Y.; Bi, J.; Huang, L. Human Exposure Pathways of Heavy Metals in a Lead-Zinc Mining Area, Jiangsu Province, China. *PLoS ONE* **2012**, *7* (11). <https://doi.org/10.1371/journal.pone.0046793>.
- (25) Thyssen, J. P.; Menné, T. Metal Allergy—A Review on Exposures, Penetration, Genetics, Prevalence, and Clinical Implications. *Chem. Res. Toxicol.* **2010**, *23* (2), 309–318. <https://doi.org/10.1021/tx9002726>.
- (26) *Mercury Exposure Among Household Users and Nonusers of Skin-Lightening Creams Produced in Mexico — California and Virginia, 2010*. <https://www.cdc.gov/mmwr/preview/mmwrhtml/mm6102a3.htm> (accessed 2020-05-11).
- (27) Stauber, J. L.; Florence, T. M.; Gulson, B. L.; Dale, L. S. Percutaneous Absorption of Inorganic Lead Compounds. *Sci. Total Environ.* **1994**, *145* (1), 55–70. [https://doi.org/10.1016/0048-9697\(94\)90297-6](https://doi.org/10.1016/0048-9697(94)90297-6).
- (28) Soodan, R. K.; Pakade, Y. B.; Nagpal, A.; Katnoria, J. K. Analytical Techniques for Estimation of Heavy Metals in Soil Ecosystem: A Tabulated Review. *Talanta* **2014**, *125*, 405–410. <https://doi.org/10.1016/j.talanta.2014.02.033>.
- (29) Environmental Monitoring Systems Laboratory. DETERMINATION OF TRACE ELEMENTS IN WATERS AND WASTES BY INDUCTIVELY COUPLED PLASMA - MASS SPECTROMETRY. In *Methods for the Determination of Metals in Environmental Samples*; Elsevier, 1996; pp 88–145. <https://doi.org/10.1016/B978-0-8155-1398-8.50011-2>.
- (30) Hepp, N. M.; Mindak, W. R.; Gasper, J. W.; Thompson, C. B.; Barrows, J. N. Survey of Cosmetics for Arsenic, Cadmium, Chromium, Cobalt, Lead, Mercury, and Nickel Content. *J. Cosmet. Sci.* **2014**, *65* (3), 125–145.

- (31) Buffle, J.; Altmann, R. S.; Filella, M.; Tessier, A. Complexation by Natural Heterogeneous Compounds: Site Occupation Distribution Functions, a Normalized Description of Metal Complexation. *Geochim. Cosmochim. Acta* **1990**, *54* (6), 1535–1553. [https://doi.org/10.1016/0016-7037\(90\)90389-3](https://doi.org/10.1016/0016-7037(90)90389-3).
- (32) Mesko, M. F.; Novo, D. L. R.; Costa, V. C.; Henn, A. S.; Flores, E. M. M. Toxic and Potentially Toxic Elements Determination in Cosmetics Used for Make-up: A Critical Review. *Anal. Chim. Acta* **2020**, *1098*, 1–26. <https://doi.org/10.1016/j.aca.2019.11.046>.
- (33) Peters, R. W. Chelant Extraction of Heavy Metals from Contaminated Soils. *J. Hazard. Mater.* **1999**, *66* (1), 151–210. [https://doi.org/10.1016/S0304-3894\(99\)00010-2](https://doi.org/10.1016/S0304-3894(99)00010-2).
- (34) Economou, A. Bismuth-Film Electrodes: Recent Developments and Potentialities for Electroanalysis. *TrAC Trends Anal. Chem.* **2005**, *24* (4), 334–340. <https://doi.org/10.1016/j.trac.2004.11.006>.
- (35) Barton, J.; García, M. B. G.; Santos, D. H.; Fanjul-Bolado, P.; Ribotti, A.; McCaul, M.; Diamond, D.; Magni, P. Screen-Printed Electrodes for Environmental Monitoring of Heavy Metal Ions: A Review. *Microchim. Acta* **2016**, *183* (2), 503–517. <https://doi.org/10.1007/s00604-015-1651-0>.
- (36) Kava, A. A.; Beardsley, C.; Hofstetter, J.; Henry, C. S. Disposable Glassy Carbon Stencil Printed Electrodes for Trace Detection of Cadmium and Lead. *Anal. Chim. Acta* **2020**, *1103*, 58–66. <https://doi.org/10.1016/j.aca.2019.12.047>.
- (37) Wang, J.; Lu, J.; Hocevar, S. B.; Farias, P. A. M.; Ogorevc, B. Bismuth-Coated Carbon Electrodes for Anodic Stripping Voltammetry. *Anal. Chem.* **2000**, *72* (14), 3218–3222. <https://doi.org/10.1021/ac000108x>.
- (38) Lee, S.; Bong, S.; Ha, J.; Kwak, M.; Park, S.-K.; Piao, Y. Electrochemical Deposition of Bismuth on Activated Graphene-Nafion Composite for Anodic Stripping Voltammetric Determination of Trace Heavy Metals. *Sens. Actuators B Chem.* **2015**, *215*, 62–69. <https://doi.org/10.1016/j.snb.2015.03.032>.
- (39) Phal, S.; Nguyễn, H.; Berisha, A.; Tesfalidet, S. In Situ Bi/Carboxyphenyl-Modified Glassy Carbon Electrode as a Sensor Platform for Detection of Cd²⁺ and Pb²⁺ Using Square Wave Anodic Stripping Voltammetry. *Sens. Bio-Sens. Res.* **2021**, *34*, 100455. <https://doi.org/10.1016/j.sbsr.2021.100455>.
- (40) Martín-Yerga, D.; Álvarez-Martos, I.; Blanco-López, M. C.; Henry, C. S.; Fernández-Abedul, M. T. Point-of-Need Simultaneous Electrochemical Detection of Lead and Cadmium Using Low-Cost Stencil-Printed Transparency Electrodes. *Anal. Chim. Acta* **2017**, *981*, 24–33. <https://doi.org/10.1016/j.aca.2017.05.027>.
- (41) Wygant, B. R.; Lambert, T. N. Thin Film Electrodes for Anodic Stripping Voltammetry: A Mini-Review. *Front. Chem.* **2022**, *9*, 809535. <https://doi.org/10.3389/fchem.2021.809535>.
- (42) Kilbride, C.; Poole, J.; Hutchings, T. R. A Comparison of Cu, Pb, As, Cd, Zn, Fe, Ni and Mn Determined by Acid Extraction/ICP–OES and Ex Situ Field Portable X-Ray Fluorescence Analyses. *Environ. Pollut.* **2006**, *143* (1), 16–23. <https://doi.org/10.1016/j.envpol.2005.11.013>.
- (43) dos Anjos, M. J.; Lopes, R. T.; de Jesus, E. F. O.; Assis, J. T.; Cesareo, R.; Barradas, C. A. A. Quantitative Analysis of Metals in Soil Using X-Ray Fluorescence. *Spectrochim. Acta Part B At. Spectrosc.* **2000**, *55* (7), 1189–1194. [https://doi.org/10.1016/S0584-8547\(00\)00165-8](https://doi.org/10.1016/S0584-8547(00)00165-8).
- (44) Nutrition, C. for F. S. and A. Lead in Cosmetics. *FDA* **2022**.
- (45) Zabiszak, M.; Nowak, M.; Taras-Goslinska, K.; Kaczmarek, M. T.; Hnatejko, Z.; Jastrzab, R. Carboxyl Groups of Citric Acid in the Process of Complex Formation with Bivalent and

- Trivalent Metal Ions in Biological Systems. *J. Inorg. Biochem.* **2018**, *182*, 37–47.
<https://doi.org/10.1016/j.jinorgbio.2018.01.017>.
- (46) Sun, Y.; Guan, F.; Yang, W.; Wang, F. Removal of Chromium from a Contaminated Soil Using Oxalic Acid, Citric Acid, and Hydrochloric Acid: Dynamics, Mechanisms, and Concomitant Removal of Non-Targeted Metals. *Int. J. Environ. Res. Public Health* **2019**, *16* (15), 2771. <https://doi.org/10.3390/ijerph16152771>.
- (47) Ochoa-Loza, F. J.; Artiola, J. F.; Maier, R. M. Stability Constants for the Complexation of Various Metals with a Rhamnolipid Biosurfactant. *J. Environ. Qual.* **2001**, *30* (2), 479–485.
<https://doi.org/10.2134/jeq2001.302479x>.
- (48) del Dacera, D. M.; Babel, S. Use of Citric Acid for Heavy Metals Extraction from Contaminated Sewage Sludge for Land Application. *Water Sci. Technol. J. Int. Assoc. Water Pollut. Res.* **2006**, *54* (9), 129–135. <https://doi.org/10.2166/wst.2006.764>.
- (49) Heavy metal lead(Pb) removal in contaminated soils using citric acid and malic acid as washing agents. <https://doi.org/10.21203/rs.3.rs-1862022/v1>.
- (50) Borrill, A. J.; Reily, N. E.; Macpherson, J. V. Addressing the Practicalities of Anodic Stripping Voltammetry for Heavy Metal Detection: A Tutorial Review. *Analyst* **2019**, *144* (23), 6834–6849. <https://doi.org/10.1039/C9AN01437C>.
- (51) Tesarova, E.; Baldrianova, L.; Hocevar, S. B.; Svancara, I.; Vytras, K.; Ogorevc, B. Anodic Stripping Voltammetric Measurement of Trace Heavy Metals at Antimony Film Carbon Paste Electrode. *Electrochimica Acta* **2009**, *54* (5), 1506–1510.
<https://doi.org/10.1016/j.electacta.2008.09.030>.
- (52) Munoz, R. A. A.; Angnes, L. Simultaneous Determination of Copper and Lead in Ethanol Fuel by Anodic Stripping Voltammetry. *Microchem. J.* **2004**, *77* (2), 157–162.
<https://doi.org/10.1016/j.microc.2004.02.010>.
- (53) Kachoosangi, R. T.; Banks, C. E.; Ji, X.; Compton, R. G. Electroanalytical Determination of Cadmium(II) and Lead(II) Using an *in-Situ* Bismuth Film Modified Edge Plane Pyrolytic Graphite Electrode. *Anal. Sci.* **2007**, *23* (3), 283–289. <https://doi.org/10.2116/analsci.23.283>.
- (54) Anastasiadou, Z. d.; Sipaki, I.; Jannakoudakis, P. d.; Girousi, S. t. Square-Wave Anodic Stripping Voltammetry (SWASV) for the Determination of Ecotoxic Metals, Using a Bismuth-Film Electrode. *Anal. Lett.* **2011**, *44* (5), 761–777. <https://doi.org/10.1080/00032711003790023>.
- (55) Król, A.; Mizerna, K.; Bożym, M. An Assessment of PH-Dependent Release and Mobility of Heavy Metals from Metallurgical Slag. *J. Hazard. Mater.* **2020**, *384*, 121502.
<https://doi.org/10.1016/j.jhazmat.2019.121502>.
- (56) McLaughlin, M. J.; Zarcinas, B. A.; Stevens, D. P.; Cook, N. Soil Testing for Heavy Metals. *Commun. Soil Sci. Plant Anal.* **2000**, *31* (11–14), 1661–1700.
<https://doi.org/10.1080/00103620009370531>.

CHAPTER 3: CHARACTERIZATION OF FACTORS AFFECTING STRIPPING VOLTAMMETRY ON THERMOPLASTIC ELECTRODES

3.1 Chapter Overview

Thermoplastic carbon electrodes (TPEs) are an alternative form of carbon composite electrodes that have shown excellent electrochemical performance and been applied to biological sensing. However, little has been done to apply TPEs to environmental sensing, in particular for heavy metal analysis. Based on their electrochemical properties, TPEs are expected to outperform other carbon composite materials for heavy metal analysis. However, after testing multiple formulations, TPEs showed inferior performance to previously developed carbon composite sensors for heavy metals. To examine the cause, a detailed electrode characterization was conducted. X-Ray photoelectron spectroscopy was conducted to analyze the surface functional groups, indicating that acidic and alkaline functional groups impact lead electrodeposition. Scanning electron microscopy and electrochemical characterization demonstrated that both the binder and graphite can influence the surface morphology, electroactive area and electron kinetics. The work in this chapter has been submitted to *Electrochimica Acta*, entitled “Characterization of Factors Affecting Stripping Voltammetry of Thermoplastic Electrodes”. The work was done in collaboration with Brandaise Martinez. Her contributions include aiding and/or collecting and analyzing data for the XPS and SEM experiments. All other experiments were conducted by K. McMahon.

3.2 Introduction

Carbon electrodes have become increasingly popular due to their wide applicability across a variety of fields. They have been utilized in batteries, fuel cells, capacitors, and chemical sensors.¹⁻⁵ Several different forms of carbon electrodes have been developed, including screen and stencil printed, glassy carbon, carbon paste, and carbon composite.⁶⁻¹¹ However, carbon electrodes often suffer from difficult fabrication processes and slow electron transfer kinetics in comparison to their precious metal counterparts.¹² To combat these problems, thermoplastic electrodes (TPEs) were developed. They are easily fabricated carbon composite electrodes that maintain exceptional conductivity and electron transfer kinetics.¹³⁻²⁰ Three primary thermoplastic binders have been explored for TPEs, including polymethyl methacrylate (PMMA),^{13,21} polycaprolactone (PCL),^{14,16} and polystyrene (PS).^{17,18} All binders create functional electrodes, but their individual properties greatly influence their application due to their unique surface and electrochemical properties. The type of carbon used has also been examined, including a variety of sized particles from 500 nm to 130 μm of naturally and synthetically sourced graphite.¹³

Previous work has demonstrated that PS and PCL electrodes can make effective biological sensors,^{16,22-24} but little has been done to apply TPEs to environmental monitoring. Other types of carbon-based electrochemical sensors have been developed for a variety of environmental applications and contaminants, including soil and water analysis, pesticides, and heavy metals.²⁵⁻²⁹ Heavy metal analysis is of particular concern due to multiple contamination sources leaching into common consumer products, including food and water.³⁰⁻³² In conjunction with anodic stripping voltammetry and other electrochemical techniques, carbon-based sensors have been able to detect heavy metals in water and soil sources at or below FDA and EPA permitted levels.^{33,34} However, many of these techniques require extensive surface modification, including precious

metal nanoparticles, carbon nanostructures, and complex surface additives or long incubation times.³⁵ Due to the excellent electrochemical properties of TPEs, it was hypothesized that they are suitable candidates for heavy metal monitoring without the need for extensive surface modification.

Here we characterize six different types of thermoplastic electrodes for the analysis of lead in water. Previously described binders, PMMA, PCL, and PS, are fabricated with two different carbon types (synthetic and natural), with particle size ranging from 16 μm to 130 μm , representing a spectrum of graphite used when designing carbon composite electrodes. Preliminary metal analysis indicates the use of different graphites and binders creates a broad range of surface properties which significantly influence heavy metal sensing with TPEs. Several characterization techniques, including scanning electron microscopy (SEM), X-ray photoelectron spectroscopy (XPS), and electrochemical characterization were conducted to better understand the impact of the electrode material on the sensor performance. Before TPEs can be broadly applied to biological or environmental sensors, an in-depth analysis of their physical and electrochemical properties is crucial. The studies presented in this work illustrate that lead sensing is influenced by both the surface functional groups and the surface morphologies of the thermoplastic electrodes. Further, both the binder and graphite can impact electrode performance, further affecting the ability of the electrodes to be used for metal ion sensing.

3.2 Materials and Methods

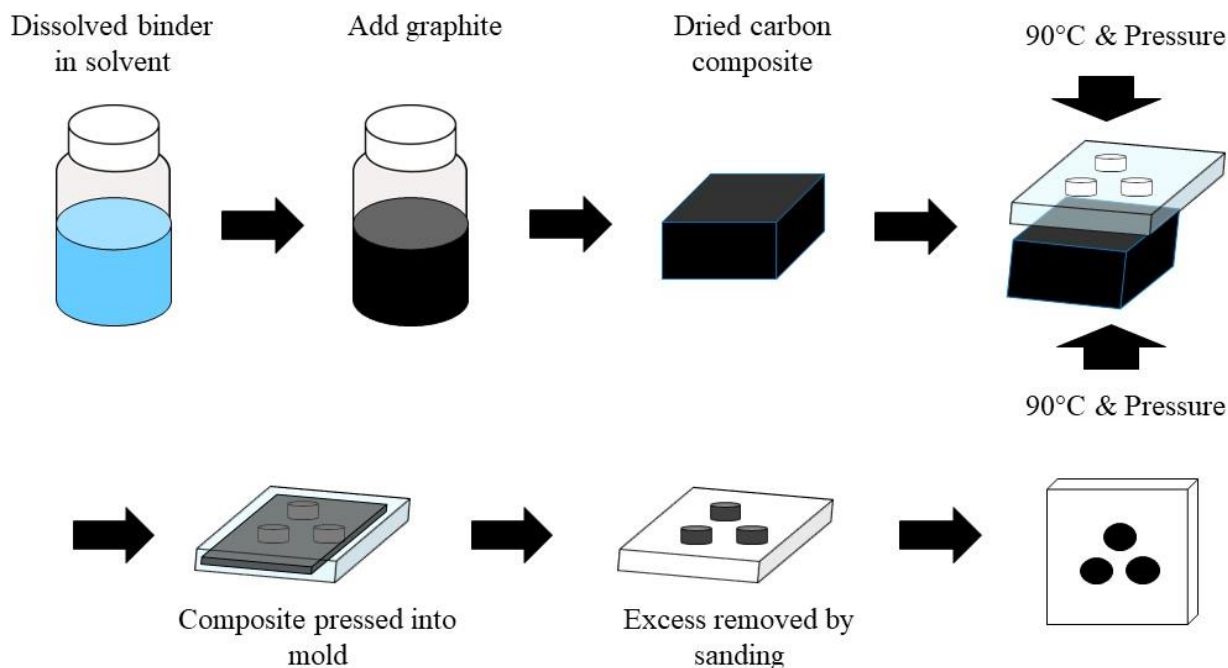
Chemicals and Reagents

Dichloromethane (DCM), ethyl acetate, sodium acetate and trace metal grade acetic acid were sourced from Thermo Fischer Scientific (Waltham, MA, USA). Potassium ferrocyanide

($\geq 98.5\%$), potassium ferricyanide (99%), potassium chloride, polystyrene 45K MW (PS), and 1000 mg/L lead and bismuth standards were sourced from Sigma Aldrich (St. Louis, MO, USA). Graphites were sourced from Asbury Carbon Mills, Inc. (Asbury, NJ, USA). Polycaprolactone (PCL) was from ThermoMorph[®] (Toledo, OH, USA) and polymethyl methacrylate (PMMA) was from Fort Collins Plastics (Fort Collins, CO, USA).

Fabrication of TPEs

All TPE formulations were pressed into three-electrode systems, as shown in **Schematic 1**. Electrode templates (3 mm WE and RE, 5 mM CE) were designed with CorelDraw (Alludo, Ottawa, ON, Canada) then laser cut out of ¼ inch bulk extruded PMMA using a CO₂ laser cutter (Epilog Laser, Golden, CO, USA). The carbon composite material was made by dissolving 1 g of the thermoplastic in approximately 15 mL of DCM (PCL and PS) or ethyl acetate (PMMA) and mixing with the graphite in a 2:1, carbon:binder ratio. Graphite was either TC303 synthetic graphite (16-30 μm) or 3569 natural graphite (33-180 μm). The resulting carbon composite was pressed into the template using a manual hydraulic heat press (Carver, Inc., Wabash, IN, USA), set at 90°C with pressures set between 1000-1200 psi. PCL and PS carbon composite materials were allowed to completely dry before pressing, whereas the PMMA material was dried to a gum-like texture before pressing. For the PS TPEs, the material was pressed into templates overnight. For PMMA and PCL TPEs, material was pressed into the templates for approximately 1 hour. Excess material was removed using wet 150 grit silicon carbide sandpaper. Solid core tinned copper wire (0.65 mm diameter) was added to each electrode using silver paint (SPI Supplies, West Chester, PA, USA) and 2-part quick set epoxy (Loctite[®], Henkel Corp., Rocky Hill, CT, USA).



Schematic 3.1: Fabrication of the thermoplastic electrodes.

Electrochemical Detection of Lead

Deposition and stripping parameters were adapted from previous work.³⁴ All buffer, pH and bismuth concentrations were replicated with minor modifications to the electrochemical parameters. Electrodes were first polished using sequential 150, 600, and 4000 grit wet silicon carbide sandpaper and allowed to air-dry. Before deposition, electrodes were cleaned using chronoamperometry at 0.4V for 120 s, using 100 μL of 0.1M acetate buffer, pH 4.0. 100 μL of Pb^{2+} standards were used for all measurements.

Electrochemical Measurements

All electrochemical measurements were performed on a PalmSens 4 potentiostat (BASi, West Lafayette, IN, USA). TPEs were polished using sequential 150, 600, and 4000 grit wet silicon carbide sandpaper. All reported potentials are referenced against a carbon pseudo-reference TPE

built into the array. After sanding, arrays were sonicated in Milli-Q water for 5 minutes to remove polishing sediments, then allowed to air-dry completely.

Cyclic Voltammetry and Scan Rates

Cyclic voltammograms (CVs) were performed at scan rates ranging from 10 mV/s – 500 mV/s in random order. Representative CVs were performed at 100 mV/s. Ferri/ferrocyanide was tested at a 1 mM concentration (1 mM of each oxidation state) in 0.1M potassium chloride. All CVs were scanned in the positive direction first and taken from -0.4V to 0.4V versus carbon pseudo-reference electrode.

Surface Morphology and Composition Analysis

Single 1 mM diameter TPE models were fabricated as described above with no wires added for ease of sample manipulation. Samples were gold sputter coated (Desk II Gold Sputter Coater, Denton Vacuum, LLC., Moorestown, NJ, USA) for 15 s to a thickness of 10 nm and scanning electron microscopy (SEM) was performed on a JEOL JSM-6500F field emission scanning electron microscope (JEOL, Tokyo, Japan) at 10 kV acceleration voltage. X-ray photoelectron spectroscopy (XPS) was performed using a Physical Electronics PE-5800 X-Ray Photoelectron Spectrometer (Physical Electronics, Inc., Chanhassen, MN, USA) equipped with monochromated Al anode producing Al $K\alpha$ x-rays, 0.8 x 0.8 mm aperture, 20 μ A electron neutralizer, and argon ion gun neutralizer. The resulting spectra were processed and analyzed via CasaXPS (Casa Software Ltd.). Optical profilometry was performed on a Zometrics ZeScope (Zygo, Middlefield, CT). Prior to each technique, the TPE models were polished, rinsed, and air-dried the same as in the electrochemical measurements.

3.3 Results and Discussion

Lead Detection on TPEs

Preliminary calibration curves were generated for all six TPE compositions for 10-200 ppb of Pb^{2+} . Seen in **Figure 3.1**, all electrode types generate resolved and reproducible peak currents for the detection of Pb^{2+} . Representative voltammograms at each concentration are available in **Figure S3.1**. The coefficient of variation ranges from 4 – 17%. The 10 ppb currents contribute the most to the variability, as expected. Across the binder types, there are minor shifts in the peak potential, which is likely a result of the differences in the potential of the carbon pseudo-reference electrodes. The variations in binder and graphite of the pseudo-references likely impacts the electrodeposition and subsequent stripping voltages of the Pb^{2+} . Both PMMA and PS electrodes were able to detect 10 ppb Pb^{2+} , while the PCL electrodes were only able to detect 50 ppb Pb^{2+} with good peak resolution. Moreover, the peak currents for PCL electrodes are substantially smaller in relation to both PS and PMMA. For the PCL electrodes, the peak heights for the 200 ppb peaks are $2.7 \pm 0.3 \mu\text{A}$ and $2.5 \pm 0.3 \mu\text{A}$ for TC303 and 3569, respectively. For the PMMA electrodes, the 3569 graphite produces more current at 200 ppb relative to TC303, with peak heights of $7.5 \pm 0.05 \mu\text{A}$ versus $5.6 \pm 0.2 \mu\text{A}$, respectively. The opposite is true of the PS electrodes with peak heights of $7.3 \pm 0.1 \mu\text{A}$ and $9.5 \pm 0.5 \mu\text{A}$ for 3569 and TC303, respectively. Comparing the relative peak heights of the six electrode types, PS-TC303 performed the best.

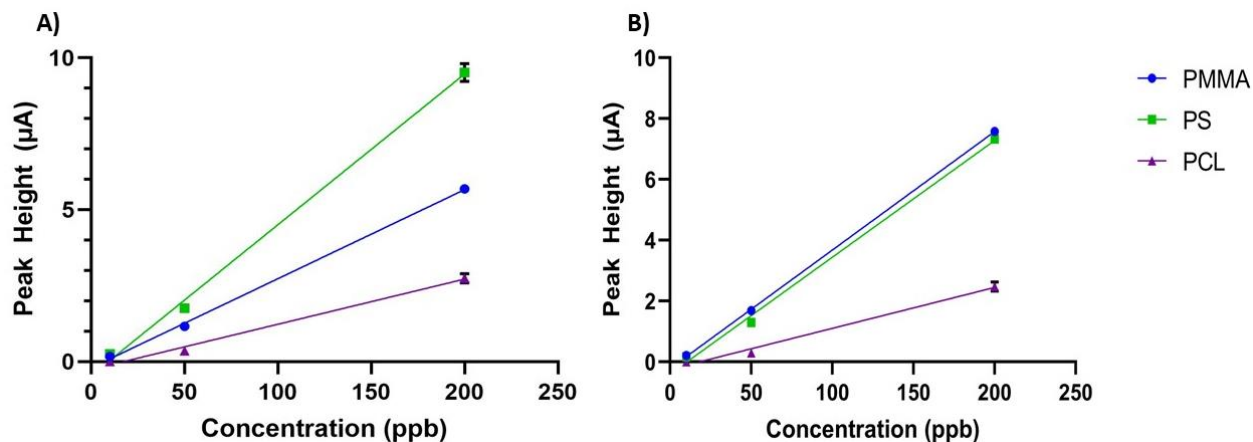


Figure 3.1. Calibration curves for 10 – 200 ppb Pb^{2+} for all six TPE formulations. Analysis was performed in 0.1M acetate buffer, pH 4, 360s deposition time, -1.4V deposition potential. A) PCL-, PS-, and PMMA-3569 TPE (n=3) peak currents fit to a linear regression model. B) PCL-, PS, and PMMA-TC303 TPE (n=3) peak currents fit to a linear regression model.

The sensitivities for each electrode type are reported in **Table 3.1** and were calculated from the calibration curves seen in **Figure 3.1**. The obtained sensitivities are below what is observed for other carbon electrodes in the literature. For example, the sensitivity of Pb^{2+} detection from Bi-coated stencil-printed carbon electrodes (SPCEs) was $0.10 \mu\text{A/ppb}$ ³⁴ and $0.08 \mu\text{A/ppb}$ ³⁶. Previous work established that TPEs are more electrochemically robust than SPCEs,¹³ which makes the lower Pb^{2+} sensitivity on TPEs surprising. The metal deposition was carried out under quiescent (diffusion-only) solution conditions and was limited by mass transport of Pb^{2+} to the electrode surface. Since the same solution volumes and concentrations were tested on each TPE formulation, it suggests that the surface properties of the TPEs are influencing metal deposition. It can be speculated that a rougher surface may deposit the same, or more, Pb^{2+} ions in relation to a smoother one, but if the graphitic edge planes are more pronounced, the re-oxidation of the Pb^{2+} could be impacted through physical hinderance. Further, surface functional groups on the electrode surface can impact the Pb^{2+} electrodeposition.³⁷ More acidic groups, such as carboxylic acids have shown higher prevalence of Pb^{2+} deposits than surfaces without, due to an increase in adsorption sites.³⁷ Additionally, a high prevalence of carbonyl or alkaline functional groups hinder Pb^{2+} deposition.

To better understand the surface chemistry and physical dynamics of the TPE electrodes, several surface characterization methods were applied to the system.

Table 3.1: The sensitivities and the R^2 values were calculated from the calibration curve for all six TPE formulations. Sensitivities and R^2 values were generated using a linear regression model, where the sensitivity is the slope of the line of best fit. Standard deviations were calculated from triplicate runs (n=3).

	TC303			3569		
	PMMA	PS	PCL	PMMA	PS	PCL
Sensitivity ($\mu\text{A/ppb}$)	0.029 ± 0.001	0.050 ± 0.001	0.015 ± 0.001	0.039 ± 0.002	0.038 ± 0.001	0.013 ± 0.001
R² Value	0.997	0.994	0.982	0.999	0.996	0.979

Surface Composition Analysis of TPEs by XPS

Depending on the graphite and binder combination, carbon composite electrodes can have different surface functional groups, leading to complex chemical interactions.³⁸ The binders differ in structure, as PCL and PMMA both have carbon chains with oxygen groups differing in length, whereas PS contains an aromatic ring, shown in **Figure 3.2**.

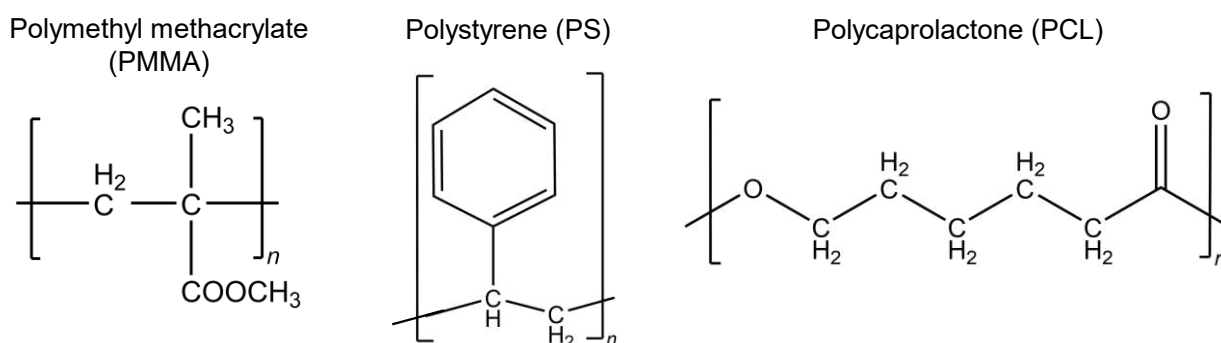


Figure 3.2. Chemical structures of PMMA, PS, and PCL, given in order from left to right.

When the electrodes are polished, the graphene sheets can become functionalized from reacting with surrounding water and oxygen, forming carboxyls, hydroxyls, and carbonyls, among others.³⁹ X-ray photoelectron spectroscopy (XPS) was used to determine the functional groups and their relative abundance on the electrode surfaces of each electrode type. Based on the survey spectra (**Figure S3.2**), there are only carbon and oxygen peaks present, as expected, indicating that there are no surface contaminants. The carbon (C1s) peaks were further analyzed via high resolution spectra to examine differences among TPE composition more closely.

Figure 3.3 shows the high-resolution spectra overlay for C1s for all six electrodes, grouped according to binder type. Qualitative analysis indicates that both the plastic type and graphite type impact the relative functional group abundance with each binder interacting with the graphite differently, as evidenced by the different functional group peak fitting for each high-resolution spectrum. Looking at the individual relative percentage abundances for the carbon-carbon and carbon-oxygen bonding (**Figure 3.4**), this observation is further validated.

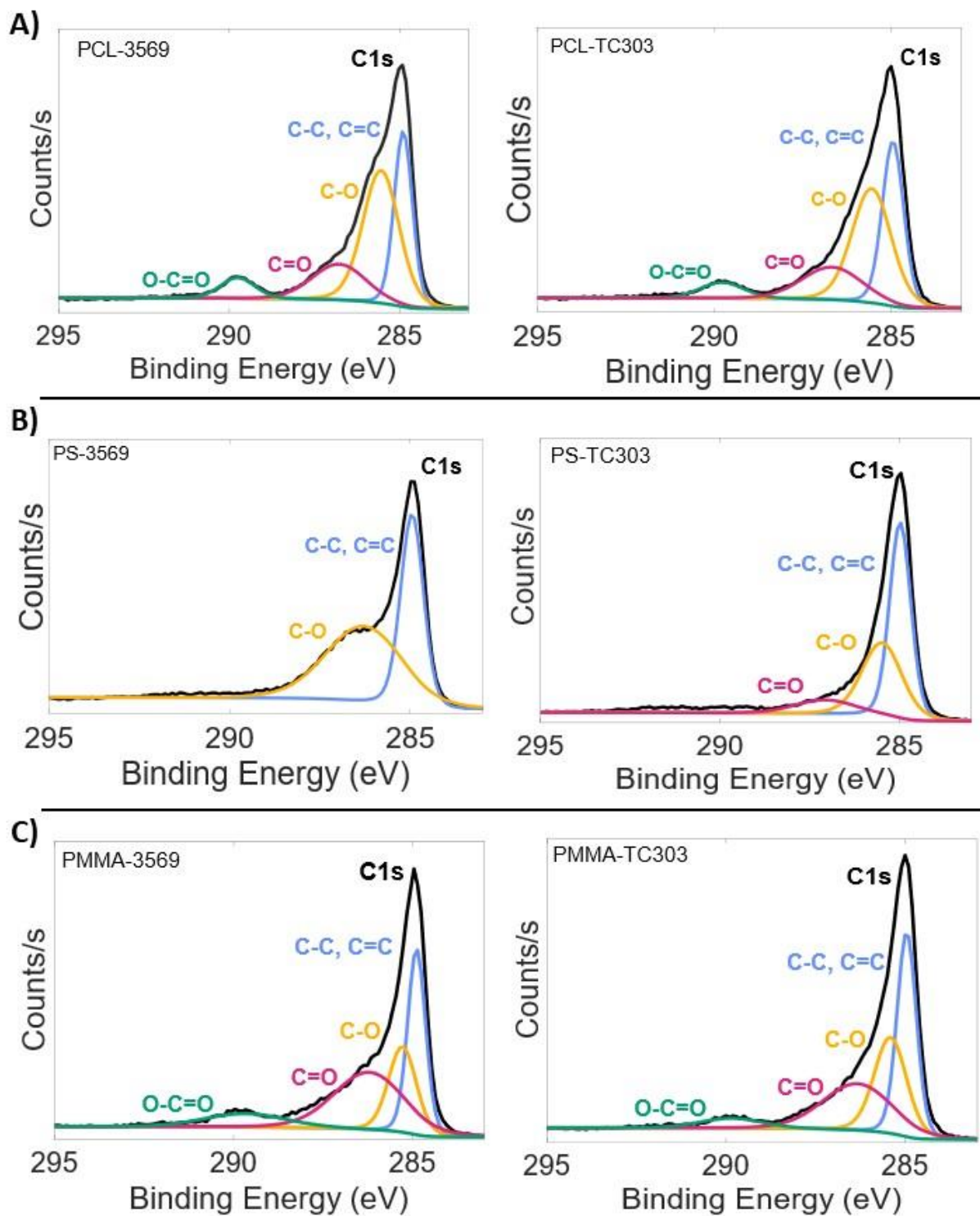


Figure 3.3: X-ray photoelectron spectroscopy high resolution C1s spectra for A) PCL TPEs, B) PS-TPEs, and C) PMMA-TPEs. Spectra were fit with CasaXPS software.

As seen by the varying degrees of the surface functional groups, the activation of the electrode surface is contingent on both the binder and graphite used. The PS electrodes are the most impacted by the size of the graphite, with PS-TC303 containing larger amounts of C-C and C-O bonds (52.8% and 36.9%, respectively) compared to PS-3569 (43.38% and 56.62%, respectively). PS-TC303 contains 10.3% of C=O and 0% of O-C=O, whereas as PS-3569 contains neither functional group. PS-TC303 has a larger fraction of C-C bonds, suggesting that the surface is comprised mainly of basal planes. PS-3569 has a greater number of carbon-oxygen bonds (C-O and C=O), suggesting that there are more edge planes, in relation to PS-TC303. As 3569 is a larger graphite in comparison to TC303, it is hypothesized that the TC303 carbon lattice is more ordered and contains fewer defects. Both PCL and PMMA contain oxygen groups, so it is expected that the oxygen abundance will be greater. In both cases, the C-C bond percentage is higher in TC303 than in 3569, supporting the theory that TC303 interactions with the binders produce more basal planes than 3569. With the increase in oxygen for both PMMA and PCL electrodes, it is hypothesized that there are more graphitic defects. However, the pattern of defects is unclear from the XPS data alone and is likely a result of various forms of graphitic defects, such as zigzag-shaped edges or arm-chair edges.⁴⁰ While the material for making the TPEs is assumed to be uniform, it is possible that the different layers of material contain heterogeneous amounts of graphite and binder. Therefore, the carbon lattices throughout the depth of the electrode would have varied levels of defects, impacting the carbon-oxygen bonds observed in the XPS data.

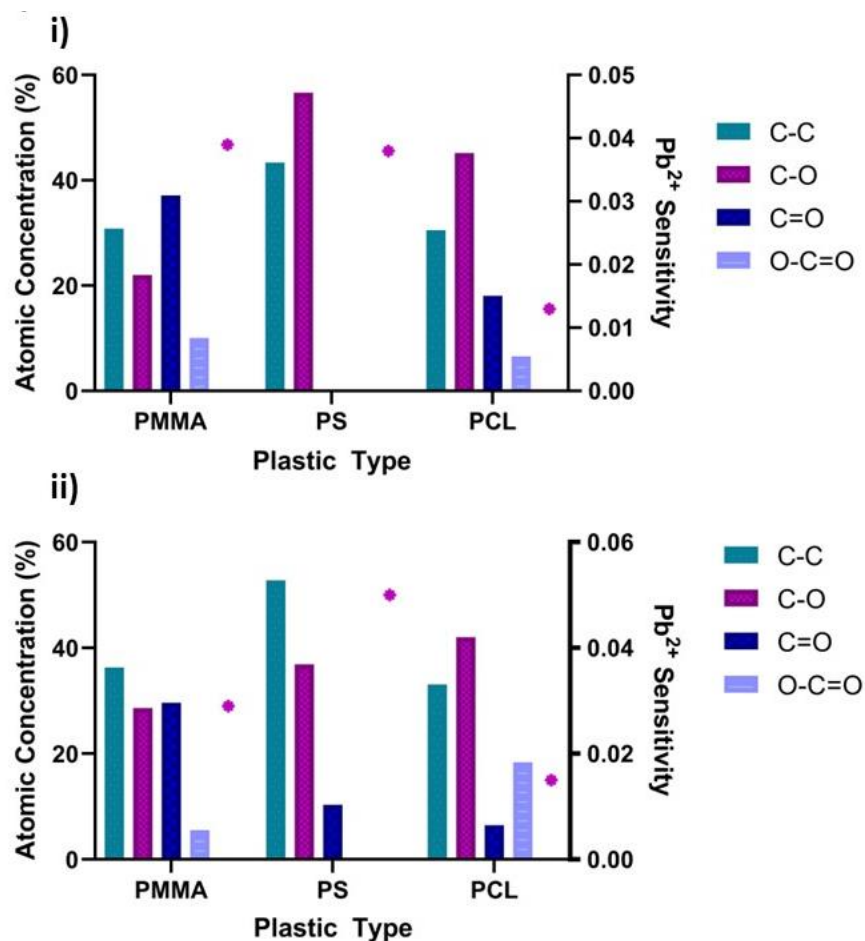


Figure 3.4. Atomic concentration percentages from high resolution XPS spectra for PCL-, PS-, and PMMA-TPEs plotted against the sensitivity of the Pb²⁺ deposition, represented by the pink star for i) 3560 graphite and ii) TC303 graphite.

Interestingly, both the PMMA- and PCL-TPEs contain higher abundances of carbonyls than the PS electrodes whereas the PS electrodes contain the highest abundances of carboxyl groups. As noted previously, carbonyl groups can have a negative impact on Pb²⁺ deposition and carboxyl groups can enhance deposition.³⁷ For the smaller graphite size (TC303), the abundance of carbonyl groups on the surface appears to have a negative impact on the Pb²⁺ sensitivity, whereas the trend is not obvious for the larger graphite, 3569. All three electrode formulations have higher levels of oxygen containing functional groups in comparison to C-C for 3569 than TC303, suggesting there is a greater number of surface defects, or edge planes. Furthermore, the sensitivities for PS and PMMA Pb²⁺ deposition are similar (0.038 ± 0.001 and 0.039 ± 0.002 ,

respectively) for 3569 ($p > 0.1$), with the PS electrode containing no carbonyl groups. This suggests that in addition to the carbonyl functional group presence, the size and shape of the graphitic defects can greatly affect the ability of Pb^{2+} to be deposited and stripped back off the electrode surface. To further investigate the structure of the electrode surfaces, scanning electron microscopy was conducted.

SEM Characterization

Scanning electron microscopy (SEM) images were taken of all six TPE formulations and are shown in **Figure 3.5** (additional magnifications are available in **Figure S3.3**). For all micrographs, there are varying degrees of surface topography. The conductive regions can be attributed to graphite whereas the regions with more charging (the brighter areas in the micrographs) are associated with the non-conductive binder. For all formulations, the surface is heterogeneous, and contain pockets of randomly oriented graphitic material. For the TC303 TPEs, PS appears to have the lowest amount of edge planes, and is primarily composed of basal planes, as evidenced by the densely packed smooth surface. There are also some smaller translucent edge planes, which could resemble graphene-like behavior. The surface roughness (R_q), determined via optical profilometry, can be correlated to the presence of edge planes (**Figure 3.6**). Further, the PS has the most uniform conductive surface, evidenced by the minimal pockets of charged material. The PMMA and PCL topographies have more ridge-like defects, which can be attributed to graphitic edge planes, but could also be a result of pockets of free binder. This is particularly the case for the PCL electrodes, where the long tubular like structures seen in both graphite images are likely bulk binder material that was not well blended with the graphite powder. For the 3569 graphite, all three binders have heterogenous pockets of graphitic material, consisting of both basal and edge planes. The PCL-3569 surface appears more densely packed, indicating the bulk material

is likely more homogeneous than the TC303 material. PS-3569 has more surface roughness in relation to PS-TC303, with more pronounced edge planes. The PMMA surfaces appear to be similar across the two graphites, with pockets of smooth and ridge-like graphitic material.

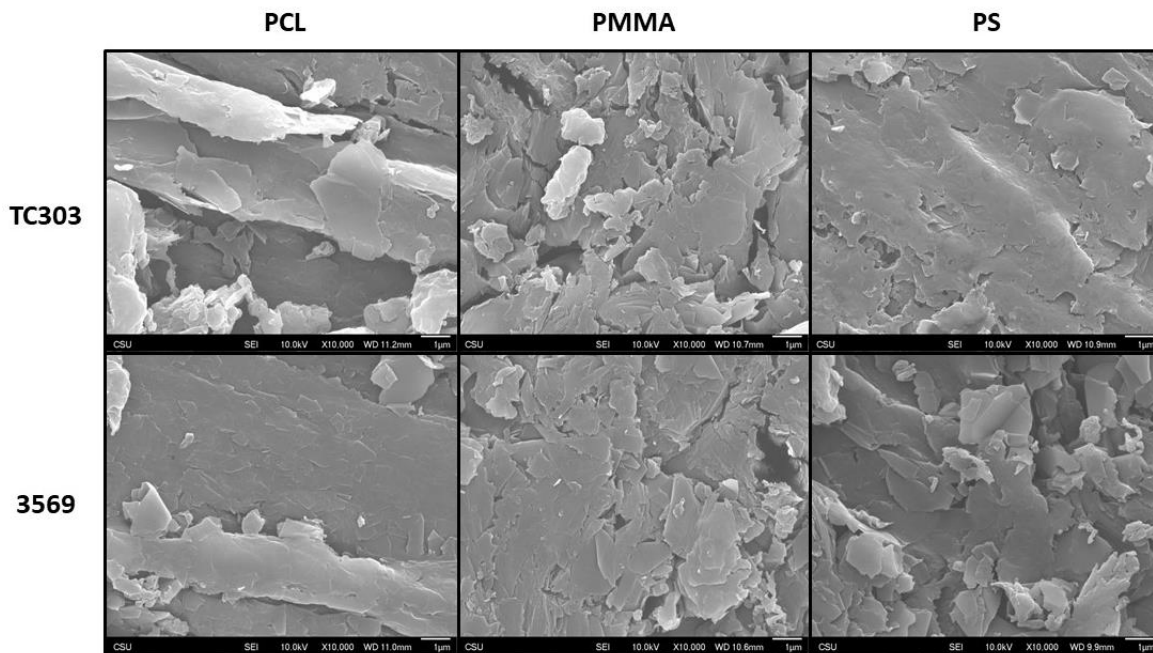


Figure 3.5: SEM micrographs at $1 \times 10^4 \times$ magnification of PCL-, PMMA-, and PS-based TPE material with TC303 graphite (top) and 3569 graphite (bottom).

For Pb^{2+} deposition, PMMA-3569 was superior to PMMA-TC303 when comparing the sensitivities (0.039 ± 0.002 and 0.029 ± 0.001 , respectively). Relating that to the surface characteristics, PMMA-3569 appears to have less defects and less charging than PMMA-TC303. However, for the PS electrodes, PS-TC303 slightly outperforms PS-3569, despite the sensitivities being similar (0.050 ± 0.001 and 0.038 ± 0.001 , respectively). For PS-TC303, the 200-ppb peak height is $2.2 \mu\text{A}$ higher than PS-3569. This leads to the conclusion that the size of the graphite is an important consideration when adapting the TPEs for various applications, and, in this case, metal sensing. For the PCL TPEs, both graphites had similar sensitivities (0.015 ± 0.001 and 0.013 ± 0.001), and the two graphites seem to produce similar surface morphologies with a mix of basal and edge planes. The PCL TPEs have the most bulk binder material observed in the SEM images,

particularly PCL-TC303. This suggests that the PCL binder produces the least homogeneous carbon composite material, which can have direct impacts on electrode function.

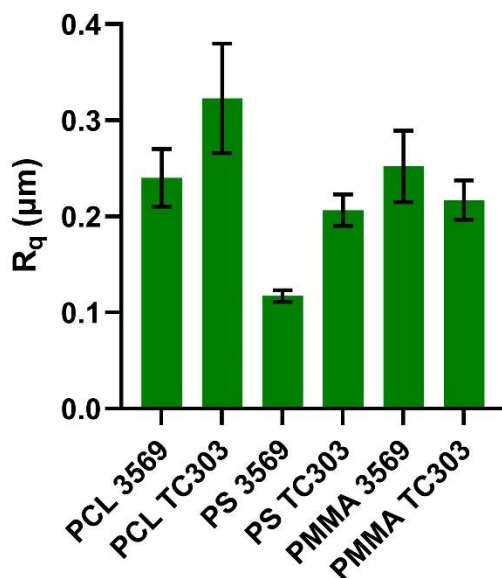


Figure 3.6. Average surface roughness (R_q) ($n=3$) of each TPE type. Error bars represent standard deviation.

Electrochemical Characterization of the TPE material

As evidenced by the XPS and SEM analysis of the TPE material, the formulation can impact both electrode surface morphology and chemistry. As seen with XPS, the surface functional groups generated by activating the carbon composite material when polishing is contingent on both the graphite and binder used. Additionally, both the graphite and binder can influence the degree and morphology of the surface defects, as evidenced by the SEM. However, all six formulations still underperform in relation to other carbon-based electrodes for Pb^{2+} analysis. Therefore, electrochemical characterization was also explored, to help understand if the different binder:graphite formulations impact electron transfer kinetics and active surface area.

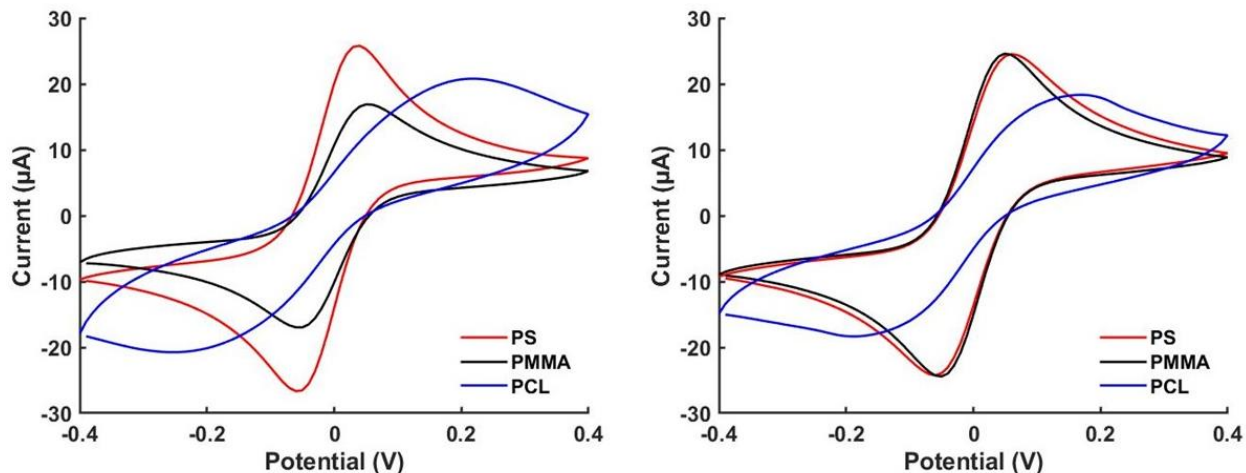


Figure 3.7. Representative CVs ($n=3$) for 100 mV/s for PS-, PMMA-, and PCL-TPEs with TC303 graphite (left) and 3569 graphite (right).

All TPE formulations were evaluated using the reversible redox couple ferri/ferrocyanide, shown in **Figure 3.7**. For the TC303 graphite, PS-TPE showed the highest oxidative current density (0.42 ± 0.01 mA/cm²) compared to PMMA (0.31 ± 0.04 mA/cm²) and PCL (0.20 ± 0.01 mA/cm²). For the 3569 graphite, the PS- and PMMA-TPE oxidative current densities were not significantly different (0.43 ± 0.03 mA/cm² and 0.41 ± 0.02 mA/cm², respectively) but were substantially higher than PCL (0.21 ± 0.02 mA/cm²). Ferri/ferrocyanide is sensitive to surface oxides, so the differences in the current densities can be attributed to the different surface roughness and the surface functional groups of each of the TPEs.⁴¹ ΔE values were also calculated for each TPE formulation. For the TC303 graphite, PS- and PMMA- electrodes were not statistically different, with ΔE values of 82 ± 4 mV and 86 ± 13 mV, respectively, indicating that both formulations have similar electron transfer kinetics. However, the PCL TPE had a much higher ΔE value of 307 ± 21 mV, suggesting that PCL can hinder electron transfer kinetics. A similar trend is observed for 3569 graphite, with ΔE values corresponding to 101 ± 15 , mV 94 ± 7 mV, and 237 ± 25 mV for PS, PMMA, and PCL TPEs, respectively. For both the PS and PMMA electrodes, the graphite appears to have a minor effect on the electron transfer kinetics, however

for PCL, the TC303 graphite has a ΔE that is 77% higher than 3569, suggesting PCL is more compatible with larger graphite particles. With PCL having the lowest current density and high ΔE values in comparison to the PS- and PMMA- TPEs, the PCL formulations are likely not suitable for applications requiring surface modification, whereas the PS and PMMA are promising candidates.

To investigate the kinetics further, the heterogeneous electron transfer rate constants, k_0 , was calculated for each TPE formulation using the Nicholson method.⁴² **Equation 3.1** was used, where ψ is the average of the ΔE of the ferri/ferrocyanide peaks for each scan rate, D is the diffusion coefficient, F is Faraday's constant, R is the ideal gas constant, ν is the scan rate, n is the number of electrons exchanged, and T is temperature (assumed 25°C).

$$\psi = k_0 \left[\frac{\pi D n F \nu}{RT} \right]^{-\frac{1}{2}} \quad \text{Equation 3.1}$$

The rate constants are shown in **Table 3.2**. The rate constants for PS- and PMMA-TPEs are similar and are comparable to glassy carbon composite electrodes ($k_0=0.005 \text{ cm}\cdot\text{s}^{-1}$).⁴³ For the PMMA-TPEs, the graphite does not appear to have a large impact on the electron transfer kinetics, as the rate constants for TC303 and 3569 differ by $0.2 \text{ cm}\cdot\text{s}^{-1}$. The size of the graphite does appear to influence the PS-TPEs, with the smaller graphite (TC303) being preferable over 3569, as the rate constant is $1 \text{ cm}\cdot\text{s}^{-1}$ higher for TC303 than 3569. The PCL rate constants are smaller by an order of magnitude and can only be estimated, as the high resistance of the electrodes adds error to the calculation, and the peak currents could be masked by non-Faradaic effects.⁴² Further, the ΔE values for PCL-TPEs exceeded 200 mV for some scan rates, which prevents accurate determination of k_0 . For both PS and PMMA, the rate constants follow the same trend as the current density, where neither graphite has a substantial impact on the PMMA TPEs, and the smaller

graphite particles is preferable for PS. This suggests that the size and orientation of the binder can impact the TPE performance.

Table 3.2: Electrochemical rate constants, k_0 , of 1 mM ferri/ferrocyanide in 0.1 M KCl in relation to differing electrode formulations. The rate constants were determined from the slopes of the linear regression lines and the error shown is the standard error of the slope.

	TC303			3569		
	PMMA	PS	PCL	PMMA	PS	PCL
k_0 ($\times 10^{-3}$ $\text{cm}\cdot\text{S}^{-1}$)	5.1 \pm 0.1	4.6 \pm 0.5	0.94 \pm 0.06	4.9 \pm 0.7	3.6 \pm 0.9	0.84 \pm 0.01

To further compare the electrodes, the electroactive surface area was calculated (**Table 3.3**). Using ferri/ferrocyanide as the redox probe, cyclic voltammograms at nine different scan rates were collected. The electroactive area was calculated using the Randles-Sevcik equation (**Equation 3.2**), where i_p is the peak current (A), n is the number of electrons transferred in the reaction, A is the electroactive surface area (cm^2), D is the diffusion coefficient ($\text{cm}^2\cdot\text{s}^{-1}$), C is the concentration (M), and ν is the scan rate ($\text{V}\cdot\text{s}^{-1}$).⁴⁴ The diffusion coefficients used were 7.20×10^{-6} cm^2/s (reduced) and 6.66×10^{-6} cm^2/s (oxidized).⁴⁵

$$i_p = 2.69 \times 10^5 A D^{\frac{1}{2}} C \nu^{\frac{1}{2}} \quad \text{Equation 3.2}$$

The square root of the scan rates versus the peak currents were fit with a linear regression model (**Figure 3.8**), and the slope was used to solve for the electroactive area in **Equation 3.2**. Temperature was assumed to be 25°C. The electroactive areas for all TPE formulations are reported in **Table 3.3**.

Table 3.3: Calculated electroactive areas for all binder formulations for TC303 graphite and 3569 graphite.

	TC303			3569		
	PMMA	PS	PCL	PMMA	PS	PCL
Oxidized (cm²)	0.139	0.201	0.044	0.185	0.190	0.038
Reduced (cm²)	0.133	0.197	0.019	0.178	0.185	0.024

The oxidized and reduced electroactive areas seem to be in good agreement across all TPE formulations, with PCL having the greatest discrepancy, which is likely a result of redox species adsorbing to the surface and/or slow electron transfer kinetics. The geometric surface area of the working electrodes (WE) for all TPE formulations was 0.071 cm². For the TC303 graphite, the PMMA- and PS-TPEs electroactive area were 192% and 280% greater than the geometric surface area. For the 3569 graphite, the PMMA- and PS-TPEs electroactive area were 256% and 264% greater than the geometric surface area. These values seem plausible, based on the rough surfaces (increasing electroactive surface area) observed from the SEM analysis. The electroactive area calculations are also in good agreement with the current densities and electron transfer kinetics. For the PCL-TPEs, the electroactive surface area is smaller than the geometric surface area, which is further supported by the more resistive cyclic voltammograms in **Figure 3.7**.

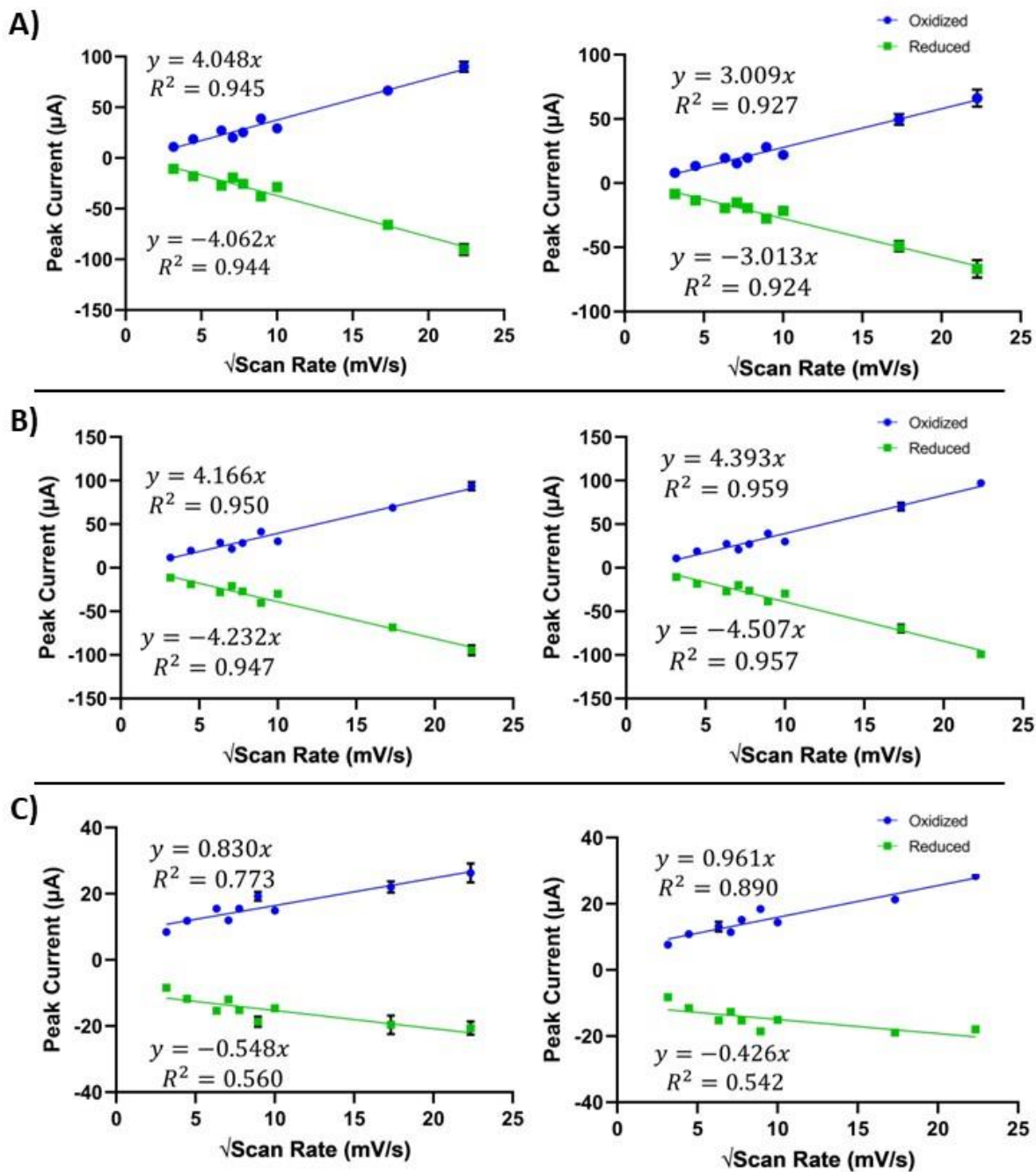


Figure 3.8. Plots of the peak current vs the square root of the scan rate for the oxidized and reduced peaks for **A)** PMMA-TPEs with 3569 (left) and TC303 (right), **B)** PS-TPEs with 3569 (left) and TC303 (right), and **C)** PCL-TPEs with 3569 (left) and TC303 (right).

3.4 Conclusions

Both the binder and graphite play crucial roles in the chemical and physical properties of thermoplastic electrodes. The inherent physical and chemical properties influence the utility of the electrode, in this case, for the analysis of Pb^{2+} . PS-based TPEs showed the best overall performance for both metal deposition and electrochemical characterization. However, the size of the graphite played a critical role, as PS-TC303 outperformed PS-3569. For the PS-TPEs, it is hypothesized that the aromatic group of polystyrene is responsible for creating edge planes during polishing. The orientation of the binder can create small perpendicular edge planes, allowing the material to be more densely packed which improves electron transfer kinetics while maintaining a relatively smooth surface. PCL is likely being degraded either during fabrication and/or through polishing. The hydrolysis of the binder could result in the formation of the other functional groups, mainly carbonyl groups, by reacting with the surrounding water and oxygen. Further, the long carbon chain of PCL is likely contributing to the flexibility of the binder, creating the tubular shapes observed in the SEM images. PMMA and PS are notably more brittle than PCL, likely creating more sheered edges within the graphite. PMMA has fewer surface oxides in comparison to PS, which is supported by the lower current density. Because of the carboxyl groups of the binder itself, hydrogen bonding can occur between the binder molecules, inhibiting graphite interaction with the binder, creating less densely packed conductive material. It is hypothesized that the material contains small islands of PMMA bound to itself, which could be confirmed with more extensive XPS mapping. Broadly, TPEs can be used for metal analysis, with the proper tuning of the electrode surface.

References

- (1) Uslu, B.; Ozkan, S. A. Electroanalytical Application of Carbon Based Electrodes to the Pharmaceuticals. *Anal. Lett.* **2007**, *40* (5), 817–853. <https://doi.org/10.1080/00032710701242121>.
- (2) Zhang, T.; Ran, F. Design Strategies of 3D Carbon-Based Electrodes for Charge/Ion Transport in Lithium Ion Battery and Sodium Ion Battery. *Adv. Funct. Mater.* **2021**, *31* (17), 2010041. <https://doi.org/10.1002/adfm.202010041>.
- (3) A. Wring, S.; P. Hart, J. Chemically Modified, Carbon-Based Electrodes and Their Application as Electrochemical Sensors for the Analysis of Biologically Important Compounds. A Review. *Analyst* **1992**, *117* (8), 1215–1229. <https://doi.org/10.1039/AN9921701215>.
- (4) Dubey, R.; Guruviah, V. Review of Carbon-Based Electrode Materials for Supercapacitor Energy Storage. *Ionics* **2019**, *25* (4), 1419–1445. <https://doi.org/10.1007/s11581-019-02874-0>.
- (5) Casanova, A.; Iniesta, J.; Gomis-Berenguer, A. Recent Progress in the Development of Porous Carbon-Based Electrodes for Sensing Applications. *Analyst* **2022**, *147* (5), 767–783. <https://doi.org/10.1039/D1AN01978C>.
- (6) Dekanski, A.; Stevanović, J.; Stevanović, R.; Nikolić, B. Ž.; Jovanović, V. M. Glassy Carbon Electrodes: I. Characterization and Electrochemical Activation. *Carbon* **2001**, *39* (8), 1195–1205. [https://doi.org/10.1016/S0008-6223\(00\)00228-1](https://doi.org/10.1016/S0008-6223(00)00228-1).
- (7) Van der Linden, W. E.; Dieker, J. W. Glassy Carbon as Electrode Material in Electro-Analytical Chemistry. *Anal. Chim. Acta* **1980**, *119* (1), 1–24. [https://doi.org/10.1016/S0003-2670\(00\)00025-8](https://doi.org/10.1016/S0003-2670(00)00025-8).
- (8) Kava, A. A.; Henry, C. S. Exploring Carbon Particle Type and Plasma Treatment to Improve Electrochemical Properties of Stencil-Printed Carbon Electrodes. *Talanta* **2021**, *221*, 121553. <https://doi.org/10.1016/j.talanta.2020.121553>.
- (9) A. Wring, S.; P. Hart, J. Chemically Modified, Screen-Printed Carbon Electrodes. *Analyst* **1992**, *117* (8), 1281–1286. <https://doi.org/10.1039/AN9921701281>.
- (10) Švancara, I.; Vytras, K.; Kalcher, K.; Walcarius, A.; Wang, J. Carbon Paste Electrodes in Facts, Numbers, and Notes: A Review on the Occasion of the 50-Years Jubilee of Carbon Paste in Electrochemistry and Electroanalysis. *Electroanalysis* **2009**, *21* (1), 7–28. <https://doi.org/10.1002/elan.200804340>.
- (11) Ramírez-García, S.; Alegret, S.; Céspedes, F.; J. Forster, R. Carbon Composite Electrodes: Surface and Electrochemical Properties. *Analyst* **2002**, *127* (11), 1512–1519. <https://doi.org/10.1039/B206201A>.
- (12) Tan, S.; Lazenby, R. A.; Bano, K.; Zhang, J.; Bond, A. M.; Macpherson, J. V.; Unwin, P. R. Comparison of Fast Electron Transfer Kinetics at Platinum, Gold, Glassy Carbon and Diamond Electrodes Using Fourier-Transformed AC Voltammetry and Scanning

Electrochemical Microscopy. *Phys. Chem. Chem. Phys.* **2017**, *19* (13), 8726–8734.
<https://doi.org/10.1039/C7CP00968B>.

(13) Klunder, K. J.; Nilsson, Z.; Sambur, J. B.; Henry, C. S. *Patternable Solvent-Processed Thermoplastic Graphite Electrodes*. ACS Publications. <https://doi.org/10.1021/jacs.7b06173>.

(14) Klunder, K. J.; Clark, K. M.; McCord, C.; Berg, K. E.; Minteer, S. D.; Henry, C. S. Polycaprolactone-Enabled Sealing and Carbon Composite Electrode Integration into Electrochemical Microfluidics. *Lab. Chip* **2019**, *19* (15), 2589–2597.
<https://doi.org/10.1039/C9LC00417C>.

(15) Noviana, E.; Klunder, K. J.; Channon, R. B.; Henry, C. S. Thermoplastic Electrode Arrays in Electrochemical Paper-Based Analytical Devices. *Anal. Chem.* **2019**, *91* (3), 2431–2438. <https://doi.org/10.1021/acs.analchem.8b05218>.

(16) Clark, K. M.; Henry, C. S. Thermoplastic Electrode (TPE)-Based Enzymatic Glucose Sensor Using Polycaprolactone-Graphite Composites. *Electroanalysis* **2022**, *34* (12), 1869–1876.
<https://doi.org/10.1002/elan.202100446>.

(17) McCord, C. P.; Summers, B.; Henry, C. S. Simultaneous Analysis of Ascorbic Acid, Uric Acid, and Dopamine at Bare Polystyrene Thermoplastic Electrodes. *ChemElectroChem* **2022**, *9* (11), e202101600. <https://doi.org/10.1002/celec.202101600>.

(18) McCord, C. P.; Summers, B.; Henry, C. S. Redox Behavior and Surface Morphology of Polystyrene Thermoplastic Electrodes. *Electrochimica Acta* **2021**, *393*, 139069.
<https://doi.org/10.1016/j.electacta.2021.139069>.

(19) Berg, K. E.; Leroux, Y. R.; Hapiot, P.; Henry, C. S. SECM Investigation of Carbon Composite Thermoplastic Electrodes. *Anal. Chem.* **2021**, *93* (3), 1304–1309.
<https://doi.org/10.1021/acs.analchem.0c01041>.

(20) Berg, K. E.; Leroux, Y. R.; Hapiot, P.; Henry, C. S. Increasing Applications of Graphite Thermoplastic Electrodes with Aryl Diazonium Grafting. *ChemElectroChem* **2019**, *6* (18), 4811–4816. <https://doi.org/10.1002/celec.201901048>.

(21) Pradela-Filho, L. A.; Araújo, D. A. G.; Takeuchi, R. M.; Santos, A. L.; Henry, C. S. Thermoplastic Electrodes as a New Electrochemical Platform Coupled to Microfluidic Devices for Tryptamine Determination. *Anal. Chim. Acta* **2021**, *1147*, 116–123.
<https://doi.org/10.1016/j.aca.2020.12.059>.

(22) Ozer, T.; Henry, C. S. All-Solid-State Potassium-Selective Sensor Based on Carbon Black Modified Thermoplastic Electrode. *Electrochimica Acta* **2022**, *404*, 139762.
<https://doi.org/10.1016/j.electacta.2021.139762>.

(23) Ozer, T.; Henry, C. S. Microfluidic-Based Ion-Selective Thermoplastic Electrode Array for Point-of-Care Detection of Potassium and Sodium Ions. *Microchim. Acta* **2022**, *189* (4), 152.
<https://doi.org/10.1007/s00604-022-05264-y>.

- (24) Ozer, T.; McCord, C.; Geiss, B. J.; Dandy, D.; Henry, C. S. Thermoplastic Electrodes for Detection of Escherichia Coli. *J. Electrochem. Soc.* **2021**, *168* (4), 047509. <https://doi.org/10.1149/1945-7111/abf77e>.
- (25) Barton, J.; García, M. B. G.; Santos, D. H.; Fanjul-Bolado, P.; Ribotti, A.; McCaul, M.; Diamond, D.; Magni, P. Screen-Printed Electrodes for Environmental Monitoring of Heavy Metal Ions: A Review. *Microchim. Acta* **2016**, *183* (2), 503–517. <https://doi.org/10.1007/s00604-015-1651-0>.
- (26) Wang, J.; Rivas, G.; Cai, X.; Palecek, E.; Nielsen, P.; Shiraishi, H.; Dontha, N.; Luo, D.; Parrado, C.; Chicharro, M.; Farias, P. A. M.; Valera, F. S.; Grant, D. H.; Ozsoz, M.; Flair, M. N. DNA Electrochemical Biosensors for Environmental Monitoring. A Review. *Anal. Chim. Acta* **1997**, *347* (1), 1–8. [https://doi.org/10.1016/S0003-2670\(96\)00598-3](https://doi.org/10.1016/S0003-2670(96)00598-3).
- (27) Shetti, N. P.; Malode, S. J.; Vernekar, P. R.; Nayak, D. S.; Shetty, N. S.; Reddy, K. R.; Shukla, S. S.; Aminabhavi, T. M. Electro-Sensing Base for Herbicide Aclonifen at Graphitic Carbon Nitride Modified Carbon Electrode – Water and Soil Sample Analysis. *Microchem. J.* **2019**, *149*, 103976. <https://doi.org/10.1016/j.microc.2019.103976>.
- (28) Hwang, J.-H.; Pathak, P.; Wang, X.; Rodriguez, K. L.; Park, J.; Cho, H. J.; Lee, W. H. A Novel Fe-Chitosan-Coated Carbon Electrode Sensor for in Situ As(III) Detection in Mining Wastewater and Soil Leachate. *Sens. Actuators B Chem.* **2019**, *294*, 89–97. <https://doi.org/10.1016/j.snb.2019.05.044>.
- (29) Manisankar, P.; Sundari, P. L. A.; Sasikumar, R.; Palaniappan, S. P. Electroanalysis of Some Common Pesticides Using Conducting Polymer/Multiwalled Carbon Nanotubes Modified Glassy Carbon Electrode. *Talanta* **2008**, *76* (5), 1022–1028. <https://doi.org/10.1016/j.talanta.2008.04.056>.
- (30) Ahmed, M.; Matsumoto, M.; Kurosawa, K. Heavy Metal Contamination of Irrigation Water, Soil, and Vegetables in a Multi-Industry District of Bangladesh. *Int. J. Environ. Res.* **2018**, *12* (4), 531–542. <https://doi.org/10.1007/s41742-018-0113-z>.
- (31) Bobaker, A. M.; Alakili, I.; Sarmani, S. B.; Al-Ansari, N.; Yaseen, Z. M. Determination and Assessment of the Toxic Heavy Metal Elements Abstracted from the Traditional Plant Cosmetics and Medical Remedies: Case Study of Libya. *Int. J. Environ. Res. Public Health* **2019**, *16* (11). <https://doi.org/10.3390/ijerph16111957>.
- (32) Fashola, M. O.; Ngole-Jeme, V. M.; Babalola, O. O. Heavy Metal Pollution from Gold Mines: Environmental Effects and Bacterial Strategies for Resistance. *Int. J. Environ. Res. Public Health* **2016**, *13* (11). <https://doi.org/10.3390/ijerph13111047>.
- (33) J. Borrill, A.; E. Reily, N.; V. Macpherson, J. Addressing the Practicalities of Anodic Stripping Voltammetry for Heavy Metal Detection: A Tutorial Review. *Analyst* **2019**, *144* (23), 6834–6849. <https://doi.org/10.1039/C9AN01437C>.

- (34) Kava, A. A.; Beardsley, C.; Hofstetter, J.; Henry, C. S. Disposable Glassy Carbon Stencil Printed Electrodes for Trace Detection of Cadmium and Lead. *Anal. Chim. Acta* **2020**, *1103*, 58–66. <https://doi.org/10.1016/j.aca.2019.12.047>.
- (35) Bansod, B.; Kumar, T.; Thakur, R.; Rana, S.; Singh, I. A Review on Various Electrochemical Techniques for Heavy Metal Ions Detection with Different Sensing Platforms. *Biosens. Bioelectron.* **2017**, *94*, 443–455. <https://doi.org/10.1016/j.bios.2017.03.031>.
- (36) Martín-Yerga, D.; Álvarez-Martos, I.; Blanco-López, M. C.; Henry, C. S.; Fernández-Abedul, M. T. Point-of-Need Simultaneous Electrochemical Detection of Lead and Cadmium Using Low-Cost Stencil-Printed Transparency Electrodes. *Anal. Chim. Acta* **2017**, *981*, 24–33. <https://doi.org/10.1016/j.aca.2017.05.027>.
- (37) Wang, L.; Zhang, H.; Cao, G.; Zhang, W.; Zhao, H.; Yang, Y. Effect of Activated Carbon Surface Functional Groups on Nano-Lead Electrodeposition and Hydrogen Evolution and Its Applications in Lead-Carbon Batteries. *Electrochimica Acta* **2015**, *186*, 654–663. <https://doi.org/10.1016/j.electacta.2015.11.007>.
- (38) Oliveira, L. S.; Alba, J. F. G.; Silva, V. L.; Ribeiro, R. T.; Falcão, E. H. L.; Navarro, M. The Effect of Surface Functional Groups on the Performance of Graphite Powders Used as Electrodes. *J. Electroanal. Chem.* **2018**, *818*, 106–113. <https://doi.org/10.1016/j.jelechem.2018.04.022>.
- (39) Eng, A. Y. S.; Chua, C. K.; Pumera, M. Refinements to the Structure of Graphite Oxide: Absolute Quantification of Functional Groups via Selective Labelling. *Nanoscale* **2015**, *7* (47), 20256–20266. <https://doi.org/10.1039/C5NR05891K>.
- (40) Kim, J.; Lee, N.; Min, Y. H.; Noh, S.; Kim, N.-K.; Jung, S.; Joo, M.; Yamada, Y. Distinguishing Zigzag and Armchair Edges on Graphene Nanoribbons by X-Ray Photoelectron and Raman Spectroscopies. *ACS Omega* **2018**, *3* (12), 17789–17796. <https://doi.org/10.1021/acsomega.8b02744>.
- (41) Ji, X.; Banks, C. E.; Crossley, A.; Compton, R. G. Oxygenated Edge Plane Sites Slow the Electron Transfer of the Ferro-/Ferricyanide Redox Couple at Graphite Electrodes. *ChemPhysChem* **2006**, *7* (6), 1337–1344. <https://doi.org/10.1002/cphc.200600098>.
- (42) Randviir, E. P. A Cross Examination of Electron Transfer Rate Constants for Carbon Screen-Printed Electrodes Using Electrochemical Impedance Spectroscopy and Cyclic Voltammetry. *Electrochimica Acta* **2018**, *286*, 179–186. <https://doi.org/10.1016/j.electacta.2018.08.021>.
- (43) McCreery, R. L. Advanced Carbon Electrode Materials for Molecular Electrochemistry. *Chem. Rev.* **2008**, *108* (7), 2646–2687. <https://doi.org/10.1021/cr068076m>.
- (44) Zhu, P.; Zhao, Y. Cyclic Voltammetry Measurements of Electroactive Surface Area of Porous Nickel: Peak Current and Peak Charge Methods and Diffusion Layer Effect. *Mater. Chem. Phys.* **2019**, *233*, 60–67. <https://doi.org/10.1016/j.matchemphys.2019.05.034>.

(45) Moldenhauer, J.; Meier, M.; Paul, D. W. Rapid and Direct Determination of Diffusion Coefficients Using Microelectrode Arrays. *J. Electrochem. Soc.* **2016**, *163* (8), H672. <https://doi.org/10.1149/2.0561608jes>.

CHAPTER 4: ELECTROCHEMICAL IMMUNOASSAY FOR THE DETECTION OF SARS-CoV-2 NUCLEOCAPSID PROTEIN IN NASOPHARYNGEAL SAMPLES

4.1 Chapter Overview.

The COVID-19 pandemic presented several diagnostic challenges. Up until recently, point-of-care diagnostics for SARS-CoV-2 were lacking. This work describes the development of a highly sensitive electrochemical immunoassay capable of quantitatively detecting the presence of SARS-CoV-2 virus in patient nasopharyngeal samples using screen-printed carbon electrodes (SPCEs) functionalized with capture antibodies targeting the SARS-CoV-2 nucleocapsid protein (N protein). For measurements, samples are added to the electrode surface, followed by horseradish peroxidase (HRP)-conjugated detection antibodies also targeting the SARS-CoV-2 N protein to form a sandwich immunoassay. The concentration of virus in samples is quantified using chronoamperometry in the presence of 3,3',5,5'-tetramethylbenzidine (TMB). Limits of detection equivalent to less than 50 plaque forming units/mL (PFU/mL) were determined with virus sample volumes of 20 μ L. No cross-reactivity was detected with influenza virus and other coronavirus N proteins. A preliminary patient study was conducted as a proof-of-concept clinical study and validated using RT-qPCR. This work was a multi-author project, with contributions from many. Isabelle Samper and I collected all the data presented here together and contributed equally to the data processing and writing of the manuscript. Kaylee Clark, Melissa Schenkel, Trey Pittman, and Wisarut Khamcharoen helped collect the preliminary data (not shown here) that the work is based off and what was further optimized. Samples were collected and analyzed by Loran Anderson and James Terry. The work from the chapter was published in *Analytical Chemistry* entitled “Electrochemical immunoassay for the detection of SARS-CoV-2 nucleocapsid protein in nasopharyngeal samples.”

4.2 Introduction.

Electrochemical sensors have received attention in recent years as a means of detecting biological analytes such as viruses and other disease-related pathogens, including HIV, zika virus, and hepatitis B.¹⁻⁵ Detection mechanisms for the aforementioned pathogens have been integrated into point-of-care (POC) sensors, which can be deployable in low-resource settings, where standard instrumentation is not available. However, POC sensors can lack sensitivity and are usually only qualitative, as many of them use optical or colorimetric detection.^{6,7} The incorporation of an electrochemical detection mechanism can improve sensitivity and provide quantitative measurements.

POC electrochemical biosensors have several advantages, including rapid response times, low limits of detection, and low sample volume requirements, while being cost effective.⁸ The most common examples are handheld glucometers, used by diabetic patients for routinely measuring their blood glucose levels.⁹ In order to make electrochemical platforms suitable for POC applications, stencil-printed or screen-printed carbon electrodes (SPCEs) are often used, as they are robust, mass producible and disposable.¹⁰⁻¹²

Coronavirus disease 2019, known as COVID-19, is caused by severe acute respiratory syndrome coronavirus 2 (SARS-CoV-2), and has impacted world health since late 2019. As of September, 2021 the virus has infected 222M people and resulted in 4.5M deaths worldwide.¹³ Prompt and accurate testing for SARS-CoV-2 and its mutations is essential for continual management and remediation of the virus. Currently, the gold standard viral test is real time quantitative polymerase chain reaction (RT-qPCR), which is a molecular approach that amplifies the genetic material of the virus.^{14,15} However, RT-qPCR can take several days to output results, and therefore, efforts have been made to build POC testing technologies to detect COVID-19

infections.^{16,17} SARS-CoV-2 infection can also be detected with immunoassays, using antibodies to bind viral antigens with high specificity.¹⁸ Enzyme-linked immunosorbent assays (ELISAs) are considered the standard for antigen testing; however, they are laboratory-based due to the need for external instrumentation to interpret the results.^{19–21}

Monitoring of antibody and antigen levels plays a key role in assessing patient prognosis and managing the pandemic progression.^{22,23} According to the Center of Disease Control (CDC), viral tests, including antigen tests are valuable POC diagnostic tools to detect active infection and inform medical care.²⁴ Since the start of the pandemic, several antigen-based POC tests have been developed, with varying degrees of sensitivity, specificity and accuracy. Two well-known and commercially available examples include the BinaxNOW test developed by Abbot and the IntelliSwab test developed by OraSure.^{25,26} Several other POC tests have been developed, but their low sensitivities resulted in high rates of false negatives.²⁷

To improve upon the current state of POC diagnostics for COVID-19, the sensitivity and accuracy of the test is of utmost importance. The incorporation of an electrochemical detection mechanism can provide an avenue to create a more robust, sensitive, and accurate POC diagnostic.^{28,29} However, the development of POC technologies is not linear, and requires several stages of development, including but not limited to the miniaturization of the sensing mechanism and the integration of reagent delivery, while also considering the means of sample collection, preparation, and addition to the diagnostic test to provide ease of use for the end user.¹⁷ The work described herein focuses on the fundamental development of the sensing mechanism, including the ability to miniaturize the platform without compromising the immunoassay integrity. The goal of the proposed assay is to perform as well as a standard ELISA but doing so outside of typical lab settings and without the long wait times and reagent high volumes.

Here, a novel electrochemical sandwich immunoassay using SPCEs to quantify SARS-CoV-2 nucleocapsid protein (N protein) in nasopharyngeal samples is presented. N-protein was chosen for this assay because of its clinical relevance in COVID-19 diagnostics.^{30,31} SPCEs are functionalized with capture antibodies, which specifically bind to N proteins present in the sample tested. Detection antibodies conjugated to horseradish peroxidase (HRP) and the substrate, 3,3',5,5'-tetramethylbenzidine (TMB), are then added after the sample. Chronoamperometry is performed to measure the levels of HRP, which correlates to the N-protein concentration in the sample. Optimization of the immunoassay antibody pair is shown and the sensor response to samples of varying virus concentrations is characterized. Additionally, cross-reactivity to variants and potential interferents is studied. Further, a preliminary clinical study using twenty-two patient nasopharyngeal swab samples is conducted. Unlike other POC diagnostics, the method described here is quantitative, due to the use of an electrochemical measurement. This work is aimed at being the first step in developing a POC sensor for the rapid, sensitive, and accurate detection of active SARS-CoV-2 infection.

4.3 Methods and Materials.

Reagents.

Buffers. 10 mM phosphate buffer solution (PBS) with 140 mM sodium chloride and 2.7 mM potassium chloride, pH 7.4 was prepared using a tablet according to package instructions (Research Products International, USA). 10 mM phosphate buffer solution with Tween20 (PBST) was made by adding Tween20 to PBS to a final concentration of 0.05%. Hanks Balanced Salt Solution (HBSS) was prepared by combining 0.14 M sodium chloride, 5 mM potassium chloride, 1 mM calcium chloride, 0.4 mM magnesium sulfate, 0.5 mM magnesium chloride, 0.3 mM sodium phosphate, 0.4 mM potassium phosphate, and 4 mM sodium carbonate to make a 1 L solution in

Millipore water. HBSST buffer was made by adding Tween80 (Fischer Scientific, USA) and Igepal (MP Biomedicals, USA) to HBSS to make a final concentration of 0.1% and 0.1%, respectively. Viral transport media (VTM) was prepared according to CDC guidelines by adding fetal bovine serum, gentamicin sulfate, and amphotericin B to HBSS to a final concentration of 2%, 50 mg/mL and 250 µg/mL, respectively.³² VTMT was made by adding Tween80 and Igepal to VTM so that the final concentration of each surfactant was equal to 0.1%.

House-made anti-N antibodies. Rabbit polyclonal antibodies targeting SARS-CoV-2 N protein were prepared as previously described.^{33,34} Briefly, rabbits were immunized by Pacific Immunology with truncated SARS-CoV-2 nucleocapsid antigen (AA133-416) produced and purified in *E. coli*. Hyperimmune serum was passed over a SARS-CoV-2 nucleocapsid column and binding antibodies eluted and collected. Eluted antibody preparations were dialyzed against PBS with 0.1% sodium azide and stored at -20°C until use.

House-made anti-N-HRP. Anti-N antibodies prepared as described above were first purified using a NucAway spin column (Invitrogen by Thermo Fisher Scientific, USA) according to package instructions. Once purified, antibodies were conjugated to horseradish peroxidase (HRP) using a Lightning-Link® HRP-Conjugation kit (Abcam, UK) according to kit instructions. Stock antibody was diluted to 0.5 µg/mL in HBSST.

Aged casein solution. Solution was prepared as previously reported.³⁵ Briefly, a 100 mL solution was prepared by dissolving 6 g of casein in 80 mL of 50 mM sodium hydroxide overnight. Then 0.26 g boric acid and 0.45 g sodium tetraborate were added and the solution was pH adjusted to 8.5. The solution was brought to volume with Millipore distilled water and heated at 37°C for 7 days. Aliquots of 50 µL were stored at -20°C until needed, then thawed and combined with 950 µL of 50 mM borate buffer, pH 8.5 and mixed well.

Commercial antibodies and substrate. SARS-CoV-2 anti-N antibodies and SARS-CoV-2 detection-HRP antibodies (Table S1) were purchased from Sino Biological. Anti-N antibodies were diluted from the stock to 10 $\mu\text{g}/\text{mL}$ in PBS and detection-HRP antibody was diluted from the stock to 0.5 $\mu\text{g}/\text{mL}$ in HBSST. Substrate 3,3',5,5'-tetramethylbenzidine (TMB) was purchased from Sigma Aldrich, USA.

Inactivated SARS-CoV-2 virus samples. SARS-CoV-2 virus (USA-WA1, NR52281) was provided by BEI resources. Virus was passaged at biosafety level 3 (BSL-3) containment in Vero E6 cells (ATCC (CRL-1586) in 2% FBS-DMEM at 37°C to generate virus stocks. Virus stocks were stored at -80°C . Viral stocks were quantified for infectivity by plaque assay (plaque forming units (PFU)/ml) and total genome copy number by real time digital droplet polymerase chain reaction (RT-ddPCR), using the procedures established by Case et al.³⁶ To inactivate virus, viral stocks were brought to 0.1% final concentration of Triton-X-100 on ice for 30 minutes. All inactivated stocks were tested for active virus using cytopathic effect assays of 5 days and were considered inactive if no cell killing was observed compared to live virus controls. All inactivated virus samples were handled following BSL2 safety practices. For the antibody screening study (**Figure 4.1**), virus samples were diluted in HBSST. For all other experiments, dilutions of the virus stock solution to the desired viral concentrations were made in VTMT.

Clinical samples

Nasopharyngeal swabs were collected from asymptomatic staff at long-term care facilities and characterized as described here.³⁷ Briefly, viral RNA was extracted and quantified using qPCR with CDC primer-probes. Infectious virus was measuring using a standard plaque assay on Vero cells starting with 250 μL of input material. Clinical samples were surfactant-inactivated, which breaks up viral particles and releases N proteins in solution. Samples were diluted by a 1.07 factor

in VTM, Tween80 and Igepal so that the final concentrations of Tween80 and Igepal in each sample were both equal to 0.1%. A 20 μL volume of each surfactant-containing clinical sample was tested on our immunoassay.

Electrode fabrication.

Electrodes were fabricated as previously reported.³⁸ Briefly, TC303 synthetic graphite (Asbury Carbons, USA) and carbon ink (Ercon, USA) were mixed in a 3:5 ratio respectively to create a homogeneous paste. The paste was stencil-printed and dried at 60°C for 30 min. Ag|AgCl ink (Sigma Aldrich, USA) was then painted onto the reference electrode and dried at 60°C for 30 min. Double sided adhesive wells (3M, USA) were laser cut (8 mm in diameter) and adhered to the electrode surface, exposing the reference, counter, and working electrode (9 mm²).

Electrochemical immunoassay protocol.

The immunoassay and electrochemical detection mechanism are illustrated in **Figure 4.1** and the protocol is as follows.

SPCE functionalization. SPCEs were functionalized (see Figure S1 by covalently binding capture anti-N antibodies to the electrode surface via carbodiimide coupling using N-ethyl-N'-(3-(dimethylamino)propyl)carbodiimide/N-hydroxysuccinimide (EDC/NHS) chemistry. First, 20 μL of a solution of 5 mM EDC (Sigma Aldrich, USA), 5 mM NHS (Sigma Aldrich, USA) in water was pipetted on the working electrode and incubated in a humid chamber for 45 min. Then, this solution was pipetted off and 20 μL of 10 $\mu\text{g}/\text{mL}$ capture anti-N antibody in PBS was immediately added to the electrode surface. Following a 1 h incubation period in a humid chamber, the electrode was washed with PBST followed by PBS using solid stream spray bottles. The SPCE was then incubated with 50 μL of aged casein solution for 1 h to block non-specific activated binding sites,

and subsequently rinsed with PBST followed by PBS using transfer pipettes. The total duration for SPCE functionalization was 2 h and 45 min.

SPCE testing. Functionalized SPCEs were tested by pipetting 20 μL of a sample solution onto the electrode surface. Following a 40 min incubation period, the electrodes were washed with PBST followed by PBS using solid stream spray bottles. Subsequently, 20 μL of a 0.5 $\mu\text{g}/\text{mL}$ anti-N-HRP detection antibody solution prepared in HBSST was pipetted onto the electrode surface and incubated for 25 min. Following washing with PBST and PBS using solid stream spray bottles, 50 μL of TMB was added to the electrode surface and incubated for 2 min. Immediately following the TMB incubation, a chronoamperometry recording was started. Using a portable potentiostat (PalmSens4), a 0.0 V potential was applied to the working electrode (vs the Ag|AgCl reference electrode) for 2 min, while the current was recorded between the working and the counter electrodes. The total duration for SPCE testing was 70 min.

Data analysis.

Chronoamperometry traces were averaged on a 10 s interval (100 points) centered in 100 S following the start of the recording ($I_{100\text{s}}$). The 100 s timepoint was chosen to avoid the initial charging current and to evaluate the plateau current. Blank samples ($n=3$), made with the same media as the samples tested but without virus, were run in parallel to virus samples to get a measure of the background current. For every sample tested, the mean background current was subtracted from the sample current and the immunoassay current ΔI generated by each sample was defined as follows, as illustrated in **Figure 4.1**.

$$\Delta I = -\left(I_{100s}^{sample} - \text{mean}(I_{100s}^{blank})\right)$$

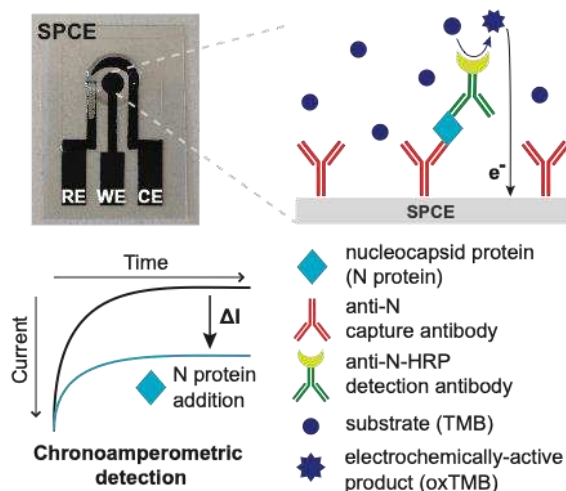


Figure 4.1. Electrochemical detection mechanism of SARS-CoV-2 nucleocapsid (N) protein on a modified screen-printed carbon electrode (SPCE), with RE, WE and CE representing reference, working, and counter electrodes, respectively. If present in the sample, N proteins are captured by anti-N antibodies (capture antibodies) immobilized on the SPCE surface. HRP-labelled anti-N antibodies (detection antibodies) subsequently bind to N proteins and catalyze the oxidation of the substrate TMB, creating an electroactive compound (oxTMB) that is detected via chronoamperometry.

4.4 Results and Discussion.

Antibody screening.

Since the beginning of the pandemic, many antibodies have become available for SARS-CoV-2 detection, necessitating screening to optimize performance. To screen capture anti-N and detection anti-N-HRP antibodies, the electrochemical immunoassay was tested on the SPCEs using eight different antibody pairs (**Table 4.1**). The antibodies tested were selected based on a previous study³⁹ that identified commercially available antibodies that performed best on immunoassays targeting SARS-CoV-2 N protein, as well as following commercial supplier recommendations.⁴⁰ All antibody pairs from commercial sources (Pairs 2 to 8) were tested against inhouse-generated antibodies (Pair 1).

Table 4.1: Capture/detection anti-N antibody pairs tested. Except for Pair 1, all antibodies were purchased from SinoBiological. Antibody mixes were made by mixing different antibodies in equal proportions. Mix 1: MM08, MM05, R004. Mix 1-H: MM08-H, MM05-H, R004-H. Mix 2: MM08, MM05, R004, R040, R001. Mix 2-H: MM08-H, MM05-H, R004-H, R040-H, R001-H. Antibody names refer to last four digits of SinoBiological catalog numbers (preceded by 40143-). -H indicates an HRP label.

Pairs	1	2	3	4	5	6	7	8
Capture Antibodies	Polyclonal anti-N	R004	MM05	MM08	MM08	R005	Mix 1	Mix 2
Detection Antibodies	Polyclonal anti-N	R040-H	R001-H	R004-H	MM05-H	MM05-H	Mix 1-H	Mix 2-H

Figure 4.2 shows the immunoassay current output, ΔI , to a virus concentration of 5,000 PFU/mL, generated using each of the eight antibody pairs. The results show that ΔI is highly variable across the eight antibody pairs tested, which is consistent with results from previous studies.^{39,41} The difference in signal observed across antibody pairs can be attributed to multiple factors, including the binding affinity between the antibodies and our target and the way the antibodies bind to the electrode surface. On the electrochemical immunoassay, Pair 5 gave a current output 34% higher than that generated by the affinity-purified rabbit anti-N polyclonal antibodies (Pair 1) and critically, demonstrated the most consistent current output, as shown by the lowest standard deviation. Therefore, Pair 5 was identified as the antibody pair that performed best on the electrochemical immunoassay. From this point onwards, all experiments were conducted with antibody Pair 5.

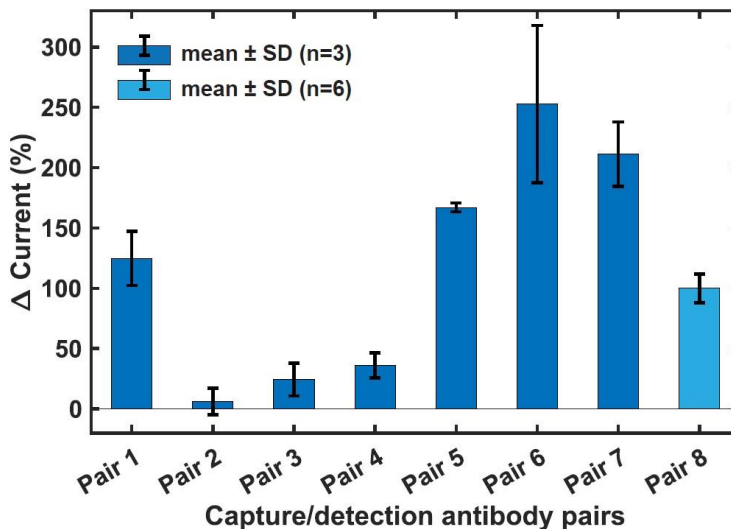


Figure 4.2. Comparison of capture/detection antibody pairs. Blank-subtracted current generated by SARS-CoV-2 samples at 5,000 PFU/mL (2.4×10^8 RNA copies/mL), using different pairs of capture/detection antibodies. Antibody pairs are defined in **Table 4.1**. Dataset was collected in two separate experiments and measurements from Pair 8 were repeated across both experiments. For each pair, current is expressed as a percentage of the current generated using Pair 8 from the corresponding experiment. Except for Pair 8 where the current mean and standard deviation (SD) are calculated over both experiments ($n=6$), data represent mean and SD of triplicate measurements ($n=3$). SD of Pair 8 for each experiment ($n=3$) remains higher than SD of Pair 5 ($\pm 11\%$ and $\pm 12\%$ vs $\pm 4\%$).

Electrochemical response to different concentrations of SARS-CoV-2 virus

The ability of the immunoassay to quantify the concentration of SARS-CoV-2 virus in 20 μL VTM-based samples was evaluated by exposing functionalized SPCEs to different inactivated SARS-CoV-2 virus concentrations. Chronoamperograms recorded from SPCEs exposed to eight different SARS-CoV-2 virus concentrations ranging from 0 to 110,000 PFU/mL are shown in **Figure 4.3A**. Each concentration was tested on three separate SPCEs ($n=3$) and the average and standard deviation of the triplicate measurements are shown by line and shaded areas, respectively. The calibration curve generated by this dataset is shown in **Figure 4.3B**. The graphs show clear separation between current responses to each concentration tested and an increase in ΔI with increasing virus concentration. The current-to-concentration response curve follows a 4-parameter logistic (4PL) model, which is typical for immunoassays.^{42,43} Note that the current response to the

highest virus concentration tested, 110,000 PFU/mL, is lower than that of the lower 22,000 PFU/mL concentration. This could be attributed to the hook effect, which has been previously reported in immunoassays⁴⁴ when an overload of virus prevents antibody binding and decreases signal. Patient samples likely won't contain such high viral loads, but if a sample contained a viral load within the range impacted by the hook effect, the assay would still exhibit a positive result, and the accuracy of the test would not be compromised. These results demonstrate the ability of the immunoassay to quantify SARS-CoV-2 virus concentration in VTM samples of volumes as low as 20 μ L. The limit of detection (LOD) of our electrochemical assay, calculated as the viral concentration corresponding to 3X the standard deviation of the signal recorded in the absence of virus, was found to be equivalent to 45 PFU/mL. This calculated LOD is lower than the measured LOD of most commercially available rapid antigen tests, which are typically between 80 and 500 PFU/mL.^{27,45} However, it is important to note that the lowest concentration tested as part of this experiment was 220 PFU/mL (**Figure 4.3**), which is above the calculated 45 PFU/mL LOD, whereas the LODs of the commercial tests reported in these studies^{27,45} were measured concentrations. Nevertheless, the concentration of 220 PFU/mL that is clearly detected by the assay is well within the range of these reported LODs.

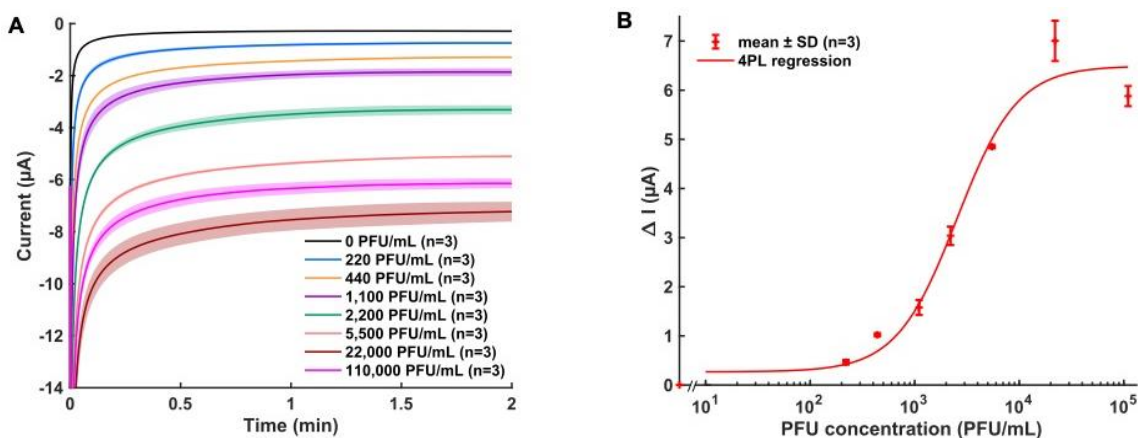


Figure 4.3. Electrochemical detection of SARS-CoV-2 virus in 20 µL samples. (A) Chronoamperograms obtained from SPCEs exposed to different concentrations of SARS-CoV-2 virus. Lines and shaded areas represent mean and SD of triplicate measurements. (B) Corresponding calibration curve showing ΔI averaged over a 10 s interval centered in $t = 100$ s. Data fitted with a 4-parameter logistic (4PL) regression. LOD, calculated as the virus concentration corresponding to 3 SD of the blank signal, is equivalent to 45 PFU/mL ($\gg 2.17 \times 10^6$ viral RNA copies/mL, as calculated from genome concentration of the virus stock solution which was measured via RT-digital droplet(dd)PCR).

Cross-reactivity to SARS-CoV-2 variants and potential interferents

The ability to differentiate the target from other viruses while detecting SARS-CoV-2 variants is essential for test accuracy. Cross-reactivity studies using SARS-CoV-2 variant viruses and potential interferents were carried out to investigate the specificity of the biosensor toward SARS-CoV-2. Using the same experimental conditions as for SARS-CoV-2 detection (**Figure 4.3**), the following four SARS-CoV-2 variants were tested: Alpha (UK-00), Alpha (UK-11), Beta (SA-08) and Beta (SA-09) against the original SARS-CoV-2 strain on the functionalized SPCEs, as shown in **Figure 4.4A**. All virus strains were tested at the same concentration of 1,100 PFU/mL and interestingly, all variant strains generated a higher signal than the original strain. This can be explained by higher viral RNA content of the variant strains, as later revealed by RT-ddPCR assays (not shown). Importantly, all four variants tested could be detected by the functionalized SPCEs indicating the applicability of the system as new variants emerge.

The functionalized SPCEs were then evaluated against 10 potential interferents, including influenza virus, Sindbis virus and N proteins from eight other coronaviruses as compared to the response generated by SARS-CoV-2 virus. To simulate a worst-case scenario, potential interfering viruses and N proteins were tested at concentrations as high as 10,000 PFU/mL and 100 ng/mL, respectively, while SARS-CoV-2 virus was tested at a clinically relevant concentration of 1,100 PFU/mL.⁴⁶ Results from this interferent study are presented in **Figure 4.4B** and show that none of the 10 potential interferents tested was detected by the functionalized SPCEs. Instead, each of them generated a small negative ΔI , which means that their current response was closer to zero than that of the blank samples (VTM only). This is likely due to proteins being present in such high concentrations in the potential interferent samples, which could block access of the detection antibodies to the electrode surface, decreasing the electron turnover by TMB. These results demonstrate the specificity of our assay toward SARS-CoV-2 virus.

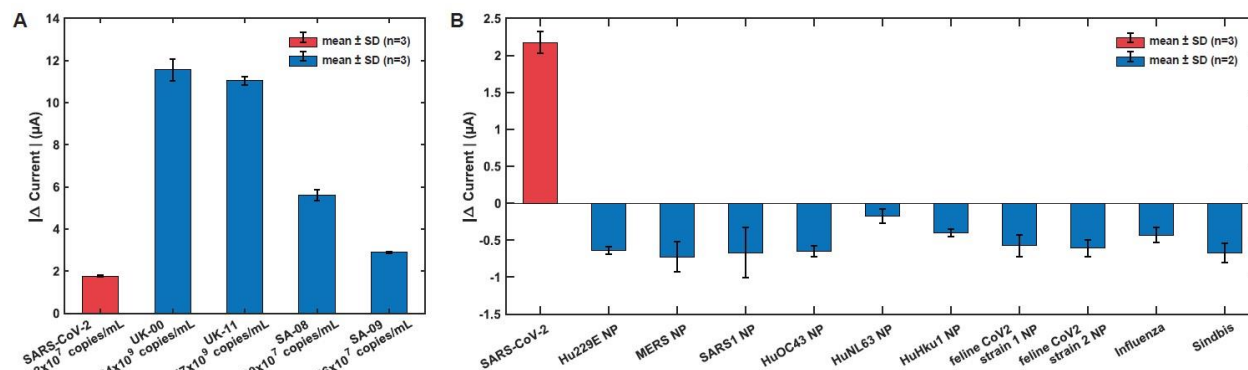


Figure 4.4. Cross-reactivity to SARS-CoV-2 variants and potential interferents in 20 μL VTM samples. (A) ΔI generated by virus samples of SARS-CoV-2 original strain and SARS-CoV-2 variant strains. All samples were tested at 1,100 PFU/mL as determined by a plaque assay, and corresponding viral RNA concentrations were 5.2×10^7 , 2.0×10^9 , 1.5×10^9 , 1.8×10^7 and 1.7×10^7 copies/mL for SARS-CoV-2 original, Alpha (UK-00), Alpha (UK-11), Beta (SA-08) and Beta (SA-09) strains, respectively. Data represents mean and SD of $n=3$. (B) ΔI generated by virus samples of SARS-CoV-2 original strain as well as samples of potential interfering viruses and recombinant N proteins from potential interfering viruses. SARS-CoV-2 original virus strain samples were tested at 1,100 PFU/mL (5.2×10^7 RNA copies/mL), N protein samples were tested at 100 ng/mL and heterologous virus samples (influenza and Sindbis) were tested at 10,000 PFU/mL. Data represents mean and SD of $n=3$ for SARS-CoV-2 virus and duplicate measurements for potential interferents.

Proof-of-concept clinical sample study

To evaluate the diagnostic potential of the functionalized SPCEs on clinical samples, a proof-of-concept assay was carried out where twenty-two 20 μ L heat-inactivated de-identified nasopharyngeal samples were tested. All samples had been previously banked as part of a long-term care facility study. All samples were tested with RT-qPCR and identified as either viral RNA negative or positive, according to their N1 cycle threshold (Ct) value (≤ 38 or >38 , respectively). **Table 4.2** compares the results of this electrochemical assay to the RT-qPCR assay and shows specificity and sensitivity values, respectively calculated as the number of samples identified as negatives by the electrochemical assay divided by the number of samples identified as negative by the RT-qPCR assay, and the number of samples identified as positive by the electrochemical assay divided by the number of samples identified as positive by the RT-qPCR assay. The electrochemical assay was found to be 100% specific, with a total of 9 negative samples tested but only 54% sensitive when considering all 13 positive samples. However, the sensitivity of the assay increased with decreasing Ct values and reached 70% and 100% for samples with Ct values <30 and <25 , respectively. This suggests that the LOD of the assay is around a Ct value of 25, which is defined as acceptable for a POC test by the World Health Organization.⁴⁷ Since previous studies demonstrated that infectivity was significantly reduced when RT-qPCR Ct values were higher than 24,^{48,49} these results suggest that our electrochemical assay has potential to be used as a method to identify SARS-CoV-2 infectious patients.

Table 4.2. Clinical nasopharyngeal samples

ELECTROCHEMICAL ASSAY OUTCOME	RT-QPCR ASSAY OUTCOME			
	Positive, N1 Ct			Negative
	<25	<30	≤38	N1 Ct>38
POSITIVE	5	7	7	0
NEGATIVE	0	3	6	9
	Sensitivity			Specificity
	100%	70%	54%	100%

For samples in which the presence of SARS-CoV-2 virus was detected by the electrochemical assay, the equivalent PFU concentration was quantified by simultaneously testing samples of known PFU concentration on our assay, as shown in **Figure 4.5A**. It is important to note that there could be discrepancies between the estimated equivalent PFU concentration and the N protein concentration in these samples, justifying the use of the term “equivalent”. **Figure 4.5B** shows the equivalent PFU concentration of all seven samples that were identified as positive by our electrochemical assay, plotted against their N1 Ct value, as determined by the RT-qPCR assay.

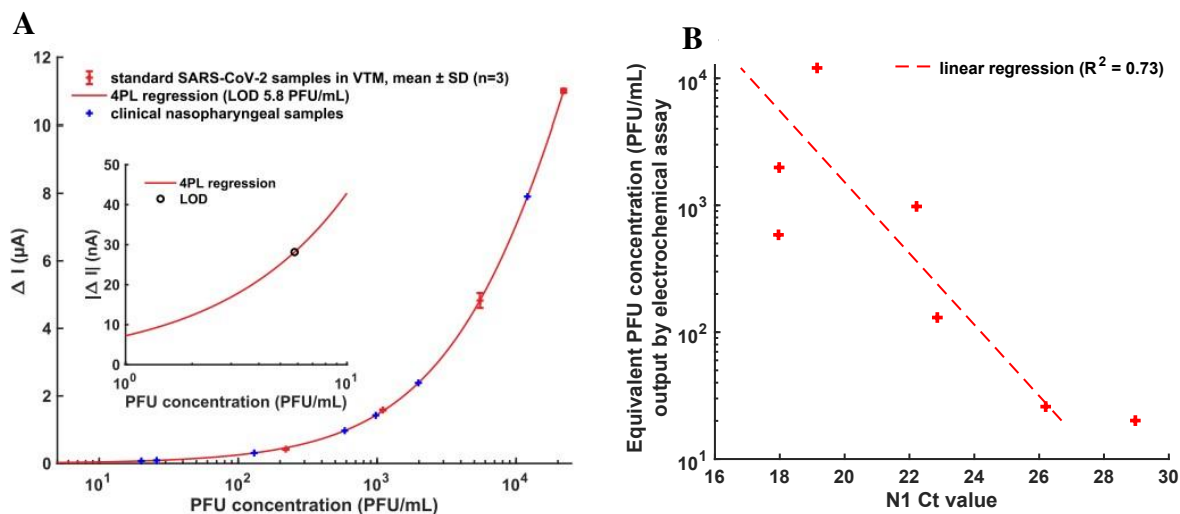


Figure 4.5. A) Calibration curve obtained from running standard samples of SARS-CoV-2 in VTM (PFU concentration determined by plaque assays) in parallel to running clinical nasopharyngeal samples. Calibration data was fitted with a 4PL regression and the LOD was calculated using 3 SD of the blank signal. Insert shows the calibration curve at low PFU concentrations with the calculated LOD. B) Samples plotted against corresponding RT-qPCR N1 Ct values. Data from the 7 out of 10 samples tested with a N1 Ct value in the range (16-30) that were identified as positive by the electrochemical assay. Linear regression suggests a correlation between our assay output and standard RT-qPCR Ct value ($R^2=0.73$).

Figure 4.5B shows a possible linear correlation between both variables, with a coefficient of determination of 0.73. The differences can be attributed to the two assays measuring different aspects of the virus biochemistry (antigen content vs viral RNA). Since lower Ct values have been associated with higher chance of infectivity,^{49,50} these results suggest that the output of our electrochemical assay could serve as a measure of patient infectivity. To test this hypothesis, plaque assays were performed on positive samples and the actual PFU concentrations were compared to the PFU concentration equivalents output by the electrochemical assay.

Figure 4.6 compares the results of the electrochemical assay to those of plaque assays and shows a linear correlation between the equivalent and the actual PFU concentrations obtained by the two methods, with a coefficient of determination of 0.9993. Note that one datapoint (circled, **Figure 4.6**) was excluded from the regression as it was identified as an outlier. The causes for this

datapoint to be an outlier are unknown and the sample could not be tested again due to limited available volume. It is possible that despite its high infectivity, this sample contained a lower amount of N proteins, which are the targeted molecules of the electrochemical assay. However, this sample was identified as infectious or positive by both methods. The infectious samples with the two lowest actual PFU concentrations (measured by plaque assay) had RT-qPCR N1 Ct values between 22 and 23 and no PFU was detected in samples with N1 Ct values higher than 23. However, according to the electrochemical assay, two positive samples with N1 Ct values of 26 and 29 were found to have equivalent PFU concentrations of 20 and 25 PFU/mL, respectively. This shows that the electrochemical immunoassay was able to detect apparent SARS-CoV-2 virus in samples that the infectivity measure missed. Whilst a larger clinical study must be performed for this assay to be used as a diagnostic tool, these results indicate that the quantitative electrochemical assay may have potential to assess patient infectivity status.

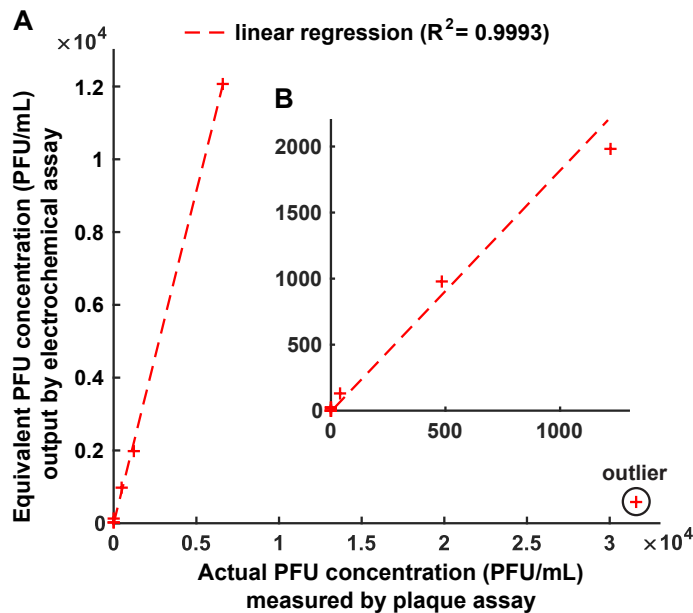


Figure 4.6. Correlation between SARS-CoV-2 actual PFU concentration of RT-qPCR positive clinical nasopharyngeal samples obtained using a standard plaque assay and equivalent PFU concentration of the same samples obtained using the electrochemical assay. The linear regression shown ($R^2=0.9993$) excludes the data point labelled as outlier. (A) shows the entire dataset and (B) zooms in on lower PFU concentrations ranging from 0 to 1300 PFU/mL.

4.5 Conclusions.

Here, a novel electrochemical biosensor for the detection of SARS-CoV-2 N-protein for practical applications in POC testing of COVID-19 has been described. The successful functionalization of SPCEs using optimized antibody pairs, while reducing reagent use and time in comparison to traditional approaches such as ELISA and RT-qPCR was demonstrated. Further, the assay can be fabricated at low cost (<\$1) and would be easily scaled up for future manufacturing. The assay has been validated against inactivated SARS-CoV-2 virus samples, showing that the virus concentration can be quantified with a LOD that is lower than most rapid antigen tests currently on the market, and that satisfies the WHO requirements for POC tests. A proof-of-concept clinical study was conducted on a small dataset of 22 clinical samples, in which results from the assay developed herein were compared to both RT-qPCR and plaque assays. Despite these three assays measuring three different variables (antigen, genome copies and infectivity), results from this proof-of-concept study show possible agreement between the developed assay and both RT-qPCR and plaque assays, indicating that the assay may have potential to predict infectivity of patients with COVID-19. A larger scale clinical study would need to be conducted to confirm these preliminary findings. Current limitations of the assay include the manual pipetting steps needed to functionalize the electrodes and the time from sample to result. Although assay time was greatly reduced compared to traditional lab-based methods such as ELISA, RT-qPCR and plaque assays, time from sample to result remains approximately 70 min. Future work is aimed at automating the assay by integrating it in a fluidic platform amenable to the point of care,⁵¹ further reducing the assay time, and assessing the stability of the functionalized SPCEs over extended time periods under various storage conditions. This will enable the assay to be

integrated into a robust, quantitative, and sensitive POC test for the detection of SARS-CoV-2 infection in patients.

REFERENCES

- (1) de Eguilaz, M. R.; Cumba, L. R.; Forster, R. J. Electrochemical Detection of Viruses and Antibodies: A Mini Review. *Electrochem. Commun.* **2020**, *116*, 106762. <https://doi.org/10.1016/j.elecom.2020.106762>.
- (2) Kaushik, A.; Yndart, A.; Kumar, S.; Jayant, R. D.; Vashist, A.; Brown, A. N.; Li, C.-Z.; Nair, M. A Sensitive Electrochemical Immunosensor for Label-Free Detection of Zika-Virus Protein. *Sci. Rep.* **2018**, *8* (1), 9700. <https://doi.org/10.1038/s41598-018-28035-3>.
- (3) Li, X.; Scida, K.; Crooks, R. M. Detection of Hepatitis B Virus DNA with a Paper Electrochemical Sensor. *Anal. Chem.* **2015**, *87* (17), 9009–9015. <https://doi.org/10.1021/acs.analchem.5b02210>.
- (4) Zhou, L.; Huang, J.; Yu, B.; Liu, Y.; You, T. A Novel Electrochemiluminescence Immunosensor for the Analysis of HIV-1 P24 Antigen Based on P-RGO@Au@Ru-SiO₂ Composite. *ACS Appl. Mater. Interfaces* **2015**, *7* (44), 24438–24445. <https://doi.org/10.1021/acsami.5b08154>.
- (5) Shrivastav, A. M.; Cvelbar, U.; Abdulhalim, I. A Comprehensive Review on Plasmonic-Based Biosensors Used in Viral Diagnostics. *Commun. Biol.* **2021**, *4* (1), 1–12. <https://doi.org/10.1038/s42003-020-01615-8>.
- (6) St John, A.; Price, C. P. Existing and Emerging Technologies for Point-of-Care Testing. *Clin. Biochem. Rev.* **2014**, *35* (3), 155–167.
- (7) Mejía-Salazar, J. R.; Rodrigues Cruz, K.; Materón Vásques, E. M.; Novais de Oliveira Jr., O. Microfluidic Point-of-Care Devices: New Trends and Future Prospects for EHealth Diagnostics. *Sensors* **2020**, *20* (7), 1951. <https://doi.org/10.3390/s20071951>.
- (8) Menon, S.; Mathew, M. R.; Sam, S.; Keerthi, K.; Kumar, K. G. Recent Advances and Challenges in Electrochemical Biosensors for Emerging and Re-Emerging Infectious Diseases. *J. Electroanal. Chem.* **2020**, *878*, 114596. <https://doi.org/10.1016/j.jelechem.2020.114596>.
- (9) Electrochemical Glucose Biosensors | Chemical Reviews <https://pubs-acsc-org.ezproxy2.library.colostate.edu/doi/full/10.1021/cr068123a> (accessed 2021 -10 -06).
- (10) Godino, N.; Gorkin, R.; Bourke, K.; Ducleé, J. Fabricating Electrodes for Amperometric Detection in Hybrid Paper/ Polymer Lab-on-a-Chip Devices. *Lab. Chip* **2012**, *12* (18), 3281–3284. <https://doi.org/10.1039/C2LC40223H>.
- (11) P. Metters, J.; K. Kampouris, D.; E. Banks, C. Electrochemistry Provides a Point-of-Care Approach for the Marker Indicative of Pseudomonas Aeruginosa Infection of Cystic Fibrosis Patients. *Analyst* **2014**, *139* (16), 3999–4004. <https://doi.org/10.1039/C4AN00675E>.
- (12) Yáñez-Sedeño, P.; Campuzano, S.; Pingarrón, J. M. Screen-Printed Electrodes: Promising Paper and Wearable Transducers for (Bio)Sensing. *Biosensors* **2020**, *10* (7), 76. <https://doi.org/10.3390/bios10070076>.
- (13) WHO Coronavirus (COVID-19) Dashboard <https://covid19.who.int> (accessed 2021 -09 -09).
- (14) Loeffelholz, M. J.; Tang, Y.-W. Laboratory Diagnosis of Emerging Human Coronavirus Infections – the State of the Art. *Emerg. Microbes Infect.* **2020**, *9* (1), 747–756. <https://doi.org/10.1080/22221751.2020.1745095>.
- (15) Vandenberg, O.; Martiny, D.; Rochas, O.; van Belkum, A.; Kozlakidis, Z. Considerations for Diagnostic COVID-19 Tests. *Nat. Rev. Microbiol.* **2021**, *19* (3), 171–183. <https://doi.org/10.1038/s41579-020-00461-z>.

- (16) Valera, E.; Jankelow, A.; Lim, J.; Kindratenko, V.; Ganguli, A.; White, K.; Kumar, J.; Bashir, R. COVID-19 Point-of-Care Diagnostics: Present and Future. *ACS Nano* **2021**, *15* (5), 7899–7906. <https://doi.org/10.1021/acsnano.1c02981>.
- (17) Choi, J. R. Development of Point-of-Care Biosensors for COVID-19. *Front. Chem.* **2020**, *8*, 517. <https://doi.org/10.3389/fchem.2020.00517>.
- (18) Souf, S. Recent Advances in Diagnostic Testing for Viral Infections. *Biosci. Horiz. Int. J. Stud. Res.* **2016**, *9* (hzw010). <https://doi.org/10.1093/biohorizons/hzw010>.
- (19) Voller, A.; Bartlett, A.; Bidwell, D. E.; Clark, M. F.; Adams, A. N. Y. 1976. The Detection of Viruses by Enzyme-Linked Immunosorbent Assay (ELISA). *J. Gen. Virol.* *33* (1), 165–167. <https://doi.org/10.1099/0022-1317-33-1-165>.
- (20) Yolken, R. H. Enzyme-Linked Immunosorbent Assay (ELISA): A Practical Tool for Rapid Diagnosis of Viruses and Other Infectious Agents. *Yale J. Biol. Med.* **1980**, *53* (1), 85–92.
- (21) Boonham, N.; Kreuze, J.; Winter, S.; van der Vlugt, R.; Bergervoet, J.; Tomlinson, J.; Mumford, R. Methods in Virus Diagnostics: From ELISA to next Generation Sequencing. *Virus Res.* **2014**, *186*, 20–31. <https://doi.org/10.1016/j.virusres.2013.12.007>.
- (22) Scourfield, D. O.; Reed, S. G.; Quastel, M.; Alderson, J.; Bart, V. M. T.; Teijeira Crespo, A.; Jones, R.; Pring, E.; Richter, F. C.; The Oxford-Cardiff COVID-19 Literature Consortium; Burnell, S. E. A. The Role and Uses of Antibodies in COVID-19 Infections: A Living Review. *Oxf. Open Immunol.* **2021**, *2* (1). <https://doi.org/10.1093/oxfimm/iqab003>.
- (23) Peeling, R. W.; Wedderburn, C. J.; Garcia, P. J.; Boeras, D.; Fongwen, N.; Nkengasong, J.; Sall, A.; Tanuri, A.; Heymann, D. L. Serology Testing in the COVID-19 Pandemic Response. *Lancet Infect. Dis.* **2020**, *20* (9), e245–e249. [https://doi.org/10.1016/S1473-3099\(20\)30517-X](https://doi.org/10.1016/S1473-3099(20)30517-X).
- (24) CDC. Healthcare Workers <https://www.cdc.gov/coronavirus/2019-ncov/hcp/testing-overview.html> (accessed 2021 -09 -09).
- (25) BinaxNOW <http://binaxnow.workplace.abbott/binaxnow-3> (accessed 2021 -10 -07).
- (26) InteliSwab™ - COVID Rapid Test. Results in hand, in minutes. <https://inteliswab.com/> (accessed 2021 -10 -07).
- (27) Cubas-Atienzar, A. I.; Kontogianni, K.; Edwards, T.; Wooding, D.; Buist, K.; Thompson, C. R.; Williams, C. T.; Patterson, E. I.; Hughes, G. L.; Baldwin, L.; Escadafal, C.; Sacks, J. A.; Adams, E. R. Limit of Detection in Different Matrices of 19 Commercially Available Rapid Antigen Tests for the Detection of SARS-CoV-2. *Sci. Rep.* **2021**, *11* (1), 18313. <https://doi.org/10.1038/s41598-021-97489-9>.
- (28) Campuzano, S.; Pedrero, M.; Yáñez-Sedeño, P.; Pingarrón, J. M. New Challenges in Point of Care Electrochemical Detection of Clinical Biomarkers. *Sens. Actuators B Chem.* **2021**, *345*, 130349. <https://doi.org/10.1016/j.snb.2021.130349>.
- (29) Pashchenko, O.; Shelby, T.; Banerjee, T.; Santra, S. A Comparison of Optical, Electrochemical, Magnetic, and Colorimetric Point-of-Care Biosensors for Infectious Disease Diagnosis. *ACS Infect. Dis.* **2018**, *4* (8), 1162–1178. <https://doi.org/10.1021/acsinfectdis.8b00023>.
- (30) Li, T.; Wang, L.; Wang, H.; Li, X.; Zhang, S.; Xu, Y.; Wei, W. Serum SARS-COV-2 Nucleocapsid Protein: A Sensitivity and Specificity Early Diagnostic Marker for SARS-COV-2 Infection. *Front. Cell. Infect. Microbiol.* **2020**, *10*, 470. <https://doi.org/10.3389/fcimb.2020.00470>.
- (31) Shan, D.; Johnson, J. M.; Fernandes, S. C.; Suib, H.; Hwang, S.; Wuelfing, D.; Mendes, M.; Holdridge, M.; Burke, E. M.; Beauregard, K.; Zhang, Y.; Cleary, M.; Xu, S.; Yao, X.; Patel, P. P.; Plavina, T.; Wilson, D. H.; Chang, L.; Kaiser, K. M.; Nattermann, J.; Schmidt, S. V.; Latz, E.; Hrusovsky, K.; Mattoon, D.; Ball, A. J. N-Protein Presents Early in Blood, Dried Blood and

- Saliva during Asymptomatic and Symptomatic SARS-CoV-2 Infection. *Nat. Commun.* **2021**, *12* (1), 1931. <https://doi.org/10.1038/s41467-021-22072-9>.
- (32) CDC Posts New Standard Operating Procedure for Creating Viral Transport Media https://www.cdc.gov/csels/dls/locs/2020/new_sop_for_creating_vtm.html (accessed 2021 -11 -02).
- (33) Fagre, A.; Lewis, J.; Eckley, M.; Zhan, S.; Rocha, S. M.; Sexton, N. R.; Burke, B.; Geiss, B.; Peersen, O.; Bass, T.; Kading, R.; Rovnak, J.; Ebel, G. D.; Tjalkens, R. B.; Aboellail, T.; Schountz, T. SARS-CoV-2 Infection, Neuropathogenesis and Transmission among Deer Mice: Implications for Spillback to New World Rodents. *PLoS Pathog.* **2021**, *17* (5), e1009585. <https://doi.org/10.1371/journal.ppat.1009585>.
- (34) Terry, J. S.; Anderson, L. B.; Scherman, M. S.; McAlister, C. E.; Perera, R.; Schountz, T.; Geiss, B. J. Development of a SARS-CoV-2 Nucleocapsid Specific Monoclonal Antibody. *Virology* **2021**, *558*, 28–37. <https://doi.org/10.1016/j.virol.2021.01.003>.
- (35) Grant, B. D.; Anderson, C. E.; Williford, J. R.; Alonzo, L. F.; Glukhova, V. A.; Boyle, D. S.; Weigl, B. H.; Nichols, K. P. SARS-CoV-2 Coronavirus Nucleocapsid Antigen-Detecting Half-Strip Lateral Flow Assay Toward the Development of Point of Care Tests Using Commercially Available Reagents. *Anal. Chem.* **2020**, *92* (16), 11305–11309. <https://doi.org/10.1021/acs.analchem.0c01975>.
- (36) Case, J. B.; Bailey, A. L.; Kim, A. S.; Chen, R. E.; Diamond, M. S. Growth, Detection, Quantification, and Inactivation of SARS-CoV-2. *Virology* **2020**, *548*, 39–48. <https://doi.org/10.1016/j.virol.2020.05.015>.
- (37) Gallichotte, E. N.; Quicke, K. M.; Sexton, N. R.; Fitzmeyer, E.; Young, M. C.; Janich, A. J.; Dobos, K.; Pabilonia, K. L.; Gahm, G.; Carlton, E. J.; Ebel, G. D.; Ehrhart, N. Early Adoption of Longitudinal Surveillance for SARS-CoV-2 among Staff in Long-Term Care Facilities: Prevalence, Virologic and Sequence Analysis. *Microbiol. Spectr.* *0* (0), e01003-21. <https://doi.org/10.1128/Spectrum.01003-21>.
- (38) Kava, A. A.; Beardsley, C.; Hofstetter, J.; Henry, C. S. Disposable Glassy Carbon Stencil Printed Electrodes for Trace Detection of Cadmium and Lead. *Anal. Chim. Acta* **2020**, *1103*, 58–66. <https://doi.org/10.1016/j.aca.2019.12.047>.
- (39) Cate, D. M.; Bishop, J. D.; Hsieh, H. V.; Glukhova, V. A.; Alonzo, L. F.; Hermansky, H. G.; Barrios-Lopez, B.; Grant, B. D.; Anderson, C. E.; Spencer, E.; Kuhn, S.; Gallagher, R.; Rivera, R.; Bennett, C.; Byrnes, S. A.; Connelly, J. T.; Dewan, P. K.; Boyle, D. S.; Weigl, B. H.; Nichols, K. P. Antibody Screening Results for Anti-Nucleocapsid Antibodies Toward the Development of a Lateral Flow Assay to Detect SARS-CoV-2 Nucleocapsid Protein. *ACS Omega* **2021**, *6* (39), 25116–25123. <https://doi.org/10.1021/acsomega.1c01253>.
- (40) A Complete Toolkit to Develop a Diagnostic SARS-CoV-2 Antigen Test <https://www.sinobiological.com/research/virus/immunodiagnostic-sars-cov-2-antigen-test> (accessed 2021 -10 -11).
- (41) *Lateral Flow Immunoassay*; Wong, R., Tse, H., Eds.; Humana Press: Totowa, NJ, 2009. <https://doi.org/10.1007/978-1-59745-240-3>.
- (42) O'Connell, M.A; Belanger, B.A.; Haaland, P.D. Calibration and Assay Development Using the Four-Parameter Logistic Model - ScienceDirect. *Chemom. Intell. Lab. Syst.* **1993**, No. 20, 97–114.
- (43) Heineman, W. R.; Halsall, H. B. Strategies for Electrochemical Immunoassay. *Anal. Chem.* **1985**, *57* (12), 1321A-1331A. <https://doi.org/10.1021/ac00289a804>.

- (44) Tate, J.; Ward, G. Interferences in Immunoassay. *Clin. Biochem. Rev.* **2004**, *25* (2), 105–120.
- (45) Corman, V. M.; Haage, V. C.; Bleicker, T.; Schmidt, M. L.; Mühlemann, B.; Zuchowski, M.; Jo, W. K.; Tscheak, P.; Möncke-Buchner, E.; Müller, M. A.; Krumbholz, A.; Drexler, J. F.; Drosten, C. Comparison of Seven Commercial SARS-CoV-2 Rapid Point-of-Care Antigen Tests: A Single-Centre Laboratory Evaluation Study. *Lancet Microbe* **2021**, *2* (7), e311–e319. [https://doi.org/10.1016/S2666-5247\(21\)00056-2](https://doi.org/10.1016/S2666-5247(21)00056-2).
- (46) Lin, Y.-C.; Malott, R. J.; Ward, L.; Kiplagat, L.; Pabbaraju, K.; Gill, K.; Berenger, B. M.; Hu, J.; Fonseca, K.; Noyce, R.; Louie, T.; Evans, D. H.; Conly, J. M. *Detection and Quantification of Infectious Severe Acute Respiratory Coronavirus-2 in Diverse Clinical and Environmental Samples from Infected Patients: Evidence to Support Respiratory Droplet, and Direct and Indirect Contact as Significant Modes of Transmission*; 2021; p 2021.07.08.21259744. <https://doi.org/10.1101/2021.07.08.21259744>.
- (47) World Health Organization. Target Product Profiles for Priority Diagnostics to Support Response to the COVID-19 Pandemic v.1.0. World Health Organization September 28, 2020.
- (48) Rao, S. N.; Manissero, D.; Steele, V. R.; Pareja, J. A Narrative Systematic Review of the Clinical Utility of Cycle Threshold Values in the Context of COVID-19. *Infect. Dis. Ther.* **2020**, *9* (3), 573–586. <https://doi.org/10.1007/s40121-020-00324-3>.
- (49) Bullard, J.; Dust, K.; Funk, D.; Strong, J. E.; Alexander, D.; Garnett, L.; Boodman, C.; Bello, A.; Hedley, A.; Schiffman, Z.; Doan, K.; Bastien, N.; Li, Y.; Van Caesele, P. G.; Poliquin, G. Predicting Infectious SARS-CoV-2 from Diagnostic Samples. *Clin. Infect. Dis. Off. Publ. Infect. Dis. Soc. Am.* **2020**, ciaa638. <https://doi.org/10.1093/cid/ciaa638>.
- (50) Laferl, H.; Kelani, H.; Seitz, T.; Holzer, B.; Zimpernik, I.; Steinrigl, A.; Schmoll, F.; Wenisch, C.; Allerberger, F. An Approach to Lifting Self-Isolation for Health Care Workers with Prolonged Shedding of SARS-CoV-2 RNA. *Infection* **2021**, *49* (1), 95–101. <https://doi.org/10.1007/s15010-020-01530-4>.
- (51) Samper, I. C.; Sánchez-Cano, A.; Khamcharoen, W.; Jang, I.; Siangproh, W.; Baldrich, E.; Geiss, B. J.; Dandy, D. S.; Henry, C. S. Electrochemical Capillary-Flow Immunoassay for Detecting Anti-SARS-CoV-2 Nucleocapsid Protein Antibodies at the Point of Care. *ACS Sens.* **2021**. <https://doi.org/10.1021/acssensors.1c01527>.

CHAPTER 5: CONCLUSIONS

The ability to screen for heavy metal contamination is necessary, especially with the ever-increasing anthropogenic demand on Earth's core resources. Heavy metal contamination in food, water, and consumer products is a result of their use in mining, industrial, agricultural, medical, and technological applications.^{1,2} Lead (Pb) is among the most common heavy metals that cause adverse health effects, and therefore proper testing and remediation is critical.³ However, many of the gold-standard approaches for Pb testing relies on expensive instrumentation, hazardous reagents, and trained personnel, limiting the scope of testing location and availability.⁴⁻⁷ Electrochemical sensors have shown promise in filling this gap, making Pb detection more widely available, as they can be fast, reliable, user-friendly and portable.⁸⁻¹⁰ Several electrochemical sensors have been able to reach acceptable sensitivities, fulfilling the detection guidelines set by the World Health Organization. Carbon composite electrodes have been fundamental players in electrochemical analysis of heavy metals, as they are non-toxic versions of the previous mercury drop electrodes.^{11,12} Using a bismuth thin-film, carbon-based electrodes are able to perform equally, if not better to their Hg counterparts. However, extensive surface modification techniques are often required, to combat carbon composite electrodes slow electron transfer kinetics and poor electrochemical properties in relation to the precious metal electrodes.¹³⁻¹⁵ Further, issues of sample preparation for analysis are still of concern, as electrochemical methods can only measure labile metal ions, rather than total metal ion concentration. Heavy metals are often present in complex matrices, often requiring concentrated acids and high temperatures to completely destroy the matrix, freeing the metal ions. This dissertation seeks to address those needs, by exploring alternative sample preparation methods for heavy metal analysis in complex samples and offering a better understanding of carbon composite electrodes for their use as environmental sensors.

Chapter 2 introduces a need to detect heavy metals in cosmetics and presents a new approach for the analysis of cosmetics using stencil-printed carbon electrodes (SPCE). Heavy metal detection in cosmetics is a relatively new field,¹⁶⁻¹⁸ and to the best of my knowledge, no one has explored making analysis more user-friendly or available outside of traditional laboratory settings. Cosmetics present a unique challenge for analysis, as their matrices are complex and full of metal derivatives. Sample extraction is often difficult, and typically uses acid-based digestion methods. However, in low-resource regions such as Nepal and Africa, access to the necessary equipment and reagents is challenging, despite the need for analysis being critical. ICP-OES analysis of 24 cosmetic samples from these regions demonstrate that there is a growing need for regular and proper screening of the cosmetics samples, to prevent adverse health effects. The work in Chapter 2 outlines a potential extraction cocktail and procedure to address this need but requires more research and optimization before it can be applied to real samples. Despite this, the development of a cosmetic standard and initial extraction statistics show the potential utility of the approach.

Future work for this project should focus on improving the extraction cocktail and method. For simple matrices, this current method is suitable, but analysis of real samples proved that metal lability is a significant limiting factor in the application of the method. It is likely that metal lability will never be able to be fully achieved (i.e. 100%), but adjustment to the cocktail could enable higher extraction efficiencies and more reproducible results. A chelate-assistant approach could prove beneficial, promoting the chelation of Pb from the cosmetic to the chelation agent. The incorporation of EDTA as a potential chelation-assistant is a promising candidate,¹⁹ as EDTA has strong binding affinities with Pb, and its function is dependent on pH. Therefore, the additional of EDTA to the extraction cocktail could remove more Pb from the sample and the adjustment in pH

post extraction could release Pb back into solution for electrochemical analysis. Further, the length of extraction and solution conditions of citric acid should be explored in more depth. Due to the constraints of the project timeline, extensive exploration of the extraction parameters was limited. This was further compounded by the success of the proposed extraction cocktail on the developed cosmetic standard. Both the pH and solution concentrations were adapted from relevant soil literature, but adjustment of both parameters could increase Pb extraction. Other studies found in the literature suggest that slightly higher pH's are more conducive for Pb extraction,²⁰ in relation to a pH of 2.0. This is supported by the strongest Pb complex with citric acid being when it is missing one hydrogen and has a net negative charge of 1⁻.²⁰

Further, other work could focus on combining the electrochemistry with the extraction and take advantage of electrokinetics for metal extraction. One study found that by combining activated carbon and citric acid to an electrokinetic approach increased Pb removal from the sample.²¹ The application of the electric field and the citric acid work together to break matrix bonds and concentrate heavy metal ions at the electrode surface, removing them from the sample matrix. Due to SPCEs being thinner composite electrode, they may be unsuited for this approach, but the incorporation of TPEs, which are more robust than SPCE could be a viable option. In summary, the work presented in Chapter 2 sets a framework and demonstrates that an alternative extraction approach for heavy metals in complex sample matrices such as cosmetics is attainable. Future work should be focused on improving the cocktail and extraction conditions to produce more reproducible and higher yields.

Keeping with the theme of heavy metals, Chapter 3 explored the utility of thermoplastic electrodes for the Pb detection. Preliminary results demonstrate the TPEs could be used for metal detection, but further understanding of the chemical and physical properties of the electrode

surface was critical. Results indicated that the physical properties as well as the surface functional groups both contribute to the ability of Pb to successfully deposit on the surface. Different plastics and graphites were tested, to understand how the graphite and polymer interactions impact the unique characteristics. Polystyrene (PS) TPEs showed the best results, which is likely a result of the polymer positioning. However, the graphite played an important role on the utility of the PS as binder, with the smaller graphite formulation having better electrochemical properties. This suggests that the smaller particles are able to more densely back around the binder, creating a more conductive material. Further, PS-TPEs had the fewest amount of carbonyl surface functional groups, which have been shown to hinder metal deposition due to creating a more alkaline surface.²² Polymethyl methacrylate (PMMA) TPEs had inferior performance in relation to PS, but superior performance over the polycaprolactone (PCL) TPEs. The physical surface of the PMMA-TPEs was rougher while also containing high levels of carbonyl functional groups. Both graphites performed similarly, indicating that the polymer has the greatest impact on the electrode performance. This is hypothesized to be a result of hydrogen bonding interactions that can occur between the polymer itself. PCL-TPEs were the worst formulation and were unable to detect Pb within relevant ranges (10 ppb or less).

Future work should focus on further characterizing the PMMA- and PS-TPEs and their applications in environmental sensing. In adjusting the pre-treatment of the electrode, the physical and chemical properties can be tuned. Moreover, decreasing the limit of detection (LOD) for heavy metal analysis on both TPE formulations would expand their application in heavy metal remediation. The EPA and WHO set 10 ppb as the maximum Pb content in drinking water sources but require sensors to be able to detect below that level for maximum confidence. Increasing the acidic nature of the electrode surface through plasma treatment could enhance Pb adsorption to the

surface, increasing the sensitivity and lowering the LOD. Furthermore, increasing the mass transport of the metal ions across the surface through incorporation into the fluidic platform could achieve the same results. More broadly, generating a multiplexed sensor for multiple heavy metals would expand the practicality and novelty. Multiplexed electrochemical sensors for heavy metals can be limited to due to the electrochemical behavior of the individual metal ions. The ease of fabrication and pattern-ability of the TPEs could help alleviate some of these issues by incorporating multiple working electrodes while maintaining a single electrochemical cell. The tunability of the electrode surfaces could also be exploited to better encapsulate hard/soft acid base metal interactions to make each working electrode more selective for different metal ions.

More broadly, TPEs themselves could be expanded into other fields, such as batteries or energy storage. Various characterization efforts have shown that TPEs, depending on the polymer binder, have excellent capacitance and conductivity parameters, particularly the PMMA- and PS-formulations.^{23,24} With work in Chapter 3 demonstrating that metal electrodeposition chemistry can be successfully applied to TPEs, they could potentially be used for carbon-based electrode materials for metal-ion batteries with further optimization.²⁵ Additionally, the pattern-ability and ease of fabrication of the TPEs into complex 3D architectures could make them suitable candidates for the 3D battery manifolds that have become popular for smaller battery systems.^{26,27}

An electrochemical biosensor was also explored in Chapter 4, to address the need of point-of-care (POC) testing during the COVID-19 pandemic. Due to the unprecedented times, the application of my research was shifted, but carbon composite electrodes remained a vital part of the project. Carbon-based electrochemical biosensors were highly studied for POC testing of SARS-CoV-2 because of their speed, reliability, miniaturization, and low limits of detection.^{28,29} ELISAs (enzyme-linked immunosorbent assay) are one of the more common immunoassays used

for the detection of infectious diseases,^{30,31} and implementation onto an electrode substrate provided a quantitative, sensitive, and specific avenue for the detection of SARS-CoV-2. The developed assay reduces the time of a traditional ELISA assay and sets the framework for the incorporation of the modified electrode system into a POC device. The LOD and ability to detect patient samples with potential information on infectivity level decreases concern related to false positives/negatives often associated with POC devices.

Future work will focus on expanding the assay and multiplexing it with other viral targets, such as Flu and RSV. Changes to electrode design could easily incorporate multiple working electrodes and utilizing selective bioreceptors for each target would prevent cross-interference. Further, to make the assay more sensitive and stable overtime, nucleic acid bioreceptors instead of antibodies could be explored. Antibodies have been extensively used for biosensors but suffer from stability limitations and batch to batch variations. Nucleic acid receptors, such as aptamers, do not suffer from the same limitations as antibodies and can be specifically engineered for a target analyte.^{32,33} While not being a fully automated system, steps to incorporate the assay into a microfluidic platform will enable the assay to serve at the point-of-care. NFC potentiostats that can work with any smartphone have becoming increasingly popular with electrochemical point-of-need sensors.^{34,35} The incorporation of such a technology could bridge the gap between academic and industrial diagnostics, allowing for easier and more reliable diagnostics.

In summary, this dissertation presents work that expands the utility of carbon composite electrodes for environmental and biological applications. The methodologies and characterization move towards being able to monitor heavy metals in different matrices without the need for expensive instrumentation and hazardous reagents. The platforms explored in this work could be adapted to a variety of different applications beyond electrochemical sensors. Moreover, the

fundamental knowledge gained gives better understanding in the utility of carbon composite electrodes. The work reported moves closer to being able to deploy point-of-need electrochemical sensors for environmental and biological screening without compromising sensitivity and accuracy.

REFERENCES

- (1) Tchounwou, P. B.; Yedjou, C. G.; Patlolla, A. K.; Sutton, D. J. Heavy Metals Toxicity and the Environment. *EXS* **2012**, *101*, 133–164. https://doi.org/10.1007/978-3-7643-8340-4_6.
- (2) Järup, L. Hazards of Heavy Metal Contamination. *Br. Med. Bull.* **2003**, *68* (1), 167–182. <https://doi.org/10.1093/bmb/ldg032>.
- (3) Balali-Mood, M.; Naseri, K.; Tahergorabi, Z.; Khazdair, M. R.; Sadeghi, M. Toxic Mechanisms of Five Heavy Metals: Mercury, Lead, Chromium, Cadmium, and Arsenic. *Front. Pharmacol.* **2021**, *12*.
- (4) Hassan, N. M.; Rasmussen, P. E.; Dabek-Zlotorzynska, E.; Celso, V.; Chen, H. Analysis of Environmental Samples Using Microwave-Assisted Acid Digestion and Inductively Coupled Plasma Mass Spectrometry: Maximizing Total Element Recoveries. *Water. Air. Soil Pollut.* **2007**, *178* (1), 323–334. <https://doi.org/10.1007/s11270-006-9201-3>.
- (5) Sastre, J.; Sahuquillo, A.; Vidal, M.; Rauret, G. Determination of Cd, Cu, Pb and Zn in Environmental Samples: Microwave-Assisted Total Digestion versus Aqua Regia and Nitric Acid Extraction. *Anal. Chim. Acta* **2002**, *462* (1), 59–72. [https://doi.org/10.1016/S0003-2670\(02\)00307-0](https://doi.org/10.1016/S0003-2670(02)00307-0).
- (6) Domínguez-González, R.; Moreda-Piñeiro, A.; Bermejo-Barrera, A.; Bermejo-Barrera, P. Application of Ultrasound-Assisted Acid Leaching Procedures for Major and Trace Elements Determination in Edible Seaweed by Inductively Coupled Plasma-Optical Emission Spectrometry. *Talanta* **2005**, *66* (4), 937–942. <https://doi.org/10.1016/j.talanta.2004.12.051>.
- (7) Kazi, T. G.; Jamali, M. K.; Arain, M. B.; Afridi, H. I.; Jalbani, N.; Sarfraz, R. A.; Ansari, R. Evaluation of an Ultrasonic Acid Digestion Procedure for Total Heavy Metals Determination in Environmental and Biological Samples. *J. Hazard. Mater.* **2009**, *161* (2), 1391–1398. <https://doi.org/10.1016/j.jhazmat.2008.04.103>.
- (8) Martín-Yerga, D.; Álvarez-Martos, I.; Blanco-López, M. C.; Henry, C. S.; Fernández-Abedul, M. T. Point-of-Need Simultaneous Electrochemical Detection of Lead and Cadmium Using Low-Cost Stencil-Printed Transparency Electrodes. *Anal. Chim. Acta* **2017**, *981*, 24–33. <https://doi.org/10.1016/j.aca.2017.05.027>.
- (9) Kava, A. A.; Beardsley, C.; Hofstetter, J.; Henry, C. S. Disposable Glassy Carbon Stencil Printed Electrodes for Trace Detection of Cadmium and Lead. *Anal. Chim. Acta* **2020**, *1103*, 58–66. <https://doi.org/10.1016/j.aca.2019.12.047>.
- (10) Rosolina, S. M.; Chambers, J. Q.; Lee, C. W.; Xue, Z.-L. Direct Determination of Cadmium and Lead in Pharmaceutical Ingredients Using Anodic Stripping Voltammetry in Aqueous and DMSO/Water Solutions. *Anal. Chim. Acta* **2015**, *893*, 25–33. <https://doi.org/10.1016/j.aca.2015.07.010>.
- (11) Ariño, C.; Serrano, N.; Díaz-Cruz, J. M.; Esteban, M. Voltammetric Determination of Metal Ions beyond Mercury Electrodes. A Review. *Anal. Chim. Acta* **2017**, *990*, 11–53. <https://doi.org/10.1016/j.aca.2017.07.069>.
- (12) Wygant, B. R.; Lambert, T. N. Thin Film Electrodes for Anodic Stripping Voltammetry: A Mini-Review. *Front. Chem.* **2022**, *9*, 809535. <https://doi.org/10.3389/fchem.2021.809535>.

- (13) Corb, I.; Manea, F.; Radovan, C.; Pop, A.; Burtica, G.; Malchev, P.; Picken, S.; Schoonman, J. Carbon-Based Composite Electrodes: Preparation, Characterization and Application in Electroanalysis. *Sensors* **2007**, *7* (11), 2626–2635.
- (14) Manea, F.; Radovan, C.; Pop, A.; Corb, I.; Burtica, G.; Malchev, P.; Picken, S.; Schoonman, J. Carbon Composite Electrodes Applied for Electrochemical Sensors. In *Sensors for Environment, Health and Security*; Baraton, M.-I., Ed.; NATO Science for Peace and Security Series C: Environmental Security; Springer Netherlands: Dordrecht, 2009; pp 179–189. https://doi.org/10.1007/978-1-4020-9009-7_11.
- (15) Ramírez-García, S.; Alegret, S.; Céspedes, F.; J. Forster, R. Carbon Composite Electrodes: Surface and Electrochemical Properties. *Analyst* **2002**, *127* (11), 1512–1519. <https://doi.org/10.1039/B206201A>.
- (16) Alam, M. F.; Akhter, M.; Mazumder, B.; Ferdous, A.; Hossain, M. D.; Dafader, N. C.; Ahmed, F. T.; Kundu, S. K.; Taheri, T.; Atique Ullah, A. K. M. Assessment of Some Heavy Metals in Selected Cosmetics Commonly Used in Bangladesh and Human Health Risk. *J. Anal. Sci. Technol.* **2019**, *10* (1), 2. <https://doi.org/10.1186/s40543-018-0162-0>.
- (17) Borowska, S.; Brzóska, M. M. Metals in Cosmetics: Implications for Human Health. *J. Appl. Toxicol.* **2015**, *35* (6), 551–572. <https://doi.org/10.1002/jat.3129>.
- (18) Brzóska, M. M.; Galażyn-Sidorczuk, M.; Borowska, S. Metals in Cosmetics. In *Metal Allergy: From Dermatitis to Implant and Device Failure*; Chen, J. K., Thyssen, J. P., Eds.; Springer International Publishing: Cham, 2018; pp 177–196. https://doi.org/10.1007/978-3-319-58503-1_15.
- (19) Wenzel, W. W.; Unterbrunner, R.; Sommer, P.; Sacco, P. Chelate-Assisted Phytoextraction Using Canola (*Brassica Napus* L.) in Outdoors Pot and Lysimeter Experiments. *Plant Soil* **2003**, *249* (1), 83–96. <https://doi.org/10.1023/A:1022516929239>.
- (20) Xiao, L.; Cheng, X.; Zhang, T.; Guo, M.; Zhang, M. Efficient Inorganic/Organic Acid Leaching for the Remediation of Protogenetic Lead-Contaminated Soil. *Appl. Sci.* **2022**, *12* (8), 3995. <https://doi.org/10.3390/app12083995>.
- (21) Xie, N.; Chen, Z.; Wang, H.; You, C. Activated Carbon Coupled with Citric Acid in Enhancing the Remediation of Pb-Contaminated Soil by Electrokinetic Method. *J. Clean. Prod.* **2021**, *308*, 127433. <https://doi.org/10.1016/j.jclepro.2021.127433>.
- (22) Wang, L.; Zhang, H.; Cao, G.; Zhang, W.; Zhao, H.; Yang, Y. Effect of Activated Carbon Surface Functional Groups on Nano-Lead Electrodeposition and Hydrogen Evolution and Its Applications in Lead-Carbon Batteries. *Electrochimica Acta* **2015**, *186*, 654–663. <https://doi.org/10.1016/j.electacta.2015.11.007>.
- (23) Klunder, K. J.; Nilsson, Z.; Sambur, J. B.; Henry, C. S. Patternable Solvent-Processed Thermoplastic Graphite Electrodes. *J. Am. Chem. Soc.* **2017**, *139* (36), 12623–12631. <https://doi.org/10.1021/jacs.7b06173>.
- (24) McCord, C. P.; Summers, B.; Henry, C. S. Redox Behavior and Surface Morphology of Polystyrene Thermoplastic Electrodes. *Electrochimica Acta* **2021**, *393*, 139069. <https://doi.org/10.1016/j.electacta.2021.139069>.

- (25) Togonon, J. J. H.; Chiang, P.-C.; Lin, H.-J.; Tsai, W.-C.; Yen, H.-J. Pure Carbon-Based Electrodes for Metal-Ion Batteries. *Carbon Trends* **2021**, *3*, 100035. <https://doi.org/10.1016/j.cartre.2021.100035>.
- (26) Long, J. W.; Dunn, B.; Rolison, D. R.; White, H. S. 3D Architectures for Batteries and Electrodes. *Adv. Energy Mater.* **2020**, *10* (46), 2002457. <https://doi.org/10.1002/aenm.202002457>.
- (27) Teixidor, G. T.; Zaouk, R. B.; Park, B. Y.; Madou, M. J. Fabrication and Characterization of Three-Dimensional Carbon Electrodes for Lithium-Ion Batteries. *J. Power Sources* **2008**, *183* (2), 730–740. <https://doi.org/10.1016/j.jpowsour.2008.05.065>.
- (28) Mallakpour, S.; Azadi, E.; Mustansar Hussain, C. Fight against COVID-19 Pandemic with the Help of Carbon-Based Nanomaterials. *New J. Chem.* **2021**, *45* (20), 8832–8846. <https://doi.org/10.1039/D1NJ01333E>.
- (29) Antiochia, R. Electrochemical Biosensors for SARS-CoV-2 Detection: Voltametric or Impedimetric Transduction? *Bioelectrochemistry Amst. Neth.* **2022**, *147*, 108190. <https://doi.org/10.1016/j.bioelechem.2022.108190>.
- (30) Sin, M. L.; Mach, K. E.; Wong, P. K.; Liao, J. C. Advances and Challenges in Biosensor-Based Diagnosis of Infectious Diseases. *Expert Rev. Mol. Diagn.* **2014**, *14* (2), 225–244. <https://doi.org/10.1586/14737159.2014.888313>.
- (31) Sykes, J. E.; Rankin, S. C. Chapter 2 - Immunoassays. In *Canine and Feline Infectious Diseases*; Sykes, J. E., Ed.; W.B. Saunders: Saint Louis, 2014; pp 10–16. <https://doi.org/10.1016/B978-1-4377-0795-3.00002-8>.
- (32) Lakhin, A. V.; Tarantul, V. Z.; Gening, L. V. Aptamers: Problems, Solutions and Prospects. *Acta Naturae* **2013**, *5* (4), 34–43.
- (33) Kumar Kulabhusan, P.; Hussain, B.; Yüce, M. Current Perspectives on Aptamers as Diagnostic Tools and Therapeutic Agents. *Pharmaceutics* **2020**, *12* (7), 646. <https://doi.org/10.3390/pharmaceutics12070646>.
- (34) Kholafazad-Kordasht, H.; Hasanzadeh, M.; Seidi, F. Smartphone Based Immunosensors as next Generation of Healthcare Tools: Technical and Analytical Overview towards Improvement of Personalized Medicine. *TrAC Trends Anal. Chem.* **2021**, *145*, 116455. <https://doi.org/10.1016/j.trac.2021.116455>.
- (35) Olenik, S.; Lee, H. S.; Güder, F. The Future of Near-Field Communication-Based Wireless Sensing. *Nat. Rev. Mater.* **2021**, *6* (4), 286–288. <https://doi.org/10.1038/s41578-021-00299-8>.

APPENDIX 1: SUPPLEMENTAL FOR CHAPTER 2

Anodic stripping voltammograms for the real samples were collected. The peak heights from the voltammograms were used to construct the standard addition calibration curves in

Figure 2.6. Electrochemical and deposition parameters are described in Experimental.

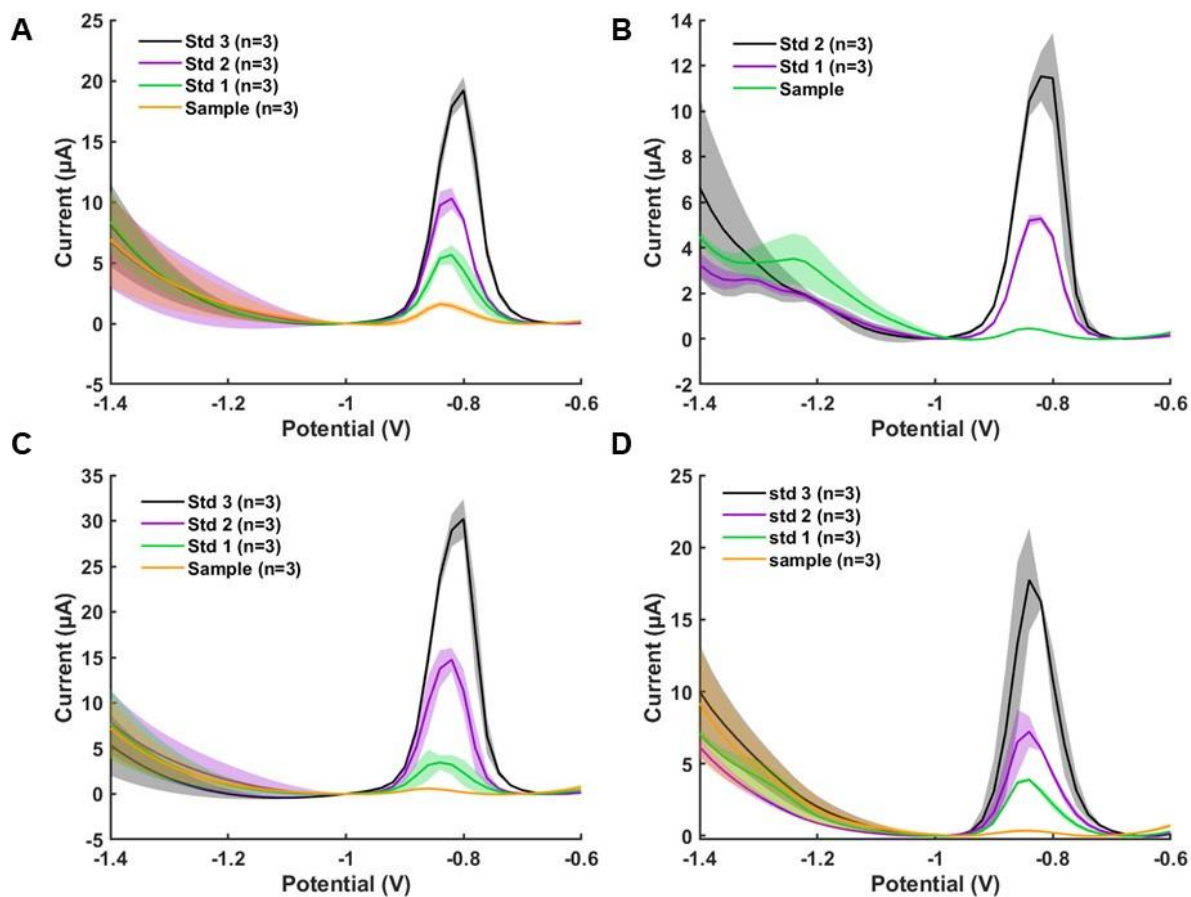


Figure S2.1: Voltammograms of Pb^{2+} deposition of the lead standards and sample with 2 ppm of Bi^{3+} for A) Sample 1, B) Sample 2, C) Sample 3, D) Sample 4. Analysis was performed in 0.1 M acetate buffer pH 4, 360 s deposition time, -1.4 V deposition potential. Shaded area represents the standard deviation for the voltammograms for $n=3$.

For accurate quantification using the inductively coupled plasma optical emission spectroscopy (ICP-OES) instrument, calibration curves were generated using five standards of Pb^{2+} , prepared in 5% nitric acid solution. Calibration curves were generated for both the filtride and filtrate analysis, as the sample solution differed for each sample type. The filtrides were composed of 5% nitric acid, whereas the filtrates were composed of a solution containing 0.5M citric acid and 0.1M acetate buffer.

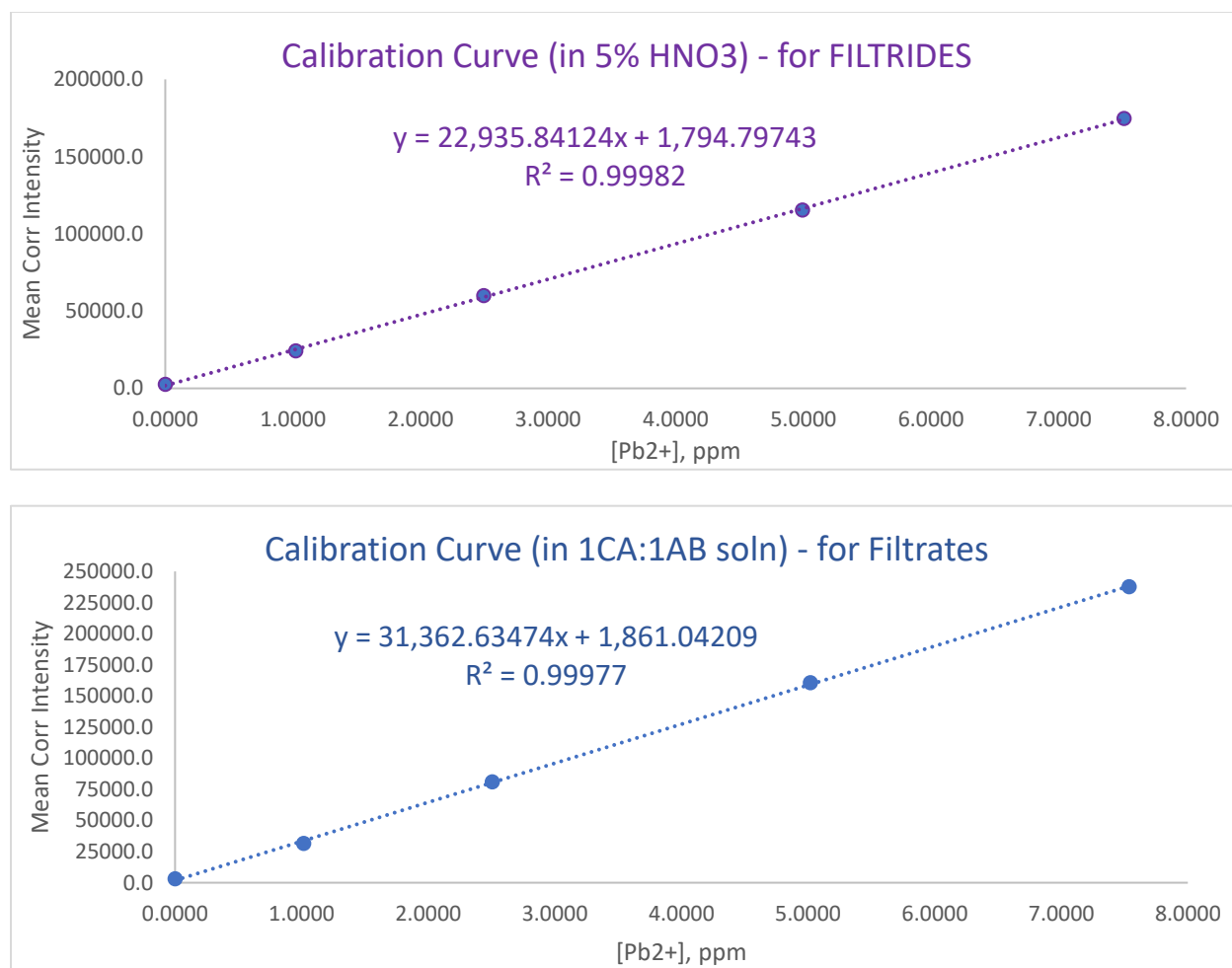


Figure S2.2. Representative calibration curves for the analysis of Pb^{2+} in the cosmetic samples filtrides (top) and filtrates (bottom). Pb^{2+} concentrations ranged from 0 – 7.5 ppm.

APPENDIX 2: SUPPLEMENTAL FOR CHAPTER 3

Lead standards, from 10-200 ppb were used to voltammograms on all six TPE formulations. The peak heights from the voltammograms were used to construct the calibration curves in **Figure 3.1**. Electrochemical and deposition parameters are described in Experimental.

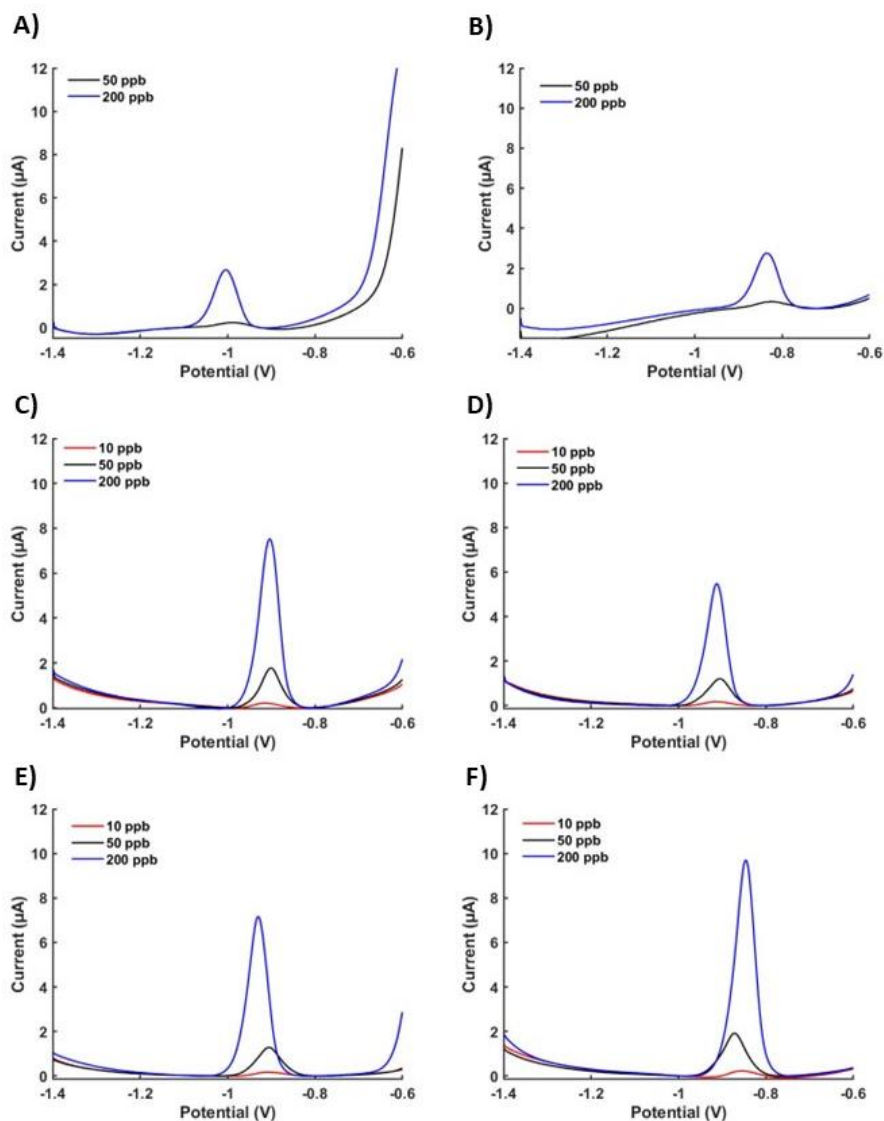


Figure S3.1: Representative voltammograms of Pb^{2+} deposition from 10 – 200 ppb with 2 ppm of Bi^{3+} for **A)** PCL-3569, **B)** PCL-TC303, **C)** PMMA-3569, **D)** PMMA-TC303, **E)** PS-3569, and **F)** PS-TC303. PCL-TPEs were unable to detect 10 ppb of Pb^{2+} . Analysis was performed in 0.1 M acetate buffer pH 4, 360 s deposition time, -1.4 V deposition potential.

X-ray photoelectron spectroscopy (XPS) was scanned across a wide energy range, to ensure no contamination was observed on the TPE surfaces. Only oxygen and carbon peaks were observed, indicating there was no contamination.

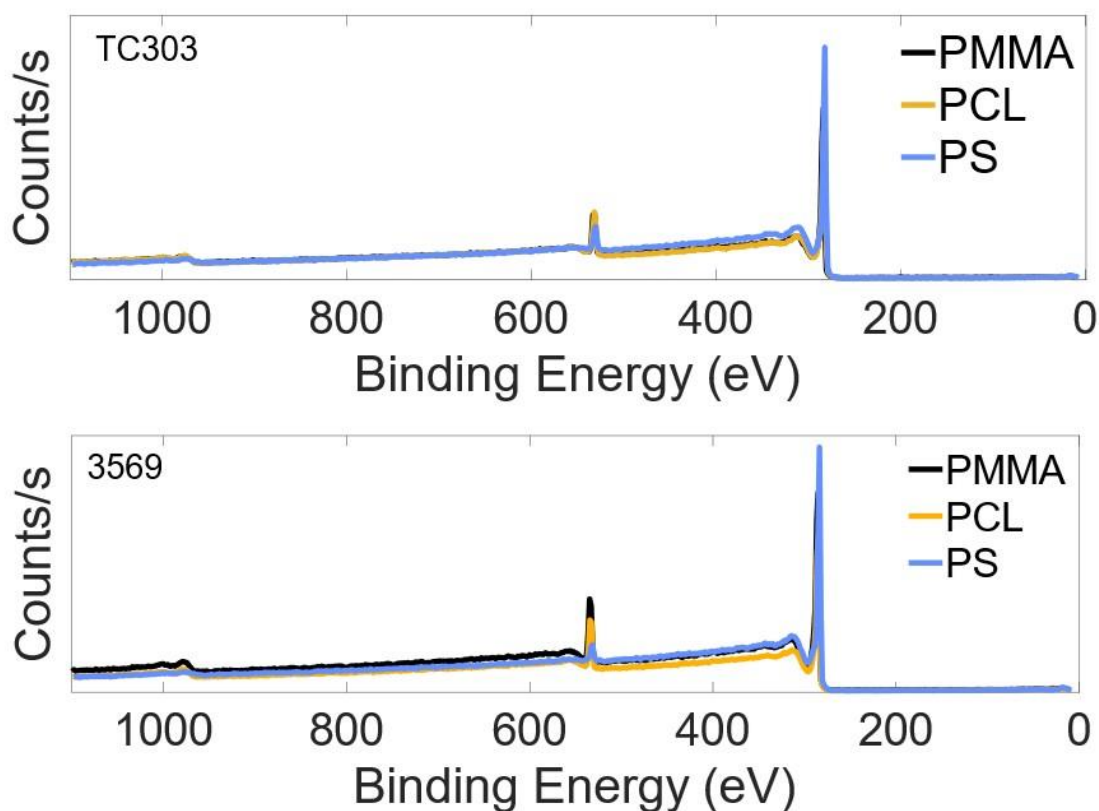


Figure S3.2. XPS survey spectra of the PCL-, PS-, and PMMA-TPEs made with TC303 graphite (top) and 3569 graphite (bottom). C1s is at 285 eV and O1s is at 531 eV.

Scanning electron microscopy (SEM) was performed at multiple magnifications at a single location on all six TPE formulations. $1 \times 10^4 \times$ magnification is reported in **Figure 3.5**. 100X, and $5 \times 10^3 \times$ give a broader view of the surface morphology, whereas $1 \times 10^4 \times$ illustrates the most detail.

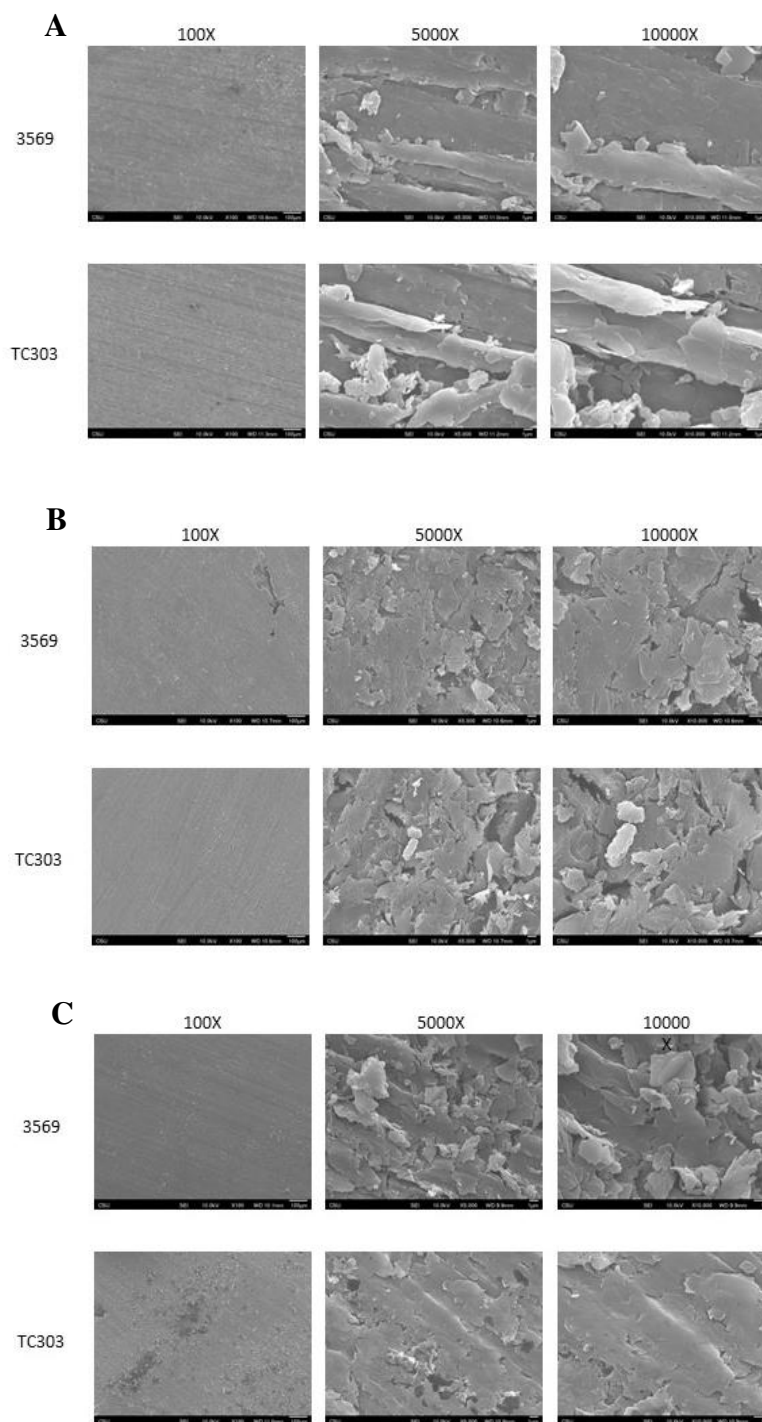


Figure S3.3: Scanning electron microscopy images for 100X, 5×10^3 X, and 1×10^4 X magnifications for **A)** PCL-TPEs, **B)** PMMA-TPEs, and **C)** PS-TPEs.

APPENDIX 3: SUPPLEMENTAL FOR CHAPTER 4

Overview of the electrode functionalization prior to the addition of the inactivated virus samples. All steps used 20 μL of solutions, except for the aged casein blocker step, which used 50 μL of solution.

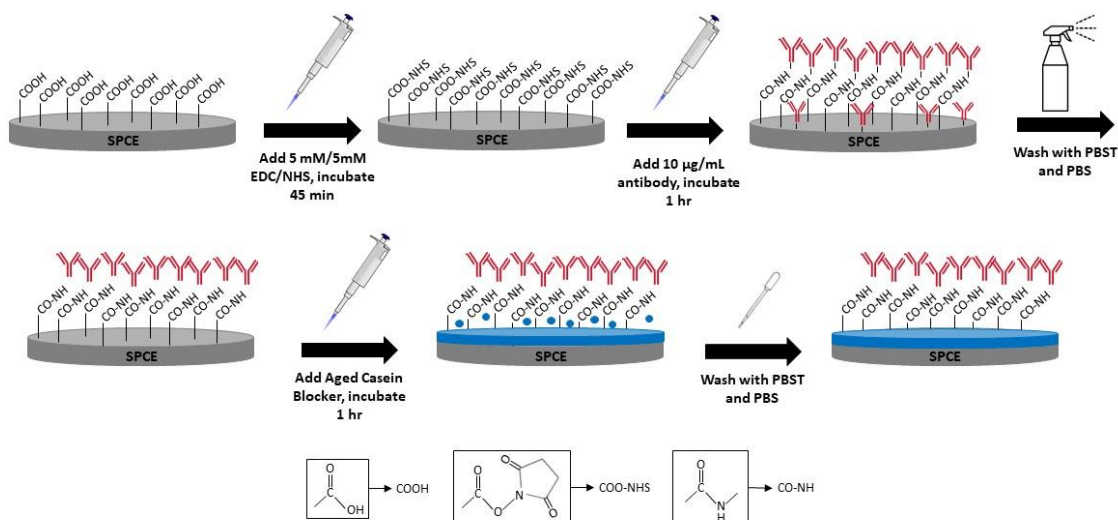


Figure S4.1. Schematic of the functionalization of the SPCE. SPCE are first modified with EDC/NHS, which covalently binds the antibody to the surface. The electrode surface is then blocked with Aged Casein solution. Briefly, the EDC reacts with the carboxylic groups on the electrode surface. This forms an intermediate, which can react with the NHS, forming an amine-reactive compound, which binds the NH_2 group on the antibody.

An Enzyme-linked immunosorbent assay (ELISA) was used to validate the concentrations of antigen samples used on the electrochemical system. Validation was performed on both recombinant N-protein and inactivated SARS-CoV-2 virus.

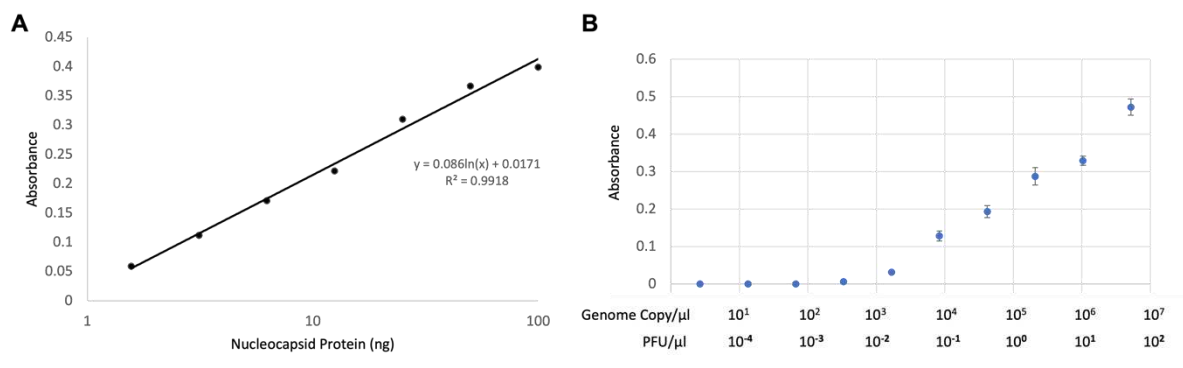


Figure S4.2. ELISA validation of recombinant N-protein and inactivated SARS-CoV-2 samples. Antigen capture ELISA protocol adapted from Terry JS et al., Virology 2021 Jun, 558:28-37. (A) Standard curve using recombinant N-protein to determine detectable quantity of antigen by standard antigen capture ELISA. Limit of detection of 1.64 ng. (B) Detectable quantity of SARS-CoV-2 genome copies and plaque forming units (PFU) by standard antigen capture ELISA. Calculations utilized genome copies obtained by ddPCR and PFU obtained by plaque assay. Limit of detection determined to be 7 PFU/mL.

Clinical samples were attained and ran on electrochemical assay as described in the main text. Information of the clinical samples is listed in **Supplemental Table 4.1** for positive samples and **Supplemental Table 4.2** for the negative samples.

Table S4.1 Clinical study results for positive samples. NA indicates that the assay was not performed. * For the electrochemical assay, a value of 0 indicates that the test result was below the LOD, defined as the viral concentration corresponding to 3 times the standard deviation of the signal recorded in the absence of virus

Sample name	Sample ID	Collection date	N1 CT	N2 CT	E CT	PFU/ml plaque assay	Equivalent PFU/ml electrochemical assay*	Equivalent copies/mL electrochemical assay*
P1	AV020A	06/05/2020	28.967	23.778	25.943	0	20.1	9.50E+05
P2	AV020B	13/05/2020	33.663	33.529	33.783	NA	0	0
P3	AV028	13/05/2020	30.097	29.849	30.598	NA	0	0
P4	CH010	08/04/2020	28.559	27.409	28.490	0	0	0
P5	CH040	08/04/2020	26.611	25.261	26.584	0	0	0
P6	S003	08/04/2020	29.745	29.140	30.841	0	0	0
P7	S014	08/04/2020	26.202	24.833	25.710	0	25.9	1.22E+06
P8	S065A	08/04/2020	30.622	29.902	31.895	0	0	0
P9	AV028B	06/05/2020	19.15	14.225	16.780	6600	12070.7	5.71E+08
P10	S022	08/04/2020	17.98	17.330	18.634	1220	1982.1	9.37E+07
P11	S094A	08/04/2020	17.96	16.216	17.777	31600	584.5	2.76E+07
P12	S094B	15/04/2020	22.22	22.788	25.188	484	978	4.62E+07
P13	S094C	22/04/2020	22.86	23.586	24.787	40	130.4	6.16E+06

Table S4.2 Clinical study results for negative samples. Undetermined indicates a Ct value > 38. NA indicates that the assay was not performed. * For the electrochemical assay, a value of 0 indicates that the test result was below the LOD, defined as the viral concentration corresponding to 3 times the standard deviation of the signal recorded in the absence of virus.

Sample name	Sample ID	Collection date	N1 CT	N2 CT	E CT	PFU/ml plaque assay	Equivalent PFU/ml electrochemical assay*	Equivalent copies/mL electrochemical assay*
N1	RI005	08/05/2020	Undetermined	NA	NA	NA	0	0
N2	RI100	08/05/2020	Undetermined	NA	NA	NA	0	0
N3	RI008	08/05/2020	Undetermined	NA	NA	NA	0	0
N4	RI026	08/05/2020	Undetermined	NA	NA	NA	0	0
N5	RI058	08/05/2020	Undetermined	NA	NA	NA	0	0
N6	RI021	08/05/2020	Undetermined	NA	NA	NA	0	0
N7	RI064	08/05/2020	Undetermined	NA	NA	NA	0	0
N8	RI071	08/05/2020	Undetermined	NA	NA	NA	0	0
N9	RI057	08/05/2020	Undetermined	NA	NA	NA	0	0

All materials used and assembled for the electrochemical assay were collected and a cost analysis was performed (**Table S4.3**) to better understand how much the assay would cost for a single sample.

Table S4.3 Estimated electrode cost. Estimated cost breakdown of reagents and materials for each electrode. *An alternative commercial synthetic carbon was selected for this calculation, from Asbury Carbons (NANO307-5LBPAIL).

	Materials	Estimated cost/sample(\$)
<i>Sensor Framework</i>	Polyester film	0.0003
	Double-side adhesive	0.003
	Subtotal	0.004
<i>Electrode</i>	Graphite powder	0.005
	Carbon ink	0.024
	Ag AgCl ink	0.009
	Subtotal	0.038
<i>Reagents</i>	Anti-N-antibody	0.800
	HRP-antibody	0.051
	TMB	0.023
	Subtotal	0.87
<i>Total cost</i>		0.918